FILTERING OF SINGLE PHOTON LIDAR DATA

A Dissertation

Presented to

the Faculty of the Department of Civil and Environmental Engineering

University of Houston

In Partial Fulfillment

of the Requirements for the Degree

Doctor of Philosophy

in Geosensing Systems Engineering and Sciences

by

Xiao Wang

December, 2017

FILTERING OF SINGLE PHOTON LIDAR DATA

Xiao Wang

Approved:

Chair of the Committee
Craig L. Glennie, Associate Professor
Department of Civil & Environmental Engineering, University of Houston

Committee Members:

Ramesh L. Shrestha, Professor
Department of Civil & Environmental Engineering, University of Houston

Michael Starek, Assistant Professor
Director of the Measurement Analytics Lab
School of Engineering and Computing Sciences, Texas A&M University-Corpus Christi

Hyongki Lee, Associate Professor
Department of Civil & Environmental Engineering, University of Houston

Preston Hartzell, Research Assistant Professor
Department of Civil & Environmental Engineering, University of Houston

Suresh K. Khator, Associate Dean
Cullen College of Engineering

Craig L. Glennie, Program Director
Geosensing Systems Engineering & Sciences

Acknowledgements

I would like to express my deepest gratitude to my advisor, Dr. Craig Glennie, for his excellent guidance, caring and continuous support throughout my Ph.D. study and dissertation research. I am thankful to him for holding me to a high research standard and inspiring me to be a better researcher. I would like to thank Dr. Ramesh Shrestha, Dr. Hyongki Lee, Dr. Michael Starek, and Dr. Preston Hartzell for carefully reading and revising my manuscripts. I also want to thank Dr. Zhigang Pan for discussing problems with me and revising article manuscripts for me. Without his valuable advice and suggestions, I would not have gotten any of my work published. I am grateful to Dr. Ning Cao and Dolu Okeowo who lend me a lot of technical support. Many thanks to my colleagues at NCALM for their various forms of support.

I want to thank Dr. Xiao Zhang, Dr. Hongzhou Wang, and Dr. Yuhang Zhang who lent me much help when I arrived at the U.S. Without you, I could have never get used to the new life here so fast and easily. I also want to thank JB, AK, Kirstie and all other members at Badminton Club of UH. I spent a great time with all of you playing badminton.

Finally, I would also like to thank my family for their love and support to me. I am grateful to my parents who raise me up with all their hearts. I want to thank my beloved girlfriend Dr. Siya Huang who encouraged me when I was depressed, helped me, and made me a better man. I appreciate her help and support in both life and research.

FILTERING OF SINGLE PHOTON LIDAR DATA

An Abstract

Of a

Dissertation

Presented to

The Faculty of the Department of Civil and Environmental Engineering

University of Houston

In Partial Fulfillment

Of the Requirements for the Degree of

Doctor of Philosophy

in Geosensing Systems Engineering and Sciences

by

Xiao Wang

December 2017

Abstract

Light detection and ranging (LiDAR) is a powerful technique that provides accurate three-dimensional measurement of targets. New generation single photon LiDAR (SPL) systems are able to collect data at faster rates than conventional linear-mode LiDAR and at a lower cost. However, the new SPL systems are also very sensitive to false returns, which cause a high noise rate in the collected data. As a result, SPL systems present new data processing challenges.

The filtering of SPL data has different requirements than imaging or conventional linear-mode LiDAR data. There is no intensity information for each return, and the data structure of the 3-D point cloud is irregularly spaced and different than 2-D images, therefore most imaging processing methods cannot be applied directly to SPL data. It also has a much higher noise rate than conventional LiDAR data, which makes conventional LiDAR filtering methods inapplicable. There has been some initial research on techniques for filtering SPL data; however, the problem has not been fully studied. In this dissertation, new SPL filtering algorithms which accommodate the higher noise and false return rates, along with afterpulsing will be developed and analyzed.

First, two novel filtering methods are proposed to remove solar/dark noise for 2-D and 3-D SPL data respectively. The 2-D method considers inhomogeneous noise distribution and local point distribution to provide a more reliable filtering result. The 3-D method utilizes principle component analysis to remove near-signal noise more effectively. Results from these two methods were compared with current methods on different types of terrain. The proposed methods removed more noise points and had lower RMSE compared to the reference data. An improved version of the proposed 3-D

filter that better retains linear features such as powerlines is then proposed and validated. Finally, a method based on robust regression is proposed to remove afterpulses. We found that on average, 90% of the afterpulse points were removed over rooftop areas and the mean elevation difference with respect to a reference surface was reduced from 1.95 m to 0.23 m.

Table of Contents

List of Figures

List of Tables

Chapter 1

Introduction

Remote sensing helps provide a better understanding of the world. Scientists can observe large scale vegetation distribution with modern satellite optical imaging [1], visualize urban heat island effects using advanced infra-red sensors [2] and detect targets hundreds of miles away with the help of radar [3]. Among the many remote sensing techniques, light detection and ranging (LiDAR) can directly provide accurate 3-D information of imaged targets. Since its first use as a part of the Apollo Command and Service Module project in the 1970s [4], LiDAR has shown its ability to accurately map in a variety of applications: Earth topography, forest biomass, shallow water bathymetry and ice sheet elevation changes [5]–[8] to name just a few.

Currently, most operational LiDAR systems work in a modality usually termed linear-mode: here the amplitude of the output laser signal is linearly proportional to that of the received/reflected energy. However, a new generation of remote sensing LiDAR is currently being developed in which the detector is sensitive to even one received photon, and appropriately termed a single photon LiDAR (SPL) system. These SPL systems have a variety of benefits, but also require new data processing approaches. This dissertation aims to address one of the outstanding challenges with SPL point clouds: data filtering.

1.1 Fundamental concept of airborne LiDAR

LiDAR can be classified as terrestrial, mobile, airborne, spaceborne and marine based upon the platform on which it is deployed [9]. For example, an airborne laser scanning system (ALS) is an active acquisition system mounted on an aircraft. A typical

ALS system usually has the following main components: 1) a laser ranging unit and scanning assembly; 2) a combined GNSS (Global Navigation Satellite System)/IMU (Inertial Measurement Unit) position and orientation system; and 3) computer subsystem for data logging and control.

The laser ranging unit transmits laser pulses and records backscattered laser radiation at a pulse repetition rate of tens or even hundreds of kilo hertz. The receiver records information on the time of flight (TOF) and the relative strength of the return echo. With accurate timing of the TOF at the picosecond level, the system can obtain centimeter level ranging by multiplying the TOF with the known speed of light. The GNSS and INS provide position and altitude information which can transform the local coordinate system of the laser measurements into a global reference frame. Data from the three components results in a globally geo-referenced 3-D point cloud. The users can therefore obtain accurate 3-D information of the targeted area from the resultant point cloud.

Airborne LiDAR systems can provide versatile, accurate 3-D measurement of target areas with fast collection speed. They have been used as a complement or even as a replacement for other existing geo-data collection methods. Airborne LiDAR data has been employed for a variety of tasks including DEM (digital elevation model) generation [10], [11], agriculture monitoring [12], archeology discovery [13]–[15], ecosystem health monitoring [16]–[18] and geomorphology [9], [19], [20]. As the number of new LiDAR acquisitions increases, ALS data will continue to show its advantages and versatility for more and more fields of study.

1.2 Motivation for single photon LiDAR (SPL)

Traditional linear-mode LiDAR uses either photodiodes or photomultipliers as the detector to convert incoming photons to electrical current. The output current is proportional to the number of incident photons, so these are normally referred to as linear mode sensors [21]. Because of residual systematic and stochastic noise sources in these detectors, such as electrical noise or solar background noise, a high electrical current magnitude is preferred to decrease the probability of recording false positive returns. Usually several hundreds of photons are needed for the system to record an event [21]. In this case, a high energy laser pulse is also needed; pulse energy for ALS is typically on the order of hundreds of micro Joules [22].

The basic design of a conventional ALS utilizes a simplified detection scheme that only works when high energy pulses are used so that the noise level doesn't exceed the detection threshold. However, high energy systems are not always desirable because of the size and cost of the system hardware. In some projects with a fixed power budget, for example, unmanned aerial vehicle (UAV) missions, the heavier system and battery will be a significant limitation. The complex electronics required also increases overall system cost. These high energy pulse systems do not make the most efficient use of transmitted laser photons [23]. It has been shown that for a given laser power-receiver aperture product, the maximum surface return rate is obtained by adopting a single photon detection threshold and a low mean signal strength [23]. Physically this implies using a high repetition rate, but low energy, laser transmitter.

These problems have motivated an alternate way to detect low energy light, made possible by developments in semi-conductor detection techniques. Newer generation

detectors using Geiger-mode avalanche photodiodes (GmAPD) or microchannel plate photomultiplier tubes (MCP-PMT) are sensitive at the single incoming photon level. MIT Lincoln Laboratory (MITLL) has pioneered the development of single photon LiDAR using GmAPD [24]. MITLL developed their Gen-I 3-D LiDAR using a 4×4 Geiger-mode APD array [25]. This brass board LiDAR system was used to test the concept of using an array of GmAPD to capture high-resolution 3-D data. After the success of the Gen-I system, a larger 32×32 GmAPD array was tested in the Gen-III system [26]. Recently, a new model of the LL 3-D imaging LiDAR has been developed with a 32×128 detector array [27].

New generation LiDAR using single photon detectors have many operational advantages over conventional linear-mode LiDAR. One of the benefits is fast data acquisition speed. Three factors contribute to the improvement in data collection speed. The first factor is the novel design of the detector; SPL can image terrain within the receiver FOV (field of view) for tens or hundreds of pixels of a photon detector array simultaneously and each of the pixels is fed into a separate timing channel [28], [29]. Therefore, SPL can collect data much faster than most conventional ALS that typically only record several returns for each fired laser pulse. Second, a higher acquisition altitude helps accelerate the collection. ALS data is collected by scanning the target area with a specific pattern. With a fixed maximum scan angle, the higher the aircraft flies, the wider the swath will be (for saw tooth and parallel line scan patterns) or the larger the radius of a circular scan pattern will be. Therefore with the same flight velocity the system can scan larger areas from a higher altitude. Of course, higher altitudes can also cause lower point density because the size of the imaged footprint is proportional to flight altitude.

For conventional ALS, the aircraft usually flies at lower altitudes to insure high point density. However, for SPL systems, this is compensated for because an array of detectors is employed. Finally, the faster speed of the aircraft enabled by the array of detectors is also an important factor. Again, considering the scanning mechanism of an ALS system, for a fixed swath, the faster the aircraft flies, the larger the area that is scanned in a unit time. These three factors enable SPL to collect data much faster than the conventional linear-mode ALS, without sacrificing point density.

Additional benefits for SPL systems are their fast response to incident photons and their compact size. For GmAPD, when a small number of photons hit the detector, an avalanche current will be generated to stop the CMOS (complementary metal-oxide-semiconductor) timer after ~100 picoseconds [30]. For a MCP PMT the rise time ranges from ~100 picoseconds to several hundred picoseconds [31]. The FWHM (full width at half maximum) of the emitted pulse width is usually on the order of hundreds of picoseconds whereas linear-mode LiDAR usually employs few nanosecond pulse width [32]. This fast response and narrow pulse width together enable a high range precision for SPL systems. However, the systems saturate with incident photons and therefore need time to recover after recording a return. The detectors record no intensity information due to the saturation and thus require no analogue gain circuits, which enables production of compact detector arrays.

Finally, the new single photon detectors make long range light detection easier. For spaceborne laser altimetry, the pulse energy will severely attenuate because of atmospheric scattering and absorption during the long travel path. With the single photon technique, satellites can detect even a single return photon, which can provide ranges on

orbit. In 2018, NASA (National Aeronautics and Space Administration) will launch the ICESat-2 satellite to observe ice sheet elevation change and sea ice thickness, while also generating an estimate of global vegetation biomass. The sole instrument on ICESat-2 will be the Advanced Topographic Laser Altimeter System (ATLAS). ATLAS utilizes single photon LiDAR to obtain a denser data profile of the ice sheet than its predecessor ICESat. The pulse energy of ICESat-2 will only be 25–100 μJ compared to pulse energy of ~100 mJ for its predecessor ICESat [23].

1.3 Limitation of single photon LiDAR

These new single photon LiDAR systems can collect data at very fast speeds, and provide dense point clouds with decreased collection costs. All these benefits seem to suggest that this technology will have a promising future. However, one severe limitation of SPL hinders the wide scale adoption of the technology until it is solved; the very high noise level and false detection rate in SPL point clouds. The high sensitivity of the detectors that enables SPL to detect single photon events can also cause the system to record false returns from sources such as solar energy and system dark count. Because of the detection mechanism employed in SPL, the number of incoming photons is irrelevant, which leads to the absence of estimates of return intensity, which in turn means there is no differentiator between signal and noise detections. The system is sensitive to photon events in a large range gate, usually several hundred meters, to ensure that all the signal points are recorded. Unlike conventional linear-mode LiDAR, which has few noise points in the data because of the high detection threshold, there are a large number of noise points in a SPL data set (as shown in Figure 1-1) and the data cannot be used until a filter

that effectively separates signal and noise returns is applied. For linear-mode LiDAR data processing, which is a much more mature field of research, there are a number of filtering methods that have been developed and applied. Typically, filtering of linear-mode data means removing non-ground points and obtaining an estimate of the ground DTM (Digital Terrain Model). The method works by considering one or several of the following ground surface characteristics [33]: lowest elevation [34], ground surface steepness [35]–[37], ground surface elevation difference [36], [38], [39] and ground surface homogeneity [36], [40]. The first characteristic, lowest elevation should always be considered when using other characteristics. For example, using elevation alone will wrongly label house roofs, which are usually very flat and smooth, as ground. In SPL data processing, estimation of ground is also an important task. However, all the developed methods for linear-mode LiDAR mentioned above cannot be used. The signal points for either ground points or non-ground points are typically distributed in the middle of the range gate and there are therefore noise points both above and under ground (again see Figure 1-1). In this case, starting from an assumption of lowest elevation cannot be used as the primary criteria to filter ground.

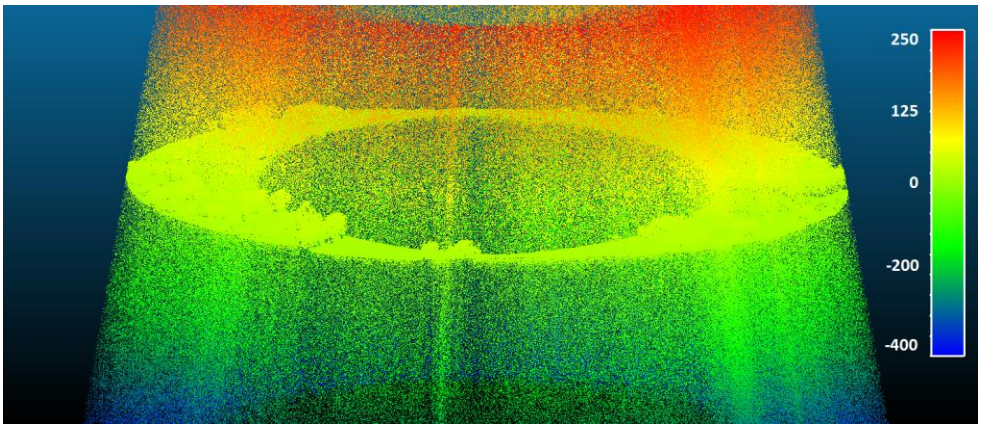

Figure 1-1 Two-second data sample of High Resolution Quantum LiDAR System (HRQLS) system raw point cloud (detail of this system are given in Chapter 2). The points are colored by elevation. Noise points can be seen both above and under the ground.

The characteristics of SPL noise makes SPL filtering a unique issue to be addressed, especially since current image processing or conventional LiDAR filtering algorithms do not work for SPL data. The study of SPL filtering algorithms is still in its infancy and only a few methods have been published to date [8], [41]–[46]. All of the algorithms take advantage of the fact that signal points cluster together while noise points are distributed sparsely in the space. From this point of view, the methods can be basically divided into two categories, image-based and density-based. The basic idea behind image-based methods is to rasterize the data into a 2-D image and use established image processing techniques to filter the noise. The density-based methods try to define a specific region around an investigated point and count the number of points within the arbitrarily defined region. The point will be considered as noise if the number of neighboring points is smaller than a threshold. These methods will be fully reviewed in Chapter 3. While they address the filtering problem to some degree, they also suffer from significant deficiencies, for example based on some assumptions that are not universally applicable or relying on arbitrary thresholds. A better and adaptable filtering algorithm is still needed.

1.4 Contributions

Single photon technology provides many advantages over conventional linear-mode LiDAR systems but also introduces new challenges for discriminating true returns within the point cloud. We are aiming to develop an effective filtering algorithm for SPL data. To achieve this goal, the following contributions are made in this dissertation:

1). A novel solar/dark noise filtering method for single photon laser altimetry data based on Bayesian decision theory is proposed and implemented.

2). A novel solar/dark noise filtering method for 3-D imaging single photon LiDAR data is proposed and implemented to remove near-signal noise more effectively.

3). An improved solar/dark noise filtering method is proposed and implemented to retain linear features during filtering process.

4). A novel method to remove afterpulses based on robust regression is proposed and implemented.

These filtering methodologies significantly improve the quality of the filtered point clouds by considering inhomogeneous noise distribution and local signal geometry which are not discussed by the current published methods. The afterpulse filtering method also demonstrates its efficiency in afterpulse removal which is rarely studied in current filtering research.

1.5 Organization of dissertation

Chapter 2 introduces the theory of single photon LiDAR and provides an overview of current SPL systems.

Chapter 3 reviews state-of-art filtering algorithms for both laser altimeter and 3-D imaging LiDAR.

Chapter 4 describes a novel algorithm for single photon laser altimetry data.

Chapter 5 describes a novel algorithm for 3-D imaging single photon LiDAR data.

Chapter 6 describes an improved filtering algorithm for 3-D imaging single photon LiDAR data.

Chapter 7 describes a method to remove afterpulses in single photon LiDAR data.

Chapter 8 summarizes the conclusions of the work and outlines possible future research directions.

Chapter 2

SPL Theory and SPL Systems

2.1 Single photon LiDAR

The equation describing the backscattered signal for SPL is similar to that for traditional linear-mode LiDAR. Assuming a collimated beam, the expression for the expected number of photon electrons n_s generated at the LiDAR detector is [47]

$$n_s = \eta_h \eta_q \eta_r \cdot \frac{E_t}{h\nu} \cdot \rho_\lambda \cos(\alpha) \cdot \frac{A_r}{\pi R^2} \cdot \left[\exp\left(-\beta_{e,\lambda} R\right)\right]^2, \tag{2.1}$$

where η_h is the hologram efficiency (in the case of an altered beam), η_q is the detector quantum efficiency, η_r is the receiver optical efficiency, E_t is the transmitted energy with units of joules, h is Planck's constant, ν is the photon frequency in hertz, ρ_λ is the wavelength-dependent surface reflectance coefficient, α is the local incidence angle on the surface, A_r is the collecting area of the receiver aperture, $\beta_{e,\lambda}$ is the atmospheric extinction coefficient in per meter, and R is the range [23]. A narrow-band spectral filter is employed to reject incoming light outside a spectral band centered at the laser's wavelength.

One of the significant characteristics of SPL data is the high noise rate that is mainly a result of background solar noise and system dark current. The expected rate of noise photon electrons $n_{b,atm}$ due to solar background illumination can be modeled as [47]

$$n_{b,atm} = \frac{\eta_q \eta_r}{h\nu} \cdot \frac{N_\lambda B_\lambda \Omega_\lambda A_r T_0^{\sec(\theta_s)\cdot\exp\left(\frac{-h_a}{h_{sc}}\right)}}{4\pi\left(\sec(\alpha)+\sec(\theta_s)\right)} \times \left[1 - T_0^{\left(\sec(\alpha)+\sec(\theta_s)\right)\cdot\left(1-\exp\left(\frac{-h_a}{h_{sc}}\right)\right)}\right], \quad (2.2)$$

where N_λ is the input exoatmospheric solar irradiance at the laser wavelength λ, B_λ is the spectral filter bandwidth, Ω_r is the receiver field of view in steradians, θ_s is the solar zenith angle in radians relative to the local Earth surface, h_a is the LiDAR altitude, h_{sc} is the atmospheric vertical scale height (vertical distance at which the energy is expected to attenuate by a factor of e) and T_0 is the one-way atmospheric transmission defined as [23]

$$T_0 = T\left(h_a, \infty\right) = \exp\left[-\int_{h_a}^{\infty} dz' \mu\left(z'\right)\right], \quad (2.3)$$

where $\mu(z)$ is the atmospheric extinction coefficient that is assumed to be a function of the vertical height only.

Likewise, the expected rate of noise photon electrons due to Lambertian solar scattering at the surface can also be modeled by the following equation [47],

$$n_{b,surf} = \frac{\eta_q \eta_r}{h\nu} \cdot \frac{N_\lambda B_\lambda \Omega_\lambda A_r \rho_\lambda T_0^{\left(\sec(\alpha)+\sec(\theta_s)\right)\cdot\left(1-\exp\left(\frac{-h_a}{h_{sc}}\right)\right)}}{\pi}. \quad (2.4)$$

An SPL system exhibits dark current events in the detector due to things such as photocathode thermoemission, cosmic rays, and spontaneous emission under transient electric potentials in the LiDAR sensor head [47]. Dark rates are typically reported by the manufacture. The total mean number of noise photon electron per range bin is given as [47]

$$n_b = \left(n_{b,atm} + n_{b,surf} + n_{b,dark}\right) \cdot \tau_b, \quad (2.5)$$

where $n_{b,dark}$ is the dark noise rate in counts per second and τ_b is the length of a range bin in seconds.

Poisson random processes are used to model signal and noise returns as [48], [49]. The probability that there are n_t detected photon electrons is therefore given by [47]

$$P(n_t, n) = \frac{n^{n_t} \cdot e^{-n}}{n_t!}, \tag{2.6}$$

where n is the expected number of generated photon electrons. The probability that at least one event occurs is an important metric since the system will record the event without considering the number of photons. The probability that there is an event occurring is simply the compliment of the probability that zero events occur. This probability is given by

$$P(n > 0) = 1 - e^{-n}. \tag{2.7}$$

So, for each range bin, the recording of a photon electron is a binary event. Then along the whole range, the distribution of noise returns follows a uniform distribution.

Using the derived ranges for both signal and noise returns, a point cloud can be generated for SPL in a similar manner to the geo-referencing process for a conventional ALS system. Airborne LiDAR systems output 3-D coordinates of target regions using the GNSS (Global Navigation Satellite System)/INS (Inertial Navigation System) trajectory, the mounting calibration parameters, rotational offset between the scanner and the GNSS/INS system and the range and angle measurements of the scanners. An ALS system integrates all these measurements through the ALS direct georeferencing equation [50],

$$\begin{bmatrix} X \\ Y \\ Z \end{bmatrix}_G^l = \begin{bmatrix} X_0 \\ Y_0 \\ Z_0 \end{bmatrix}_{GNSS}^l + R_b^l(\omega,\varphi,\kappa)\left(\left(R_s^b\right)(d\omega,d\varphi,d\kappa)\cdot\gamma^s(\alpha,R) - \begin{bmatrix} l_x \\ l_y \\ l_z \end{bmatrix} \right), \tag{2.8}$$

where, $X, Y \text{ and } Z$ of the output vector are the coordinates of the target in a global coordinate frame and $X_0, Y_0 \text{ and } Z_0$ are the coordinates of the center of GNSS. The angles $\omega, \varphi \text{ and } \kappa$ are the roll, pitch and yaw of the sensor from the body frame to the local level frame determined by the INS and the angles $d\omega, d\varphi \text{ and } d\kappa$ are the boresight angles which indicates the angular mounting differences between the INS and scanner coordinate frames. The scan angle α and range R are measurements from the scanner. Finally, $l_x, l_y \text{ and } l_z$ are the lever arm offsets, which are the physical offsets between the INS origin and the measurement origin of the laser scanner.

For a single photon altimeter which fires lasers using a fixed angle without a scanning mechanism, equation (2.8) can be used directly; the only difference is that the scan angle α is fixed. However, for a 3-D imaging SPL, equation (2.8) needs to be modified because an array of detectors is used in the system with potentially different angles for each detector in the array. Figure 2-1 demonstrates a 10×10 2-D detector array as an example. For this configuration we have the following equation,

$$\begin{pmatrix} x_{pix} \\ y_{pix} \end{pmatrix} = \begin{pmatrix} -(i-5.5)\cdot\alpha_{pp} \\ (j-5.5)\cdot\alpha_{pp} \end{pmatrix}, \tag{2.9}$$

where, i and j are index of the pixel and α_{pp} is the pixel to pixel rotation angle. The array on the ground may be rotated with an angle α_R, and so equation (2.9) can be modified as

$$\begin{pmatrix} x'_{pix} \\ y'_{pix} \end{pmatrix} = \begin{pmatrix} \cos(\alpha_R) & -\sin(\alpha_R) \\ \sin(\alpha_R) & \cos(\alpha_R) \end{pmatrix} \begin{pmatrix} x_{pix} \\ y_{pix} \end{pmatrix}. \tag{2.10}$$

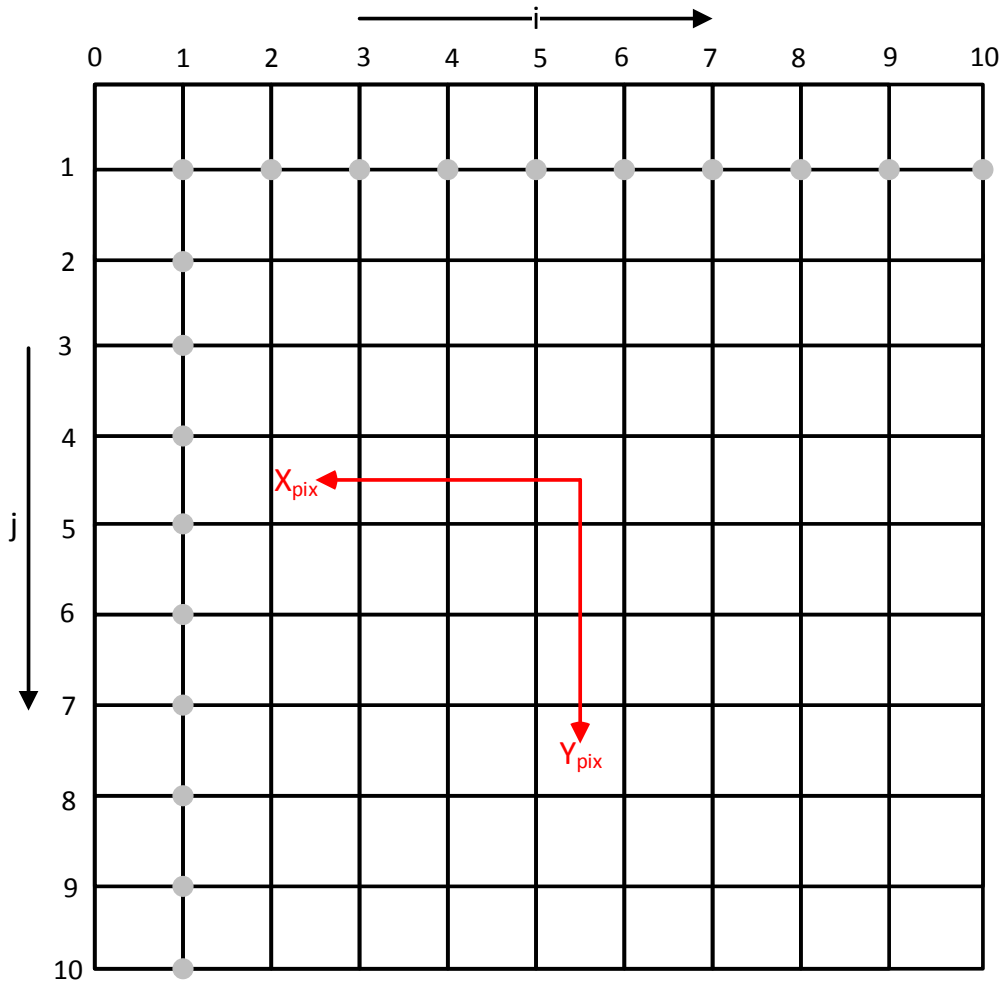

Figure 2-1 Example of a 10x10 2-D array. The laser shots at the intersection of lines are partially indicated by grey dots.

The scan pattern used in modern 3-D imaging SPL systems is primarily a circular scan as demonstrated in Figure 2-2. The laser is refracted by an optical wedge [51] and leaves the scanner with a fixed cone angle. The wedge is rotated and the horizontal mirror angle is recorded by the system. Considering the effect of a varying scan angle, we can modify equation (2.10) to the following form,

$$\begin{pmatrix} x_{pix_{rotated}} \\ y_{pix_{rotated}} \end{pmatrix} = \begin{pmatrix} \cos(\alpha) & -\sin(\alpha) \\ \sin(\alpha) & \cos(\alpha) \end{pmatrix} \begin{pmatrix} x'_{pix} \\ y'_{pix} \end{pmatrix}, \tag{2.11}$$

where, α is the scan angle. Equation (2.11) describes the vector in the array plane. We also require the central vector which is the vector from the sensor to the center of the array plane, and is calculated with the following equation,

$$\begin{pmatrix} x_{cv} \\ y_{cv} \\ z_{cv} \end{pmatrix} = \begin{pmatrix} \cos(-\alpha) & -\sin(-\alpha) & 0 \\ \sin(-\alpha) & \cos(-\alpha) & 0 \\ 0 & 0 & 1 \end{pmatrix} \begin{pmatrix} 1 & 0 & 0 \\ 0 & \cos(2\pi-\varphi) & -\sin(2\pi-\varphi) \\ 0 & \sin(2\pi-\varphi) & \cos(2\pi-\varphi) \end{pmatrix} \begin{pmatrix} 0 \\ 0 \\ -\rho \end{pmatrix}, \quad (2.12)$$

where, φ is the half cone angle and ρ is the range. When $\rho = 1$ and with some simplification, we have

$$\begin{pmatrix} x_U \\ y_U \\ z_U \end{pmatrix} = \begin{pmatrix} \sin(\varphi)\cdot\sin(\alpha) \\ \sin(\varphi)\cdot\cos(\alpha) \\ -\cos(\varphi) \end{pmatrix}. \quad (2.13)$$

The point vector from the sensor to the laser footprint on the ground will be the sum of the central vector and the pixel vector given as

$$\begin{pmatrix} x_{pv} \\ y_{pv} \\ z_{pv} \end{pmatrix} = \begin{pmatrix} x_U \\ y_U \\ z_U \end{pmatrix} + \begin{pmatrix} x_{pix_{rotated}} \\ y_{pix_{rotated}} \\ z_{pix_{rotated}} \end{pmatrix}. \quad (2.14)$$

We can then obtain the normalized pointing vector and range from the sensor to each laser footprint with the following equations:

$$\begin{pmatrix} x_{unitPV} \\ y_{unitPV} \\ z_{unitPV} \end{pmatrix} = \begin{pmatrix} x_{pv}/l \\ y_{pv}/l \\ z_{pv}/l \end{pmatrix} \textit{and}$$
$$r = \rho \begin{pmatrix} x_{unitPV} \\ y_{unitPV} \\ z_{unitPV} \end{pmatrix}, \quad (2.15)$$

where, l is the length of the pointing vector. With the range vector, the raw SPL data can be geo-referenced to form a point cloud using the same process as conventional airborne LiDAR data.

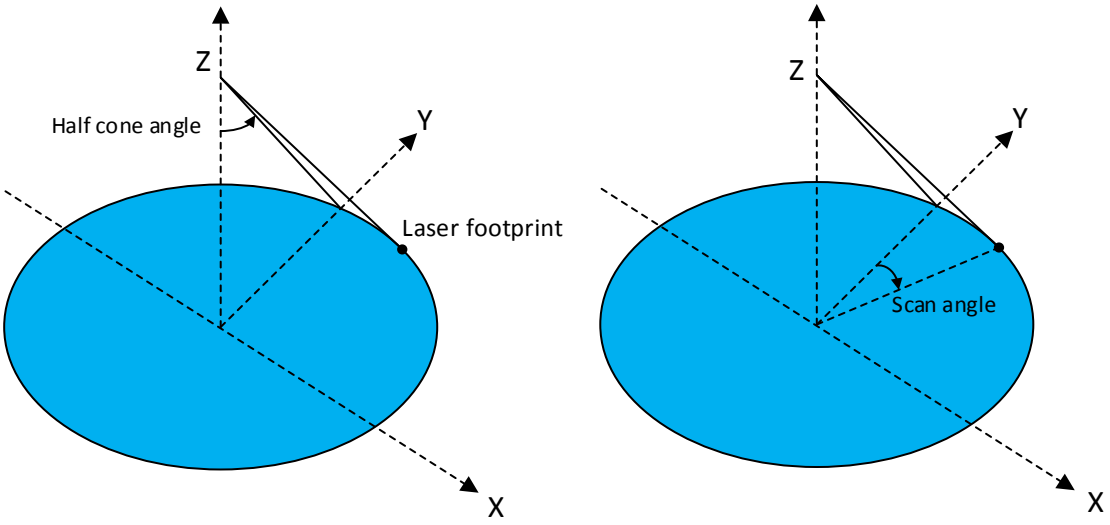

Figure 2-2 Overview of a circular scan pattern and definition of half cone angle and scan angle

2.2 Single photon LiDAR photodetector

One of the most significant differences between SPL and conventional LiDAR is the laser return detector employed. New detector technology enables SPL to be sensitive to a single photon event. In this section, two types of single photon detectors are introduced.

2.2.1 Geiger-mode APD

One of the two ways to detect single photon events is to use a Geiger-mode avalanche photodiode [52]. An APD is a variation of a P-N junction photodiode. When a P-N junction photodiode is reverse biased under a certain level, there will be an electric field in the vicinity of the junction that keeps holes to the P side and electrons to the N

side of junction. When an incoming photon of sufficient energy is absorbed in the region, an electron-hole pair is generated. Because of the existence of the electric field, the hole drifts to the P side and the electron drifts to the N side, resulting in a photocurrent. Note that electron-hole pair can also be thermally generated even without incoming photons and generate current, which is called dark current.

An APD operates with the above principles, however, they are also designed to support high electric fields. A high electric field will accelerate electron-hole pairs and provide them with sufficient energy after the incoming photon is absorbed. Then the electron (or the hole) collides with the crystal lattice and generates another electron-hole pair which can also generate new pairs. This process is called impact ionization. During this process, more and more electron-hole pairs are generated and this is the reason for the name "avalanche". Each absorbed photon generates on average a finite number of electron-hole pairs. This finite number is the internal gain of the detector which is usually about 10^2 – 10^3. This working mode is called linear mode because the resultant photocurrent is linearly proportional to the number of incoming photons.

If the reversed biased voltage is even larger than a limit, called the breakdown voltage, the electrons and holes multiply by impact ionization even faster than they can be extracted. The number of electrons and holes increases exponentially in time. In this case, a single photon event leads to an 'infinite' signal and a very high gain can be obtained, usually about 10^6 [29]. This working mode is called Geiger-mode and the output photocurrent is independent of the number of photons incident so that the magnitude of the input signal cannot be detected. After the detection of a photon event, the avalanche current needs to be shut off to re-arm the detector for the next detection.

This process is called quenching [48]. The reset time typically takes 10 to 100 ns and is called dead time. Figure 2-3 shows the photocurrent in these two working modes.

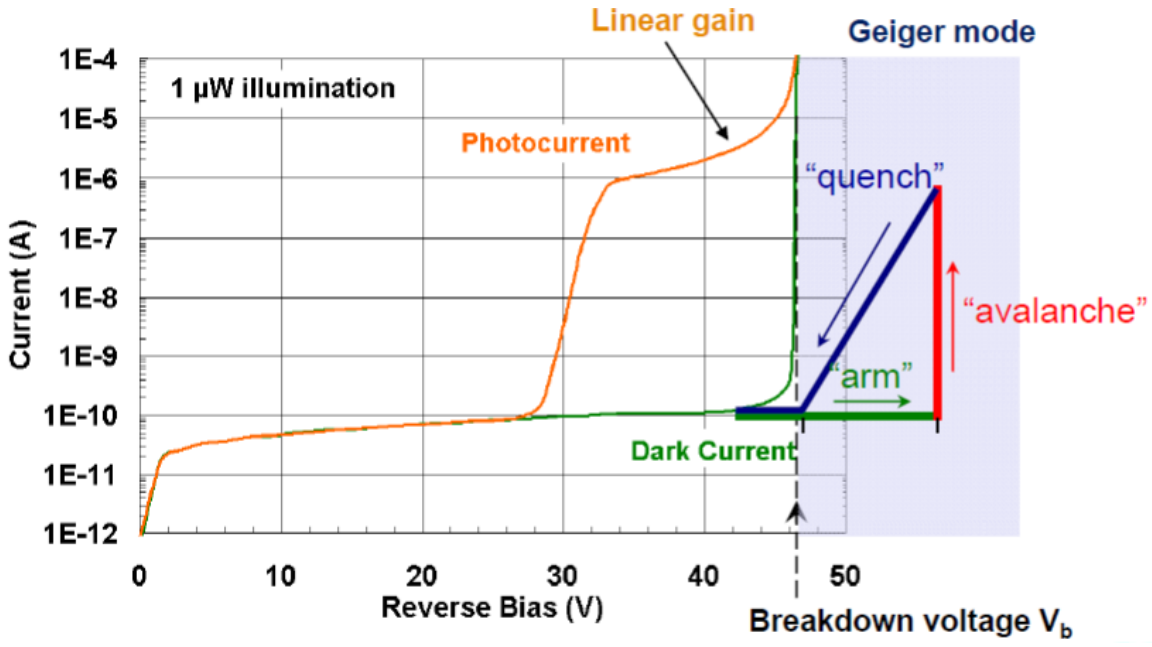

Figure 2-3 Relationship between photocurrent and reverse bias [53].

A recent advance in detection techniques using GmAPD is the silicon photomultiplier (SiPM) [54]. The basic structure of a SiPM is an array of microscopic APDs each working in Geiger-mode [55]. Each APD has an individual quench resistor and these pairs form a microcell. When a microcell responds to an incoming photon, a Geiger avalanche is initiated resulting in a photocurrent through the microcell. Then the voltage across the quench resistor drops and in turn reduces the bias voltage across the diode to a level lower than the breakdown voltage. During the avalanche process of one microcell, other microcells remain fully charged and are able to detect photons. The output of the detector is the sum of photocurrents from the individual microcells. Therefore, the magnitude of output photocurrent is proportional to the number of triggered microcells and is capable of providing information on the magnitude of incoming photon flux [56].

2.2.2 Microchannel Plate-Photomultiplier Tube

The other commonly used detector for single photon LiDAR is a microchannel plate-photomultiplier tube (MCP-PMT). A photomultiplier tube is a vacuum tube consisting of the following components: an input window, a photocathode, focusing electrodes, an electron multiplier and an anode which is usually sealed into an evacuated glass tube [57]. Figure 2-4 demonstrates the typical construction of a PMT.

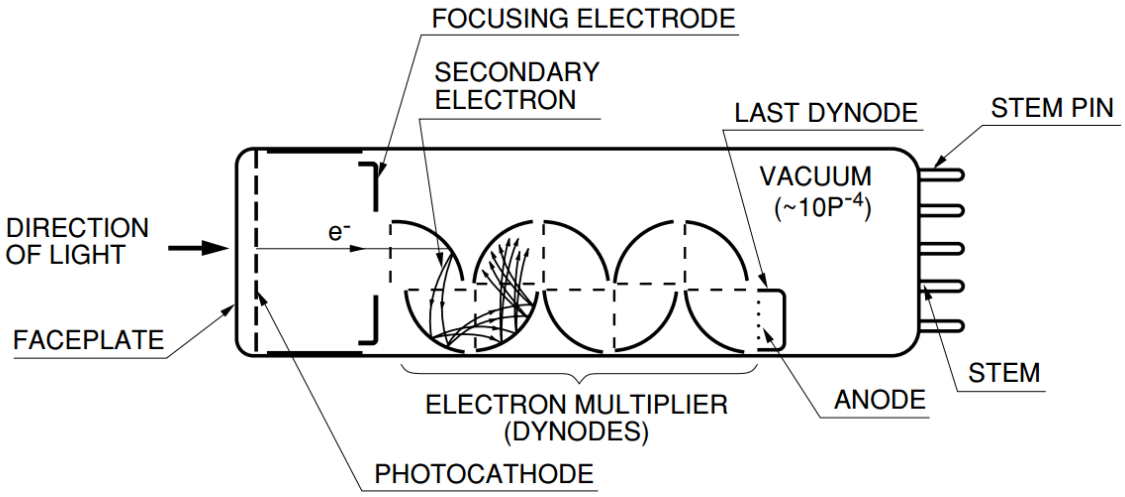

Figure 2-4 Construction of a photomultiplier tube [31]

When light enters a PMT, it passes through the input window first and then excites the electrons in the photocathode so that photoelectrons are emitted into the vacuum. This process is also called external photoelectric effect [58]. Photoelectrons are accelerated and focused by the focusing electrode onto the first dynode. Each photo electron liberates a number of secondary electrons which are accelerated and focused onto the next dynode. This process is repeated and finally the secondary electrons from the last dynode are collected at the anode.

With the emergence of microchannel plate (MCP), PMT have evolved into a more versatile device [31]. MCP-PMT employ a MCP to replace the conventional discrete

dynodes. This design makes the PMT able to measure wide-bandwidth down to the picosecond level and weaker incident light at the photon counting level. The schematic structure of an MCP is shown in Figure 2-5. An MCP is a thin disk with a two-dimensional array of glass capillaries (channels) bundled in parallel onto it. One single channel of it is very small with an internal diameter of 6–20 microns. The inner wall of each channel has the proper electrical resistance and secondary emissive properties so that it acts as an independent electron multiplier. When an electron enters a channel and impacts the inner wall, secondary electrons are emitted. Accelerated by the voltage across the both ends of the MCP, the secondary electrons then impinge the wall and generate additional secondary electrons. This process is repeated along the channel, resulting in a larger number of electrons at the other end of the MCP.

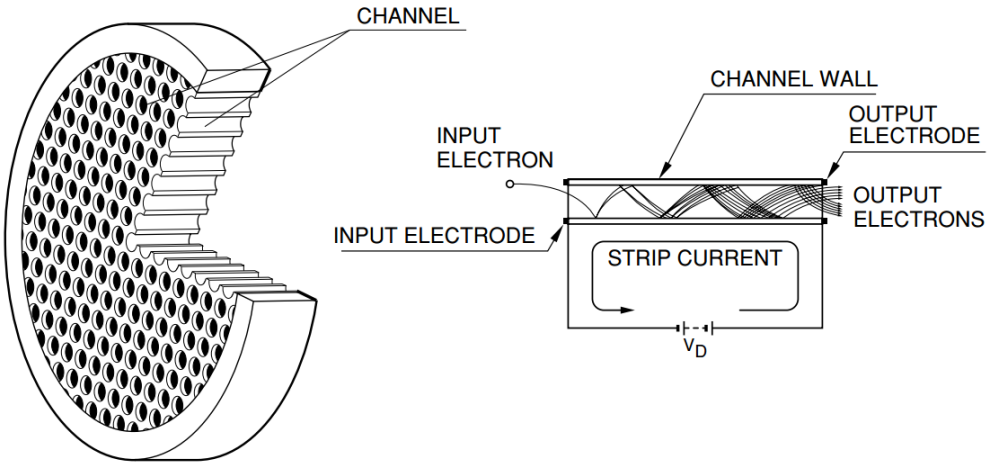

Figure 2-5 Schematic structure of an MCP and its principle of multiplication [31]

The new design of the MCP provides several benefits compared with conventional discrete dynodes design:

1) High gain despite compact size

2) Fast time response

3) Two-dimensional detection with high spatial resolution

4) Sensitive to charged particles

GmAPD and MCP PMT share a lot in common. They both have high gain to ensure single photon sensitivity, can be produced in compact size and have fast response to the incoming photons. SPL systems based on both of these detectors are currently implemented. The biggest difference between these two detectors are their respective dead times. The dead time of a PMT is much shorter than that of GmAPD. So systems with MCP PMT are able to record multi-stop events. However, the short dead time inevitably increases the data volume at the same time, and the recording speed of the timing hardware limits the size of detector arrays for PMT systems. This is partially the reason why current PMT system's detector array are only 10×10 [51] while GmAPD array can be as large as 32×128 [27]. For SiPM detectors, the biggest shortcoming is the high dark count rate which can make the final point cloud noisier than that from MCP PMT based systems [56].

2.3 Introduction to current single photon altimeters

2.3.1 NASA Multi-kilohertz Microlaser Altimeter

NASA's Multi-kilohertz Microlaser Altimeter (MMLA) was the first altimeter to use a single photon technique [22]. MMLA is an airborne multikilohertz microlaser altimeter developed by Goddard Space Flight Center under NASA's Instrument Incubator Program (IIP). The system was developed in December of 1998 and was first used for one engineering and two science flights in 2001. The typical flight height for MMLA is from 3.5 to 6.7 km. MMLA was designed to detect single photon returns reflected from

targets of interest and determine their height. The MMLA instrument utilizes a Polysci $3.5\,\mu J$, 532nm and 12 kHz microlaser. The beam and FOV (receiver field of view) are conically scanned at 20 Hz around a 2 degree cone to produce a swath along the flight path. MMLA is a proof-of concept instrument and the data collected by it demonstrated great potential for single photon techniques.

2.3.2 NASA ICESat-2

Satellite altimetry over the continental ice sheets has proven to be a valuable tool for studying decadal ice sheet elevation changes [59]. NASA launched the Ice, Cloud and land Elevation Satellite (ICESat) in 2003 to monitor interannual and long-term changes in polar ice-sheet volume [60]. ICESat has contributed significantly to human's understanding of ice sheets [59], [61]–[63]. The ICESat mission's primary instrument was Geoscience Laser Altimeter System (GLAS), which carried three 1064 nm Nd-YAG lasers. ICESat determined land surface vertical structure within laser footprints using received waveforms recorded by GLAS. The operating laser fired at a rate of 40 Hz and the laser illuminated a spot on the ground surface with a diameter of about 65 m. Successive spots were separated on the surface by 172 m [60]. Separation of the ICESat tracks is 15 km at the equator, 11km at mid-latitudes, and 2.6 km at 80 degrees latitude. ICESat finished its mission in 2009 and to continue this observation mission NASA will launch a new generation satellite, ICESat-2 in 2018 [64]. ICESat-2 will obtain point clouds of polar ice sheet elevations using the photon laser instrument from the Advanced Topographic Laser Altimeter System (ATLAS). ATLAS will split the outgoing laser energy into 6 beams, arranged in 3 pairs, with 3.3 km between pairs and 90m separation

between members of each pair (shown in Figure 2-6) [65]. The system will fire a green laser (532 nm) at a rate of 10 kHz.

For ICESat-2, single photon sensitive detectors makes it able to provide a much denser point cloud than its predecessor. With a repetition rate of 10 kHz at an altitude of 200km, ICESat-2 will produce footprints of nominally 14m diameter at 70 cm intervals along track. ICESat-2 data with better resolution and coverage will provide more observations for ice sheet study.

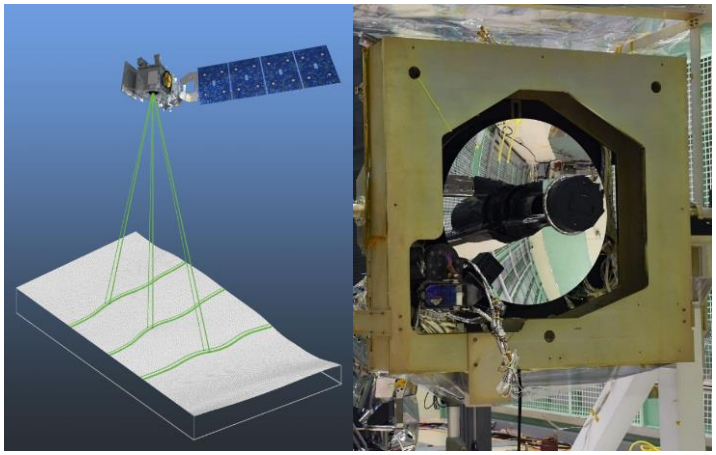

Figure 2-6 Ground track of ICESat-2 (left) and ATLAS instrument mounted on ICESat-2 (right) Credit: NASA Goddard Space Flight Center.

2.3.3 NASA MABEL

Given the different design of ICESat-2 compared with ICESat, the ICESat-2 project needed simulated data to verify the new instrument model, provide a detailed error analysis of the ATLAS measurement strategy and develop algorithms for the new data [66]. Consequently, the Multiple Altimeter Beam Experimental LiDAR (MABEL) [67] was developed.

The main instrument parameters for MABEL are shown in Table 2-1. MABEL uses a high-repetition-rate pulsed laser which can operate at repetition rates from 5 to 25

kHz; typical operations use 10 kHz to simulate ICESat-2. The systems fires both 1064- and 532-nm lasers to compare measurements at different laser wavelength. Because only one laser is used in MABEL, a splitter box is employed to split the output beam. The receiver has 105 fibers and will utilize up to 16 for 532 nm and up to 8 for 1064 nm returns.

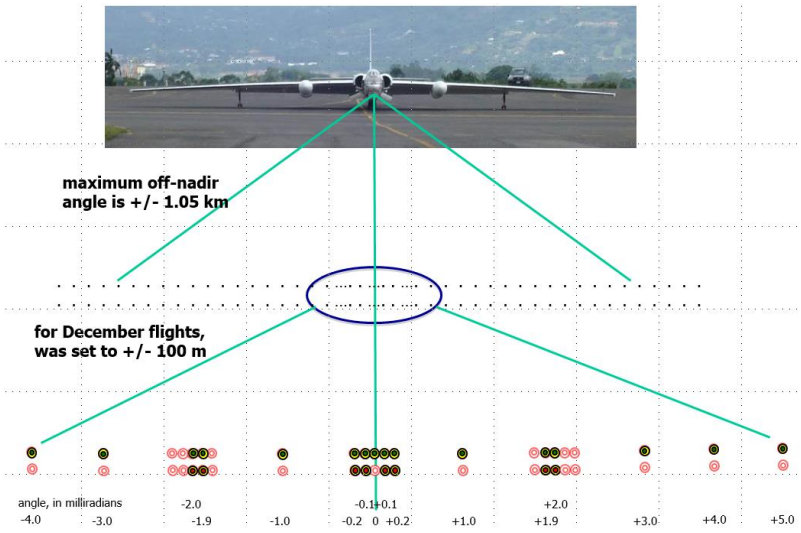

Figure 2-7 MABEL viewing geometry as defined by fiber arrays. If the outermost fibers are illuminated, the swath width would be 1.05 km [67].

Table 2-1 Main parameters for MABEL [67]

Parameter	Value
Operational altitude	20 km
Wavelength	532 and 1064 nm
Telescope diameter	12.7 cm
Laser pulse repetition frequency	Variable 5–25 kHz
Laser pulse energy	Variable, nominal 5–7 µJ per beam
Laser footprint ($1/e^2$)	100 µrad (2 m)
Telescope field of view	210 µrad (4.2 m)
Filter width	532 : ~150 pm 1064: ~400 pm
Detector efficiency	532: 10%–15% 1064: 1%–2%
Swath width (variable)	Up to ±1.05 km

The electronics of MABEL were custom developed by Sigma Space Corporation. The time-tagging electronics have a measured resolution of 83 picoseconds which is

smaller than the ICESat-2 requirement of 150 picoseconds. A Novatel model HG1700 inertial measurement unit (IMU) is used to ensure accurate determination of instrument pointing. The MABEL instrument was flown aboard the ER-2 aircraft on several missions above various earth surfaces between 2010 and 2014 at different times of the day [68]. MABEL datasets can be openly accessed from the NASA website (https://icesat.gsfc.nasa.gov/icesat2/data/mabel/mabel_docs.php). Each dataset contains one minute of data which corresponds to a ~12000 m profile. The data includes 16 channels of 532 nm returns and 8 channels of 1064 nm returns. The geometry of MABEL data collection is shown in Figure 2-7. MABEL data will be one of the experimental datasets examined in this dissertation and used to test new filtering algorithms.

2.3.4 NASA SIMPL

The Slope Imaging Multi-polarization Photon-counting LiDAR (SIMPL) is a polarimetric, two-color, multi-beam push broom laser altimeter developed by NASA Earth Science Technology Office (ESTO) Instrument Incubator Program (IIP) [69]. The purpose of the development of SIMPL was to demonstrate new altimetry capabilities for combining elevation measurements and ground surface information.

Figure 2-8 provides an overview of the functional block diagram of the SIMPL instrument. SIMPL utilizes a high repetition rate (11 kHz), short-pulse (1ns) laser with a wavelength of 1064 nm. Part of the near infrared (NIR) beam is frequency doubled to 532 nm. The output of SIMPL is 4 linearly polarized beams with both NIR and Green lasers in each beam. The receiver filter divides the two wavelength returns into separate paths and produces 16 channels (four color/polarizations states on the four beams). The return

signal is fiber coupled into sixteen single-photon counting modules to determine range to the target.

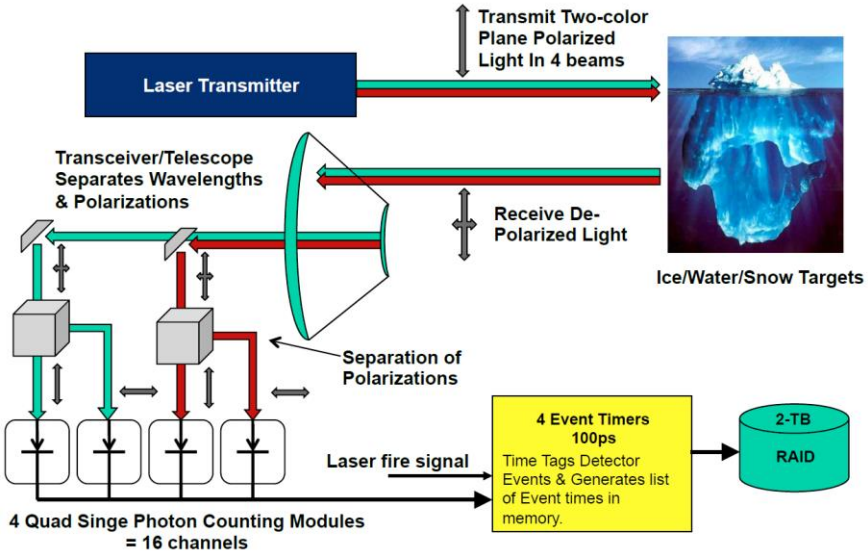

Figure 2-8 Pushbroom photon counting laser altimeter measurement approach using multiple fiber lasers, single photon counting detectors [70].

2.4 Introduction to current 3-D imaging SPL

In this section, we will introduce the current state-of-art 3-D imaging single photon LiDAR systems. The common characteristics of such systems are the use of a single photon detector array and utilization of a scanning mechanism. With this design, 3-D imaging SPL can rapidly generate dense point clouds of the target area.

2.4.1 MIT Lincoln Laboratory Jigsaw

To meet the critical requirements for accurate target identification for successful battlefield management, the Defense Advanced Research Projects Agency (DARPA) initiated development of the Jigsaw program [71]. The goal of this program was to develop high-resolution 3-D imaging laser radar sensor technology and systems that can be utilized to detect hidden military ground targets. Lincoln Laboratory, Harris

Corporation and Sarnoff Corporation formed a team to develop the sensor system, data processing algorithms and visualization applications.

The Jigsaw sensor uses Lincoln Laboratory-developed microchip laser technology. The microchip laser transmits short laser pulses at a pulse rate of 16 kHz and at a wavelength of 532 nm. The detector technology was also developed at Lincoln Laboratory. The focal-plane array is comprised of 32x32 silicon Geiger-mode APDs with digital time-of-flight counters at each pixel [72]. Figure 2-9 demonstrates the APD detector array and the detector-cooler combination. The system was mounted on a UH-1 helicopter and tested for foliage penetration. Military ground vehicles hiding under foliage can be successfully detected with the collected data.

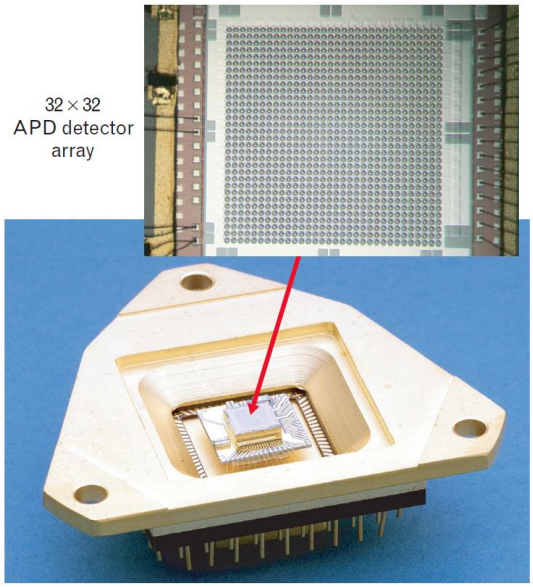

Figure 2-9 The 32x32 Geiger-mode avalanche photodiode (APD) detector array, mounted on a thermoelectric cooler. This unit was hermetically sealed into a detector package to stabilize the detector's operating temperature near 20 °C [72]

2.4.2 MIT Lincoln Laboratory ALIRT

Airborne Ladar Imaging Researching Testbed (ALIRT) is a medium altitude mapping LiDAR system developed and fabricated at MIT Lincoln Laboratory [73]. The

system utilizes a pulsed microchip laser and a 32×128 focal plane array of Gm-APDs to generate a 3-D point cloud. The system overview is given in Figure 2-10. ALIRT is mounted on a Sabreliner – 40 jet and typically collects data at 10 – 15 kft above ground level. Principal applications of ALIRT were first demonstrated during post-earthquake mapping in Haiti in January 2010 [74]. The ALIRT system rapidly mapped cities and towns after the earthquake providing humanitarian assistance teams valuable local 3-D information.

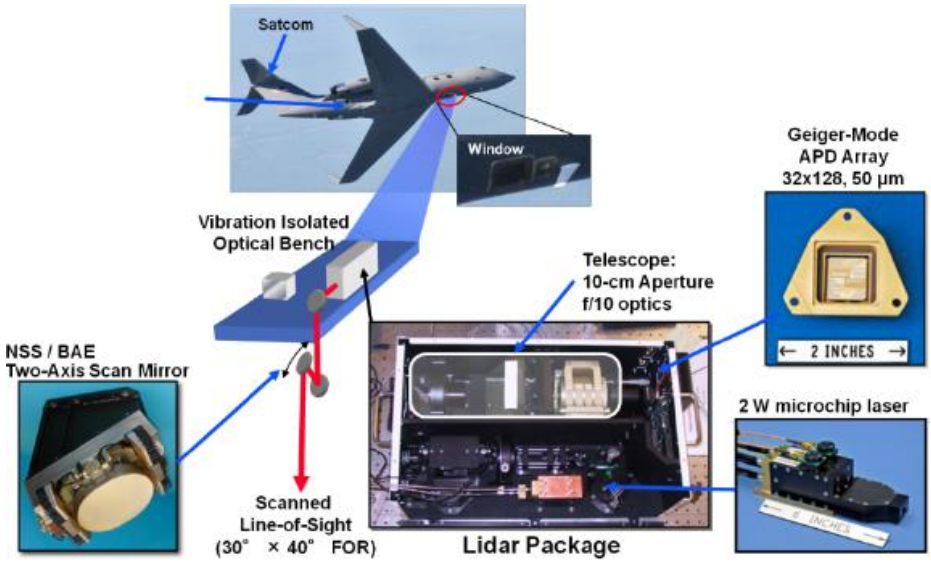

Figure 2-10 The ALIRT 3-D laser radar system and associated hardware. Credit: MIT Lincoln Laboratory.

2.4.3 CATS

The Coastal Area Tactical-mapping System (CATS) was developed by the University of Florida along with Fibertek, Inc. and Sigma Space Corporation [47]. The long-terms goal of the CATS is to gain an understanding of Earth terrain and shallow bathymetry under very low energy laser probing. The CATS instrument works at low power and a low laser pulse rate while obtaining contiguous ground coverage at a resolution of a few decimeters.

CATS uses a frequency-doubled Nd:YaG laser, operating at 532 nm in order to obtain shallow water penetration for bathymetry and submerged target detection. Each pulse is separates into a 10×10 square array by a holographic diffraction element [75]. The return light is refocused by a telephoto lens before being imaged onto separate cathodes of a 10×10 segmented anode photomultiplier tube. CATS utilizes a micro-channel plate photomultiplier tube (MCP-PMT) which can amplify single photon events with a gain of 10^5 with 200 picoseconds rise time and 200 picoseconds dead time [75]. The nominal flying altitude of CATS is 600 m and the expected horizontal spatial resolution of the system at nadir looking is 20 cm. The system is shown in Figure 2-11.

Figure 2-11 CATS and related components. View of sensor mounted on tripod with laptop and power supply components (left). Output window, enclosed scanner, electronics cube, enclosed optical components (right) [75].

2.4.4 Sigma Space Corporation's HRQLS/SPL100

The High Resolution Quantum LiDAR System (HRQLS) was a self-funded development by Sigma Space Corporation [51]. The goal of the development was to provide a sensor capable of mapping larger areas more quickly via a combination of higher air speeds and wider swaths.

The main parameters of HRQLS are given in Table 2-2. Using an external dual wedge scanner at the output of the 3 inch telescope, HRQLS can scan the target area with full cone angles between 0 and 40 degrees. With a laser repetition rate of 25 kHz, HRQLS can acquire 2.5 million ground points per second. HRQLS employs multiple focused laser beamlets. A diffractive optical element (DOE) breaks the spatially Gaussian green laser beam into a quasi-uniform 10×10 array of Gaussian spots at the target [76]. The beamlets pattern is shown in Figure 2-12. Single photon returns from individual beamlets are imaged onto a 10×10 MCP-PMT detector. Each pixel output is input to an independent channel of a high resolution (<100 picoseconds), multi-stop timer. The laser operates at 532 nm, so that shallow water bathymetry can also be detected by HRQLS. The recovery time of MCP-PMT is as short as 1.6 ns (24cm), allowing multi-ranging capability from HRQLS [77].The fast recovery allows daytime operation with large range gates and improves penetration through partial obscurants such as ground fog, dust, vegetation and water columns.

The SPL100 system is an updated version of the HRQLS. The SPL100 system uses a 10 by 10 array of SiPM detectors instead of the MCP PMT used in HRQLS. The parameters related to filtering for the new system remains the same as those of HRQLS. In Chapter 5, we will discuss filtering methods for 3-D imaging LiDAR. HRQLS and SPL100 data will be used as the experimental data to test the performance of the developed filtering algorithms.

Table 2-2 Main parameters for HRQLS Credit: J. Marcos Sirota

Parameter	Specification
Beams	100
Wavelength	532 nm
Laser Repetition Rate	25 kHz
Laser Pulse Width	200 picosecnds
Laser Output Power	1 w
Pixels/sec	2.5 Million
Eye safety	Eye safe by FAA standards
Multiple Return Capability	Yes
Pixel Recovery Time	1.6 nsec
RMS Range Precision	±5 cm
Scan Patterns	Linear, conical
Scan Width	0 to 40 degrees (selectable)
Operational Altitude Range	6.5–10 Kft
Swath vs AGL	1.3 to 2 km
Areal Coverage vs AGL(200 Knots)	400 to 640 km^2/hour single pass
Mean Point Density	12 per sq meter, single pass
Size	19 W×25 D×33 H inches
Weight	80 lbs
Prime Power	555 W

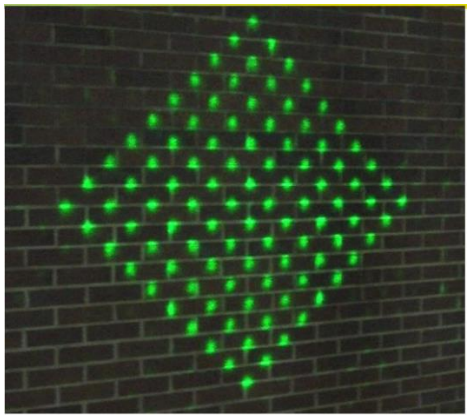

Figure 2-12 Beam pattern of HRQLS. 100 beams in a 10×10 array illuminated on the wall Credit: Kristofer Shrestha.

Chapter 3

Review of Current Filtering Algorithms

The use of single photon techniques can be traced back to the 1960s with Lunar Laser Ranging [78], but SPL had not appeared in commercial LiDAR sensors until recently. Noise filtering methods for SPL have not been well studied to date, as evidenced by the very limited number of publications on this topic. In this chapter, we will review current filtering algorithms for single photon laser altimetry and 3-D imaging LiDAR. Note that the filtering methods for single photon laser altimetry can also be used in 3-D imaging SPL data. The only difference is that the clustered beamlets of a 3-D imaging SPL system can provide additional spatial correlation information that can be used to improve filter performance. We will describe algorithms for single photon laser altimetry and then introduce methods for 3-D imaging SPL.

3.1 Filtering algorithms for laser altimetry

3.1.1 Image-based filtering method

Awadallah, et al. [79] proposed a method to extract ground and forest canopy curves from discrete laser altimeter data using an active contour model. This method first maps 3-D points onto a two-dimensional binary image and then two image processing algorithms are implied to the binary image. The first method is an open-curve model which transforms the initial curve repeatedly using an energy minimization process; a greedy algorithm is used to search for a solution. Two initial contours are used in this method, one from the top and the other one from the bottom, and ends with the top

contour converged to the top of canopy (TOC) and the bottom one converged to the ground surface. This approach has a very fast convergence speed and high computational efficiency. The other model used in this paper was a more robust algorithm known as the geometric active contour (GAC) model. Unlike the open-curve model, the output of the GAC model is a closed contour or possibly several closed contours. In the proposed approach, the upper most points from the contour at selected columns of the image are assigned to the TOC and the lowest points are assigned to the ground surface. In [65], an enhanced version of the GAC model is proposed. An additional process that refines the initial surfaces is introduced to ensure a more robust result.

While converging fast, the open-curve model is very sensitive to noise. In areas with a high noise level, the open-curve model results are not very good. The GAC model, though not computationally efficient, is more robust to noise. However, there are still some other problems with these two approaches; first both of these models are image processing algorithms, which means that 3-D LiDAR data must be rasterized first; however, the influence of the rasterization is not discussed in [65], [79]. A large pixel size will include more noise points while a small cell size may cause discontinuous signal points resulting in several contours in the final product. This method also only extracts the top line of the canopy and the ground line. There are still noise points located between these contours. In applications where all vegetation points need extraction, this method will be insufficient.

Another image-based filtering algorithm is the Canny Edge Detection (CED) method proposed by Magruder et al. [45]. Canny Edge Detection is a classical algorithm for image processing [80]. It uses a Gaussian first derivative to filter data and locate

edges. In Magruder's method, the 3-D point cloud is first rasterized to an image. The value of each pixel is assigned as the point density within each cell. The cell size is the square root of the number of points in the along-track flight direction. A Gaussian filter is applied to broaden the edges of the high density and the noise pixels. The gradient for each pixel is computed in both magnitude and direction, and with the resulting gradient map, an empirical threshold can be determined and used to remove noise pixels.

For image processing, active contour and Canny algorithms are both used to detect edges in the image. In fact, the theory behind these two methods are similar, they both convert the point cloud to an image and try to find the boundary between signal and noise. One potential problem is that it is hard to find an optimal cell size to rasterize the data. An arbitrary choice may cause both signal points and noise points to be assigned to the same cell.

3.1.2 Density-based filtering methods

Herzfeld et al. [43] proposed a method using spatial statistics to detect the ground and canopy height. The first step was to generate a histogram of elevation values for all the detected photons. The histogram is grouped into 100 elevation bins for a total range of 100m. A low-pass Butterworth filter,

$$\begin{aligned} a &= \left(a_1, a_2, a_3, a_4, a_5\right) \\ &= \left(0.00625, 0.25, 0.375, 0.25, 0.0625\right) \end{aligned} \tag{3.1}$$

is used to smooth high-frequency wiggles in the histogram. From the filtered histogram, two hypermaxima can be extracted which will represent the ground and canopy elevation centers. After the ground and canopy elevation centers are determined, the data can be segmented into 3 classes, a canopy range set, a ground range set and a remaining class.

Then for the canopy and ground sets, density values for each point are calculated using a radial basis function. A histogram of the density values for photon events is generated and filtered with another Butterworth filter. Finally, the largest density count in the histogram is used as a threshold to filter noise. The proposed method also includes some other mathematical concepts and more details can be found in the paper. However, the basic idea is still to calculate the density of returns in a circle with a predefined radius. This will inevitably encounter problems in selecting an optimal circular radius and will have a high computational burden.

Zhang et al. [41] proposed the modified density-based spatial clustering of applications with noise (mDBSCAN) algorithm to filter single photon laser altimetry data. For the conventional DBSCAN algorithm, the key idea is that for each point in a cluster, the neighborhood, determined by a given radius, has to contain a minimum number of points. In other words, for a circular area centered at the query point, the point density has to exceed some threshold. The proposed mDBSCAN method considers the fact that the ground surface and canopy returns are distributed more horizontally than vertically. Therefore instead of using a circle to examine point density, an ellipse is employed (shown in Figure 3-1). For this method, the estimation of the noise threshold is very important. In [41], a heuristic way was developed to estimate this parameter. Several ellipses were randomly selected from the data and the average point densities of each were calculated. The threshold was then set to be 4 times the average point density. The mDBSCAN method is very computationally efficient and provides good result in many cases. However, this method has several drawbacks. First, it is based on an assumption that the point density of the data is homogeneous, which might not always be true. This

will be discussed in detail in Chapter 4. Second, it is hard to prove that the threshold chosen is an optimal one; this is a common problem for density-based methods. Finally, mDBSCAN considers only the horizontal distribution of ground and canopy, using a horizontal ellipse for the nearest neighbor search. However, this assumption may not be valid in areas with high slopes such as mountains and urban environments.

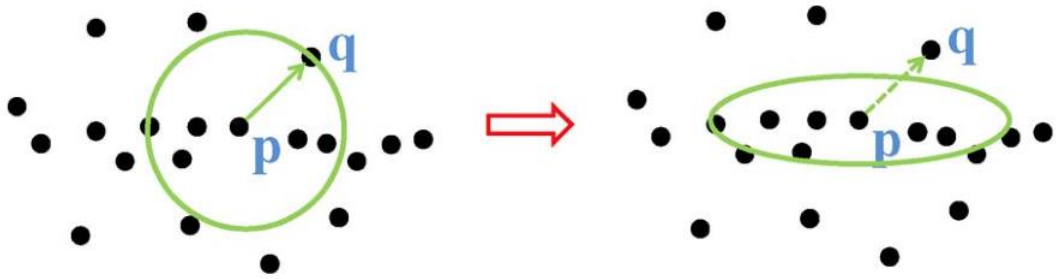

Figure 3-1 Modification of search area using DBSCAN. In the left image, by using a circular searching area, point q is used to estimate the local density of point p. On the other hand, in the right image, q is used to determine the density at point p, when an ellipse is used [41].

3.2 Filtering algorithms for 3-D imaging LiDAR

The return signal from a 3-D imaging LiDAR forms an array which can be regarded as a cluster of a large number of laser altimetry measurements. The corresponding illuminated area on the ground is usually small. In this case, there are strong spatial correlations between points in the area imaged by the 3-D array, which can be used to improve the performance of the filter. In this section, some filtering algorithms that consider the true 3-D nature of the SPL data are reviewed.

3.2.1 A real-time noise filtering strategy

Zhang et al. [42] proposed a real-time noise filtering strategy for 3-D imaging LiDAR. The proposed method considers the fact that surfaces for most targets of interest are continuous; the ranges of the target surface corresponding to the adjacent pixels are very close and therefore the temporal differences of the echo signals on the adjacent pixels is small. However, noise will be randomly distributed everywhere. By calculating the return rate of these adjacent pixels, the echo signal will be distinguished from noise with a proper threshold.

In [42], a 3×3 pixel array was used as a unit to detect signals, which means the threshold should be between 1 to 9. The selection of a proper threshold is discussed in the paper. The equation for the optimal threshold is derived, however, it is too complicated to obtain an analytical solution. A numerical result is provided instead to select a proper threshold for different signal and noise intensities.

A box next to a wall was used in the experiment described in [42], and a clean point cloud was obtained with the proposed algorithms, which indicates that the method works well for flat well-conceived scans with only hard targets. However, in other areas such as tree canopies, this method may encounter problems. The return signal from the canopy top is not homogeneous and not as strong as that from the ground. So employing a constant threshold will result in a high probability of misclassifying signal points from the canopy.

3.2.2 Two-step classifier

Cossio [81] proposed a two-step classifier. The local spatial correlation of signal events is first exploited to filter out noise, followed by classification of target points using a surface based scheme. In the filtering step, two parameters D_1, D_2 are considered to determine spatial correlation with the following equations:

$$\begin{aligned} &\left|z_k - z_l\right| < \frac{D_1}{2} \; and \\ &\left(x_k - x_l\right)^2 + \left(y_k - y_l\right)^2 < D_2, \end{aligned} \tag{3.2}$$

where $\left(x_k, y_k, z_k\right)$ are the geo-centric coordinates for the query point r_k, and $\left(x_l, y_l, z_l\right)$ are the geo-centric coordinates for the neighbor points of r_k. The neighbor points which fit these two criteria are regarded as correlated points. The numbers of correlated points are then used to determine whether the query point is signal or noise. In reality, these two criteria form a cylindrical volume around the investigated point. This method can be regarded as an expansion of the density-based method for laser altimetry data in 2-D, a 2-D circle extruded to a cylinder in 3-D.

3.2.3 Differential cell count method

Degnan [23], [51] proposed a differential cell count (DCC) method based on a post-detection Poisson analysis. The DCC method filters the SPL data by processing each shot individually. For each shot, the histogram of elevation of each point is generated with a 30 m bin. The bin with the highest count and the two adjacent bins are retained. Points in the rest of the bins are used to estimate a noise rate. Then in the second stage, a

smaller bin size (usually 5 m) is applied. With the estimated noise rate from stage 1, the optimum threshold is calculated by

$$K_{opt} = \frac{N_S + \ln(N_{bin})}{\ln(N_S / N_b)}, \tag{3.3}$$

where, K_{opt} is the optimum bin threshold. N_S is the number of signal points which is estimated as the mean number of points in the three candidate bins, N_b is the number of noise points and is calculated by subtracting N_S from the total number of points in the three candidate bins. N_{bin} is the number of bins within the whole range gate. Then bins with point counts larger than the optimum threshold are retained.

DCC method works on the level of each data bin thus it has a very high computational efficiency. However, it regards all the points in one data bin as either signal points or false returns, which leaves near-signal noise unfiltered.

3.2.4 Multi-level filtering approach

Swatantran et al. proposed a multi-level filtering approach [82]. The method is based on two basic assumptions: 1) noise returns are randomly distributed in space while signal points are clustered together; and 2) signal points have higher point densities than solar noise returns. Three levels of filters are used in this approach. The first filter uses a 30 m vertical range bin to extract the highest density signals which includes both topographic and canopy features. In addition, a 30 m bin both above and below this initial bin is selected to guarantee no structural features are missing. Therefore a 90 m vertical subset of the raw data along the topographic range is extracted for further processing. The second filter divides the subset of data into 3 m voxels. The returns in a voxel are

determined as noise if the total count in the cubic window surrounding it (27 voxels) is less than an empirical threshold (30 points). This step roughly filters most of the noise returns. In the last filter, a smaller voxel size of 1 m and a lower threshold are used to refine the filtering results. The use of the 1 m voxel can remove isolated noise points along boundary layers.

3.3 Summary

For single photon LiDAR, the data capture electronics poll the detector voltage output and record only binary events. There is no strict intensity measure in the basic SPL design, as is typically found in conventional LiDAR systems. The only information in the dataset is the position of each point. All the methods introduced in this chapter try to distinguish signal from noise using point density. The basic idea of the image-based methods are to regard the point density as the intensity in an image. Density-based methods try to define a specific region around a query point and count the number of points inside the region. These methods inevitably encounter two problems. The first problem is rasterization, either rasterizing the data into 2-D pixels or a 3-D grid. The size of the pixel or grid is determined empirically and may not always work and periodically requires human intervention for filter tuning. The other problem is the assumption of static noise density. Both image-based and density-based methods require point density as an important parameter. However, the noise and signal density may change in some cases, for example, changing reflectivity, inconstant flying speed of the platform, changes in ambient background lighting or longer illuminated time on the target. The changing noise rate can cause false alarms and filter failure. In the next chapter, a novel filtering

method for SPL altimetry data is proposed which aims to solve these problems by compensating for varying noise levels in the raw point cloud.

In the following chapters, Chapter 4 introduces a new filtering method dealing with single photon altimetry data. Chapter 5 and 6 focus on filtering 3-D imaging single photon LiDAR data. And in Chapter, afterpulse removal will be discussed.

Chapter 4

A Novel Filtering for Single Photon Laser Altimetry Data

In this chapter, we propose a novel filtering algorithm to remove noise points in single photon laser altimetry data. As discussed in Chapter 3, since there is no intensity information, only point density can be used to filter the SPL data. Most of the current filters are based on the fact that the signal points are clustered and noise points are distributed sparsely. However, the current filters work in a direct way: they define a region around the investigated point and count the number of neighbors. This method, however, is highly dependent on the local noise characteristics of the data set. To mitigate this limitation, we instead interrogate the point density-based filter using the distances to the *k*-th nearest neighbors (KNN) [83]. A probability distribution function for the noise photons is therefore developed instead of applying an arbitrary hard distance threshold. This chapter is a summary of the work published in [83].

4.1 Algorithm

4.1.1 Noise density scaling

A noise density scaling of the raw single photon point cloud will enhance the application of the proposed algorithm. Varying noise density is common in a single photon LiDAR data set due to the following features: varying atmospheric conditions during the flight, changes in the topographic return surface reflectance, and variations in aircraft speed and elevation. The inconsistent noise density limits the effectiveness of density-based noise detection. Therefore, it is important to first adaptively scale the noise

level of the received photons according to its estimated temporal noise rate. Since it is hard to extract signal points from the raw data directly during data collection, the system usually records data with a longer time gate to make sure that all the signal points from the area of interest are recorded. Usually, a region where no signal points are located can be found and used as a sample region, for example, the top or the bottom part of the vertical data profile. We can then count the number of points, N_s inside this area. So the noise level can be estimated as

$$N_w = N_s L / L_{sample}, \tag{4.1}$$

where L is the length of the whole range gate and L_{sample} is the length of the sample region along the range direction. With the estimated noise level, the points can be rescaled proportionately by multiplying by the corresponding time varying noise rate estimate. There is no strict rule for the choice of L_{sample}, however, as long as the sample contains no signal points, a larger sample should improve the estimation of noise level.

4.1.2 Derivation of distribution of distance to KNN

We use the distance from a query point to its KNN to discriminate noise photons after the adaptive noise scaling described in Section 4.1.1. Finding the nearest neighbors is a fundamental problem in a wide range of applications, including Bayesian classifiers and big data searches. There are several ways to derive the distribution of the KNN distance. Herein, we apply the method introduced in [84] to derive the distribution of distances between a point and its KNN in a 2-D space. Assuming that all points are distributed in the space evenly and randomly, the pdf (probability density function) of the distance r to the KNN $f_{ideal}^{k}(r)$, can be derived with the following steps. Consider two

co-centric circles with radius of r and $r+dr$ centered at the query point as shown in Figure 4-1.

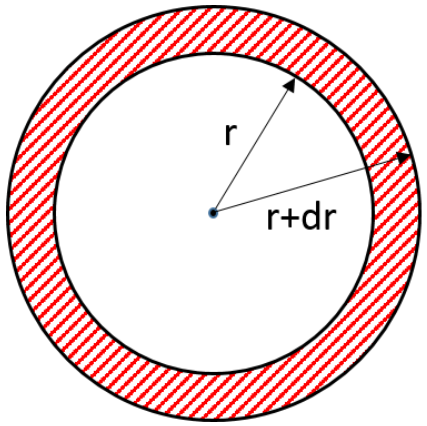

Figure 4-1 Two co-centric circles with radius r and r+dr. The *k*-th neighbor should fall in the red area.

The probability that the *k*-th nearest neighbor is located within the ring area from r to $r+dr$ is equivalent to the first $(k-1)$ nearest nodes being located within r and the k-th nearest neighbor within r and $r+dr$. From [84] equation (4.2) - (4.4) are given as

$$\begin{aligned} f_{ideal}^{k}(r)\,dr &= \Pr\left[(k-1)\,in\ r \mid N-1\right]\times \Pr\left[1\,in\,(r,r+dr) \mid N-k\right] \\ &= \left\{\binom{N-1}{k-1}\left(\frac{\pi r^2}{A}\right)^{k-1}\left(1-\frac{\pi r^2}{A}\right)^{N-k}\right\}\times \\ &\left\{\binom{N-k}{1}\left(\frac{\pi}{A}\left(2rdr+(dr)^2\right)\right)\left(1-\frac{\pi}{A}\left(2rdr+(dr)^2\right)\right)^{N-k-1}\right\}, \end{aligned} \tag{4.2}$$

where A is the area of the whole space, N is the number of points, and $k=1,2,\ldots,N-1$.

Therefore, the pdf of the *k*-th nearest neighbor at a distance r is given as

$$
\begin{aligned}
& f_{ideal}^{k}(r) = \\
& \lim_{dr\to 0}\frac{1}{dr}\left[\binom{N-1}{k-1}\left(\frac{\pi r^2}{A}\right)^{k-1}\left(1-\frac{\pi r^2}{A}\right)^{N-k}\times\right. \\
& \left.\binom{N-k}{1}\left(\frac{\pi}{A}\left(2rdr+(dr)^2\right)\left(1-\frac{\pi}{A}\left(2rdr+(dr)^2\right)\right)\right)^{N-k-1}\right] \\
& = \frac{2\pi r(N-k)}{A}\binom{N-1}{k-1}\left(\frac{\pi r^2}{A}\right)^{k-1}\left(1-\frac{\pi r^2}{A}\right)^{N-k}.
\end{aligned}
\tag{4.3}
$$

For a large N, this equation can be approximated as

$$
f_{ideal}^{k}(r) = \frac{1}{(k-1)!}2(\alpha\pi)^{k} r^{2k-1} e^{-\alpha\pi r^2}, \tag{4.4}
$$

where $\alpha = N/A$ is the average point density. The derivation can be validated by applying a Monte Carlo simulation (see Figure 4-2). 10000 points were generated randomly in a 10 m×10 m square area. Both coordinates of a point are subjected to a uniform distribution ranging from 0 to 10. The distance from a query point to its first and second neighbor is calculated and binned into 20 groups. The frequency of each bin, which is calculated by dividing the count in a bin by the whole number of points, is then converted to the probability density by dividing by the bin size. The red line in Figure 4-2 is plotted using equation (4.4) using *k* values of 1 and 2. We can see that the simulated probability density matches the theoretical one very well.

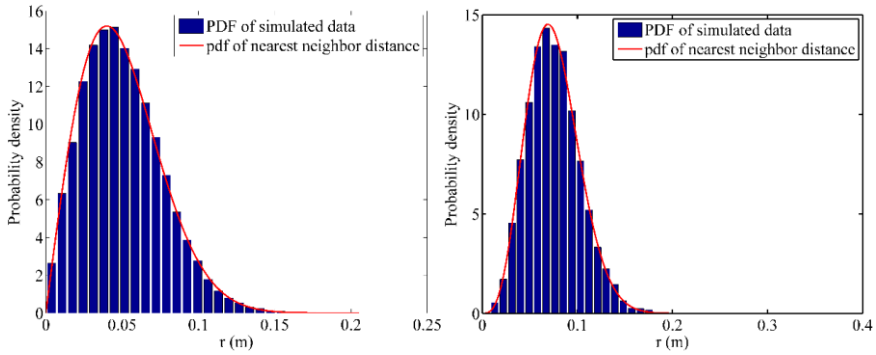

Figure 4-2 Simulation results of distribution of distances to 1st and 2nd nearest neighbor.

4.1.3 Data filter based on Bayesian decision theory

To filter the data into signal and noise returns we apply a Bayesian decision technique after the determination of the probability of the *k*-th nearest neighbor. Assuming that there are n_N noise points in the datasets already identified, then the prior probability of noise photons is given as $P(\omega_1) = n_N / n_{tot}$, where n_{tot} is the total number of points in the dataset. The prior probability of the signal photons is given by $P(\omega_2) = 1 - P(\omega_1)$. The noise photon density is determined as $\rho_N = n_N / A$, where A is the total area. The density of signal points cannot be estimated directly because the area of the signal is unknown a priori. Usually a number of areas can be selected to estimate signal to noise ratio. For each detected return, R_k is the distance to the k-th nearest neighbor return, and the posterior probability can be determined with the following equations:

$$
\begin{aligned}
P_k(\omega_1 \mid r = R_k) &= \frac{p_k(R_k \mid \omega_1)\, p(\omega_1)}{p(x)}, \\
P_k(\omega_2 \mid r = R_k) &= \frac{p_k(R_k \mid \omega_2)\, p(\omega_2)}{p(x)} \quad \textit{and} \\
p(x) &= \sum_{j=1}^{2} p_k(R_k \mid \omega_j) p(\omega_j),
\end{aligned}
\tag{4.5}
$$

where $p_k(R_k \mid \omega_j)$ is obtained from equation (4.4) using distance R_k. To enhance the capability of detecting noise photons, we examine the posterior probability of the nearest 20 neighbors. Selection of the number of neighbors is data driven and empirical. Usually,

a number from 12 to 20 is suggested. We then get a combined posterior $P_{N,i}$ of the *i*-th point in the dataset using the following equation:

$$P_{N,i} = \prod_{k=1}^{20} P_k\left(\omega_1 \mid r = R_k\right). \tag{4.6}$$

With the known estimated number of signal photons, we select the smallest n_S signal photons to adaptively filter out the noise photons.

4.2 Experimental data set

A NASA MABEL dataset is used to test the performance of the proposed filtering algorithm. As mentioned in section 2.3.3, the dual MABEL laser beams at 1064 and 532 nm are split into eight 1064-nm and sixteen 532-nm beams, each with a separate single photon detector. The time and position of each individual received photon are recorded. With the travel time of each photon and the positional information provided by the onboard Global Navigation Satellite System and inertial navigation system, we can obtain 3-D locations of each recorded return. We used two MABEL data sets obtained on August 2, 2014, near San Luis Obispo, CA, and on September 26, 2013, near New Madrid, MO. Two linear-mode airborne LiDAR data sets were downloaded from OpenTopography (www.opentopography.org) as ground truth for the final filtered MABEL datasets. The reference data sets were collected in March 2011 for the CA data and in September 2010 for the MO data, each with a point density of nine points per square meter. The terrain types for the CA and MO data are mountainous and bare ground, respectively. While the MABEL and airborne LiDAR collections were not at the same time, they were in remote regions, and therefore, we would expect no significant

differences between the terrain profiles. A profile of the raw CA and MO MABEL data is shown in Figure 4-3.

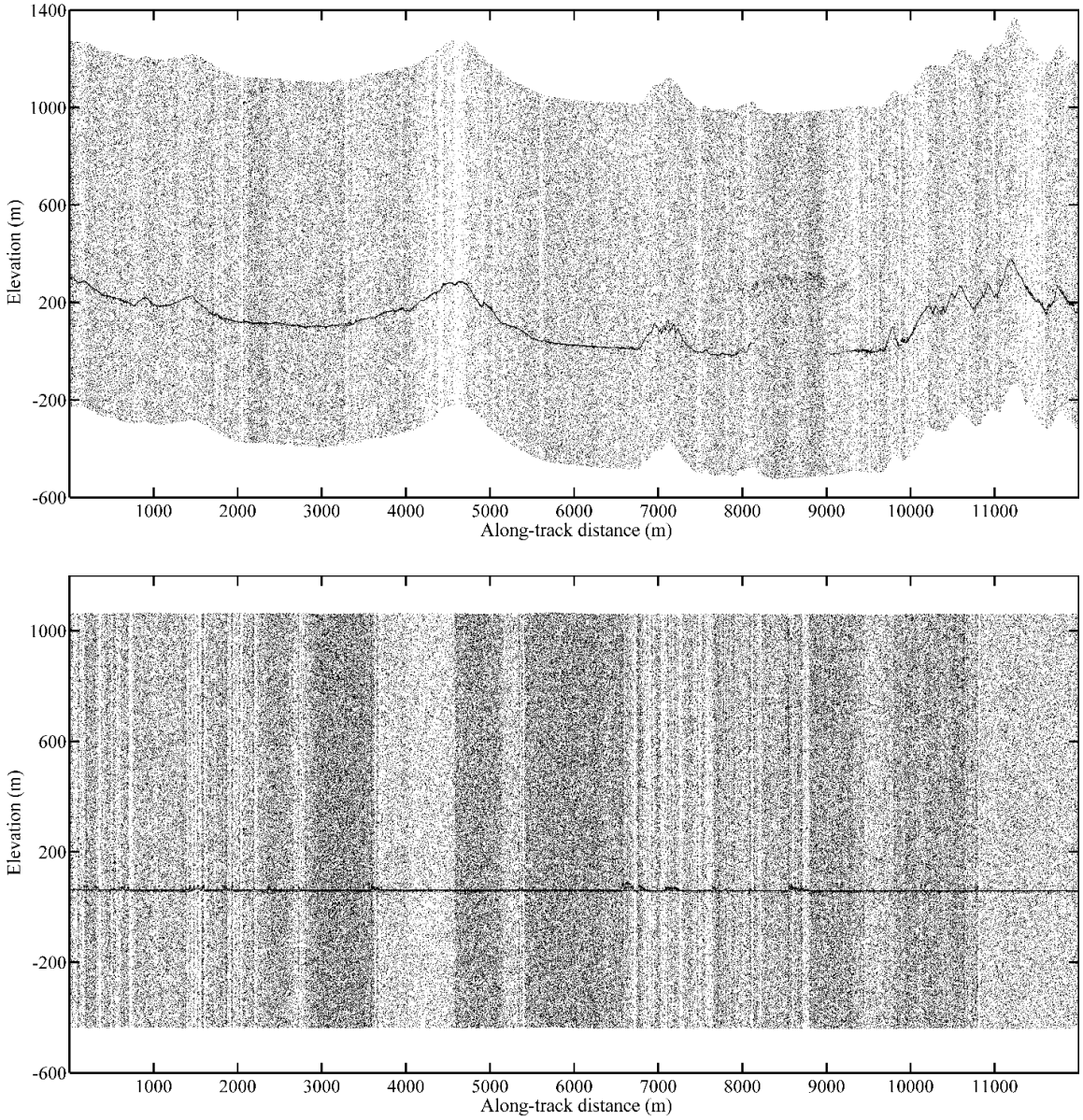

Figure 4-3 Raw MABEL CA data (top) and raw MABEL MO data (bottom). Each dataset is one minute long. Channel 16 of both datasets (the first infra-red channel) are shown.The flight height is ~20 km above the ground.

4.3 Results and discussion

The noise in the raw MABEL data set needs to be rescaled before we apply the

filter. The standard MABEL data product includes an estimate of the instantaneous noise rate which is determined by applying a window to acquire the potential noise photons using a Global Multiresolution Terrain Elevation Data digital elevation model [85]. Normally, a window composed of returns from 1000 m above ground to 500 m under the ground is defined for possible topographic photon records. In contrast to this signal window, the range window from 300 to 5300 m underground is defined as the noise window (because no signal photons would be expected there) to estimate the noise rate by counting the number of returns in this range [85]. The MABEL data provides an estimated noise rate for every 0.02 second data tile. The profile data was gridded into 0.02 second pieces to match the noise rate record. The grid width is then multiplied proportionally to the noise rate for each specific grid to create an artificial profile of consistent noise density (shown in Figure 4-4). The rescaled data is shown in Figure 4-5.

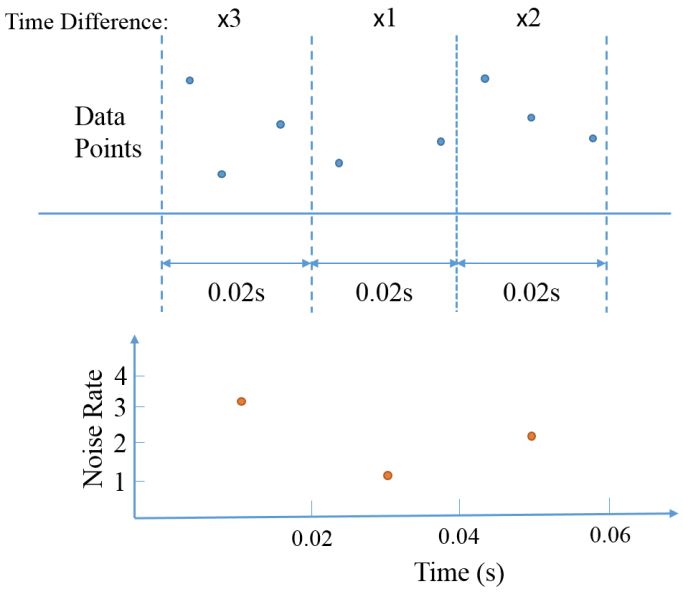

Figure 4-4 Sketch of the scaling process. The corresponding noise rate is 3, 1 and 2. So for the points in the first data bin, we multiply the time difference between two neighbor points by 3. For the points in the second bin, we multiply the time difference by 1 and by 2 for the points in the last bin.

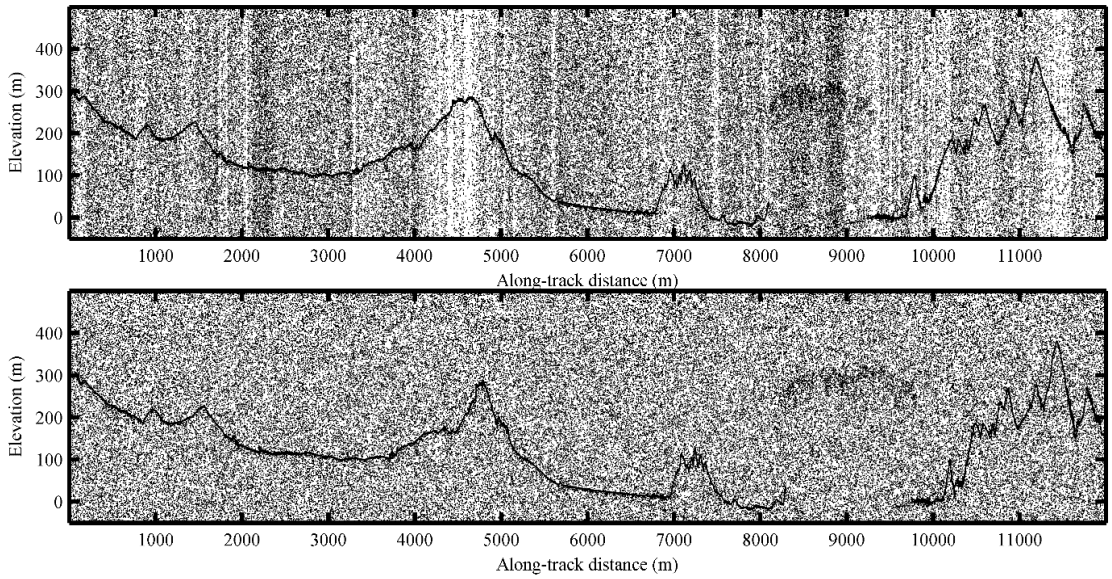

Figure 4-5 Comparison of raw MABEL CA data (top) and the noise density scaled result (bottom).

As we can see from Figure 4-5, regions with fewer noise photons (e.g., 4000–5000 m) are concentrated and more likely to be detected due to the increased signal density. In contrast, regions with a high noise rate (e.g., 8000–9000 m) are diluted, and only the returns with significantly high density will be determined as signal photons. Noise scaling benefits density–based noise filters because a relatively consistent noise density is present in the resultant pseudo-distance profiles. The distribution of signal points is also changed during rescaling. The filtering process outputs the index of signal points and returns their actual coordinates before rescaling. Thus the rescaling process does not result in an erroneous filtered profile.

The proposed algorithm was applied to the two MABEL data sets. The filtered results for the CA data set are shown in Figure 4-6. To quantitatively validate the performance of the Bayesian algorithm, we compared the CA MABEL extracted ground surface to the coincident airborne LiDAR data set. We show a scatter plot of MABEL versus airborne laser scanning (ALS) topographic elevation in Figure 4-7 (a) and (b) for

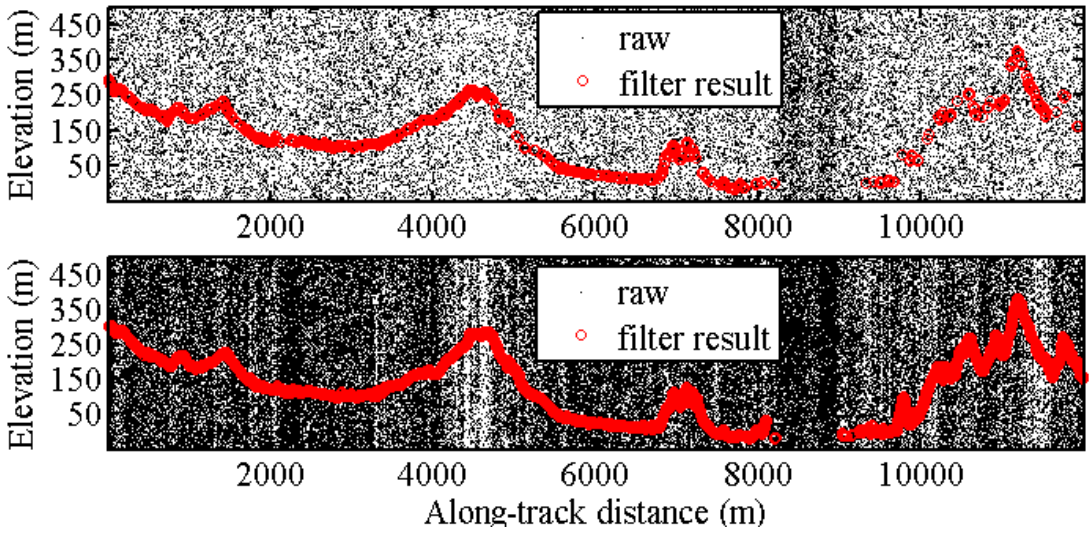

Figure 4-6 Filtered result for the CA dataset with the proposed method. Top figure shows results for channel 3 (green) and bottom figure shows result for channel 16 (infra-red).

the MABEL green and near-infrared LiDAR channels, respectively, and obtained a regression fit R^2 of 0.9897 for the green channels and 0.9989 for the near-infrared channels. In Figure 4-7 (c), we show RMSE for each of the MABEL channels individually. Channels 1–15 are green laser channels, and channels 16–23 are near-infrared channels which have consistently lower RMSE. The maximum and minimum green channel RMSE is 3.15 m for channel 4 and 5.47 m for channel 10, respectively. The maximum and minimum infra-red channel RMSE is 2.83 m for channel 17 and 4.43 m for channel 22, respectfully. The lower RMSE in infra-red channels is because the near-infrared channel has a higher return strength from vegetation and natural ground targets. As a result, we will have more signal returns, i.e., higher signal to noise ratio (SNR). This is supported by the results because we see more signal returns in Figure 4-7 (b) than in Figure 4-7 (a). Overall, given that the horizontal positioning accuracy of MABEL is estimated to be 30 m [86], and the data were collected in terrain with significant relief, this elevation agreement is quite good.

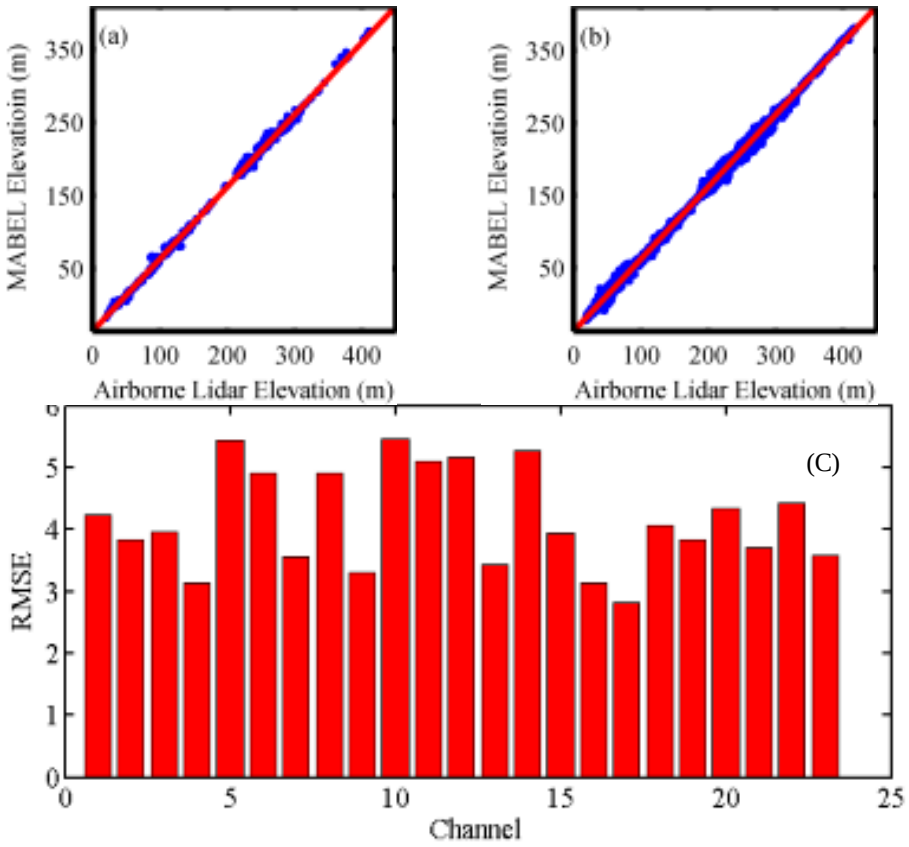

Figure 4-7 Scatter plot of airborne LiDAR elevation and MABEL green channel 3 elevation(a), near-infrared channel 16 elevation (b) using our algorithm. RMSE between airborne LiDAR and MABEL elevation in each channel are shown in (c)

As a final validation of our proposed filtering approach, we compare our algorithm with another point density method, the mDBSCAN proposed by Zhang and Kerekes [41]. The estimated topographic profiles from both methods for the CA data set are shown in Figure 4-8 and the RMSE comparison is shown in Figure 4-9. From Figure 4-9, we see that the mDBSCAN results for the green channels have a large RMSE of 25 m. This is because mDBSCAN does not consider the inconsistent noise level of the data. In Figure 4-6, we find that between 8000 and 9000 m along the profile, the noise rate is very high, which makes the signal in that area difficult to detect. mDBSCAN does not consider this higher noise rate and therefore detects many noise points as signal. However, in our method, we scaled the noise first to have a consistent noise level for the

whole data set. Then the high noise rate area does not have photon detection events incorrectly classified as terrain returns. To provide a common basis of comparison, we also applied the mDBSCAN algorithm on the adaptive noise scaled data set. The results are improved and this RMSE is shown in Figure 4-9 as the blue line. Although the adaptive noise scaling improves the mDBSCAN results, it is still outperformed by the Bayesian method; the overall mean RMSE on all the channels for the scaled mDBSCAN is 5.1 m versus 4.2 m using our method.

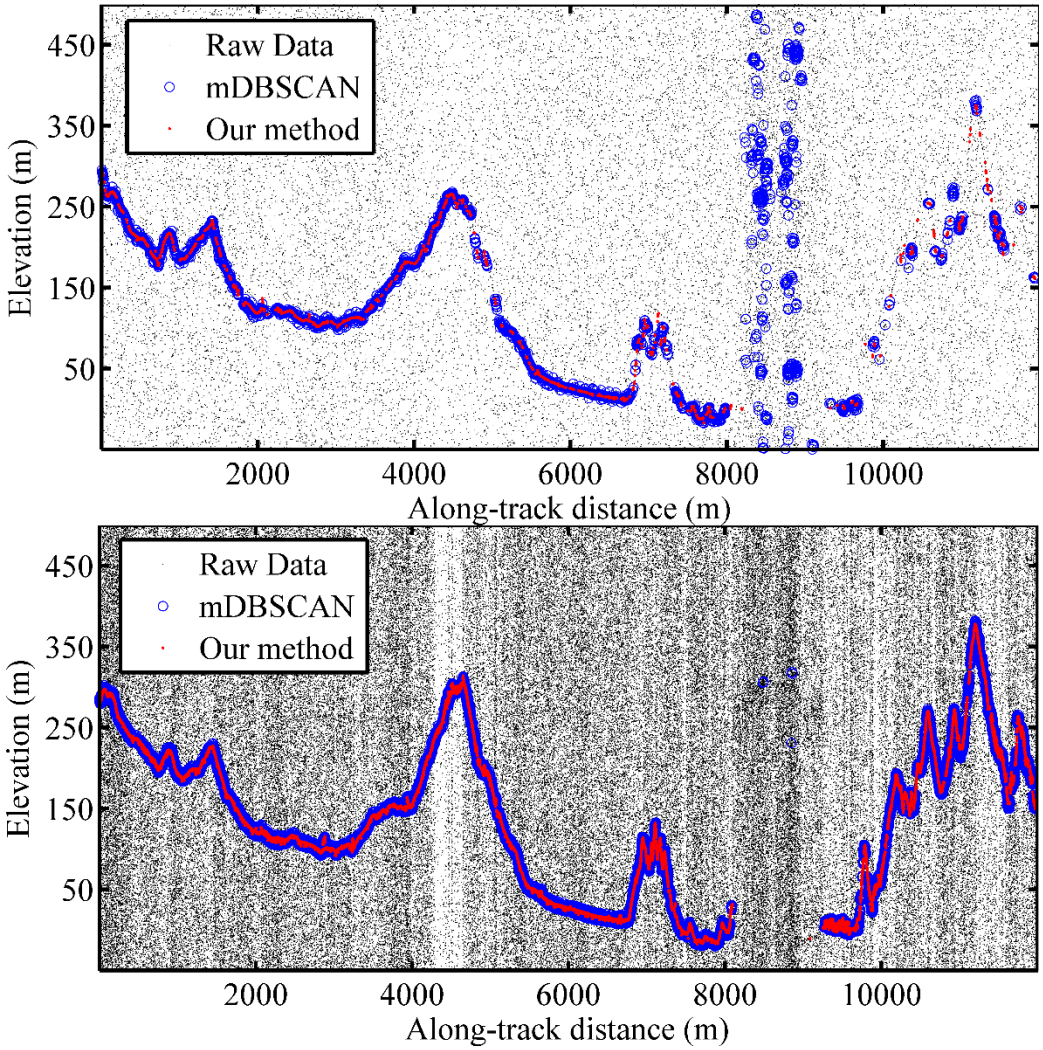

Figure 4-8 Comparision of results of mDBSCAN and the proposed method. Green channel (channel 3) result (Top) and infre-red channel (channel 16) result (Bottom).

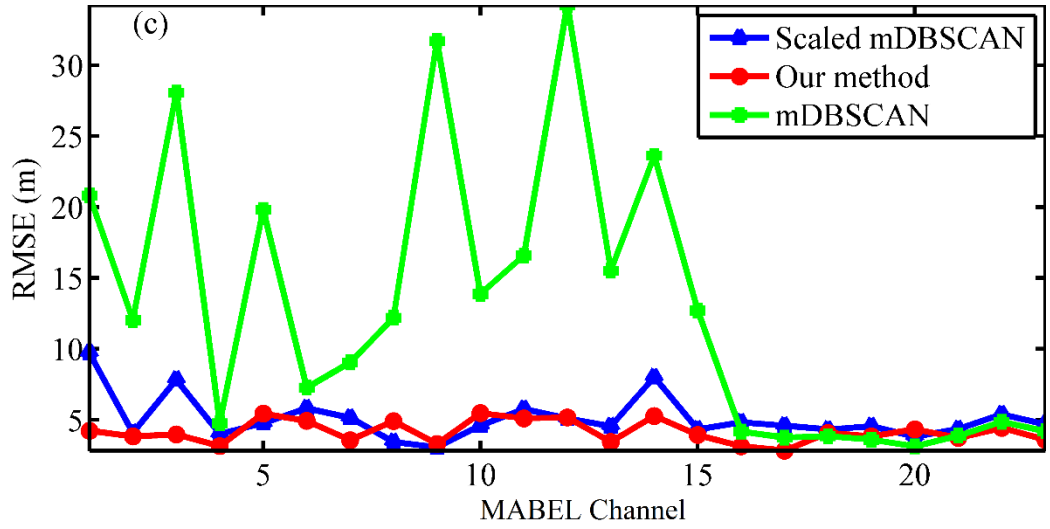

Figure 4-9 Comparision of RMSE for mDBSCAN, scaled mDBSCAN and the proposed method.

Finally, we also tested our proposed filter algorithm on the Missouri dataset and again compared with mDBSCAN. The filtered results are shown in Figure 4-10, and again demonstrate that the proposed algorithm can provide reliable results with lower rates of misclassification. The mDBSCAN method incorrectly classifies more near-ground noise than our algorithm. We compared the extracted ground surface from all MABEL channels of the Missouri dataset to the coincident airborne LiDAR dataset. We display the RMSE for each channel in Figure 4-11, and observe that the mDBSCAN results have a similar RMSE with or without the noise scaling process. The reason is that for this dataset, there is no drastic change in noise rate like the CA dataset. Our proposed algorithm improves the RMSE by about 0.5m over mDBSCAN, which is significant considering the overall RMSE is only about 2.5m.

Higher SNR of infra-red channels makes their filtering results more robust to varying noise rate. And this is why the rescaling process made little improvement for infra-red channel filtering results or sometimes made it a little worse (see Figure 4-9). For green channels, the low SNR makes them susceptible to the inhomogeneous noise rate

and the results benefit from the rescaling process, which can be seen clearly from Figure 4-9. The motivation for the MABEL system and acquisitions was to test algorithms for ICESat-2 which utilizes a green laser. Thus the rescaling process is of great importance in any density based filtering algorithm.

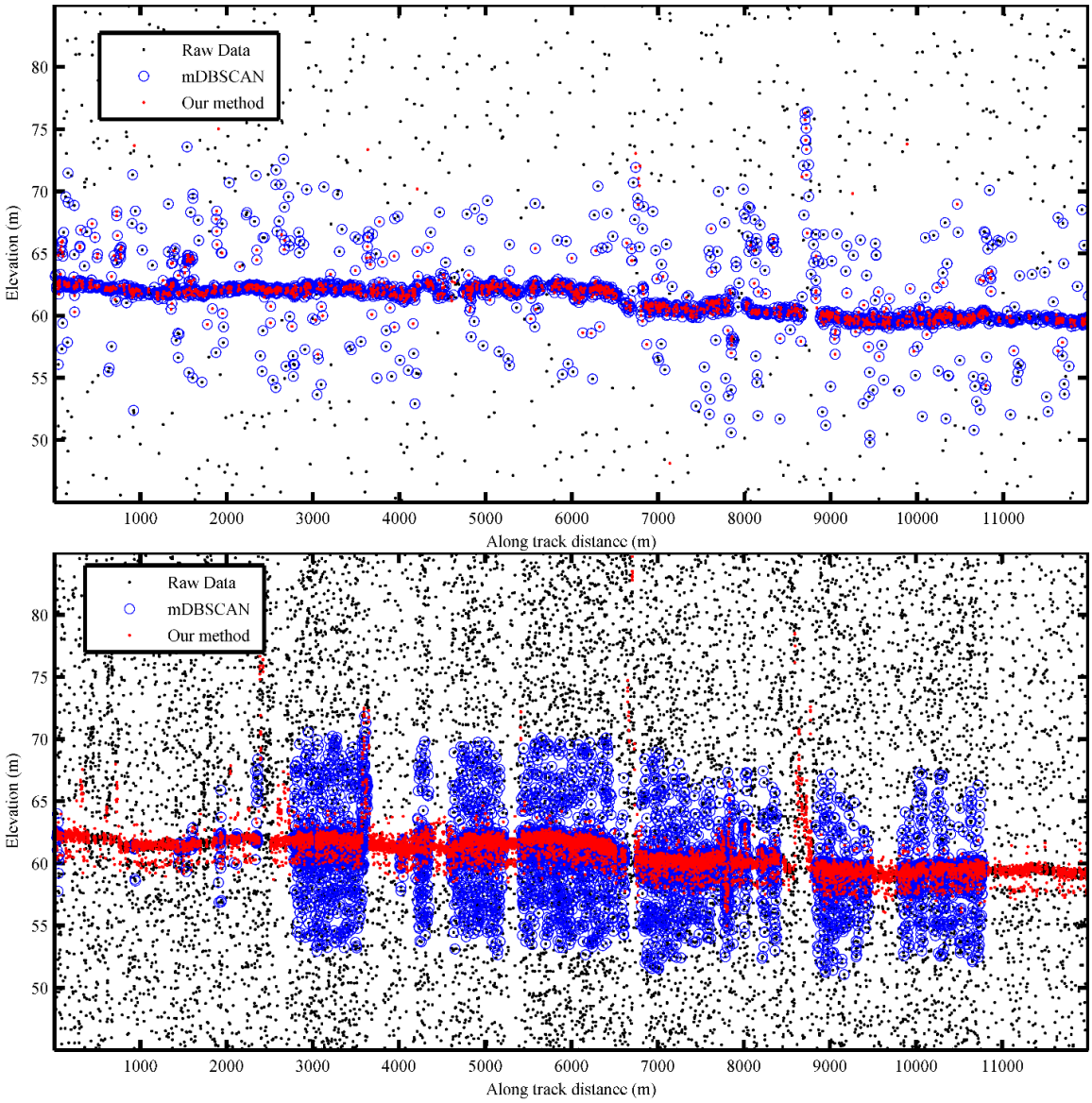

Figure 4-10 (Top) Filtering results for representative green channel using (blue) mDBSCAN and (red) the proposed algorithm on the Missouri data set. (Bottom) Filtering results for a near-infrared channel using (blue) mDBSCAN and (red) the proposed algorithm

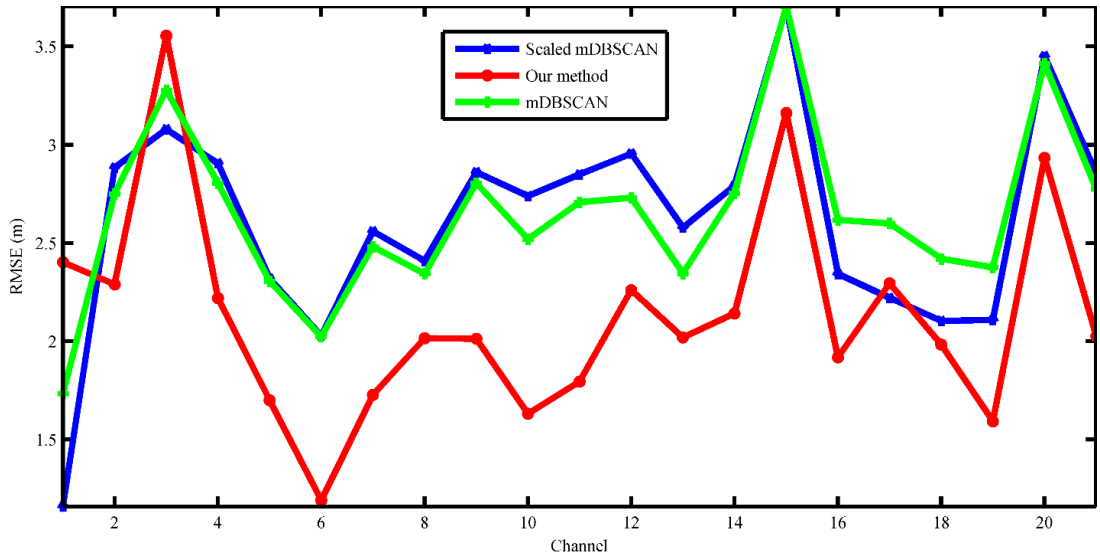

Figure 4-11 RMSE of airborne LiDAR elevation and Missouri MABEL elevation in each channel with mDBSCAN, scaled mDBSCAN and the proposed algorithm.

4.4 Conclusions

In this chapter, a novel point density based algorithm was proposed for filtering single photon counting LiDAR profiles. Instead of using a simple threshold method, the algorithm considers the probability distribution function of distances to the *k*-th nearest neighbors and then applies Bayesian decision theory to calculate the probability of a point being signal or noise. Before filtering we also adaptively scale the noise level based on the estimated noise rate provided in the MABEL data records. This proposed noise scaling significantly improves the performance on green channels when using point density based methods. Validation of the algorithm on MABEL data using high accuracy airborne laser scanning showed that the ground surface can be reliably extracted. The RMSE between the filtered CA MABEL profile and the ALS is ~6 meters for MABEL's green channels and ~4 meters for the near-infrared channels. The RMSE for comparison between the MABEL profile and ALS data for the MO test dataset is ~2 meters. We also

compared our algorithm with another point density based algorithm, the modified DBSCAN. The results showed that our algorithm was able to extract more signal points than mDBSCAN and performed better in steep areas of relief.

Chapter 5

An Adaptive Ellipsoid Searching Filter for Airborne Single Photon LiDAR

In the previous chapter, the single photon altimeter data was filtered considering only 2-D profiles in the along-track and vertical direction. In this chapter, we expand the proposed method to three dimensions to filter 3-D imaging SPL point clouds. Compared to single photon altimetry, three-dimensional imaging single photon LiDAR are able to produce point clouds for the entire illuminated area because they also contain a scanning mechanism. The scanning process makes the altimetry filtering method introduced in Chapter 4 unsuccessful for 3-D SPL data. Thus, a novel adaptive ellipsoid searching (AES) method is proposed for 3-D SPL data filtering. This chapter is a summary of the work published in [87].

5.1 Background

Research on 3-D SPL data filtering is still at an early stage. All the currently published filtering methods take advantage of the fact that SPL data noise points are sparsely and randomly distributed in space, while signal points are much more clustered [82]. The current filtering methods can be divided into two categories: histogram-based and voxel-based. Both of them work at the resolution of the data bin and thus have very high computational efficiency.

However, there are two significant limitations for the current methods. The first issue is that solar background noise is not spatially homogeneous; it varies based on

factors such as return surface spectral reflectance and the laser scanning geometry. Higher spectral reflectance surfaces reflect more solar energy, and thus, more solar noise photons are detected by the SPL detector [23]. Scanning geometry is determined by various factors, such as flying altitude, aircraft speed, topography, and so on, and can vary significantly within a data set. The resultant inhomogeneous noise density causes significant false alarms during filtering [83]. A noise scaling method was proposed in Chapter 4 for 2-D profile data by stretching the profiles horizontally, which significantly improved filtering results by making the background noise more homogenous. However, the application of this noise scaling method to a 3-D point cloud is not straightforward. The performance of current filtering methods is also limited by the spatial resolution; photons falling into one specific voxel or data bin are classified as either signal photons or noise returns, and therefore, it is hard to remove near-signal noise returns in larger data bins or voxels.

In this chapter, a novel method to filter the 3-D imaging SPL data by adaptively searching spatially neighboring returns is proposed. Querying by individual returns instead of grouping them into voxels enables us to filter the background noise photons at the highest spatial resolution of the data set. A method to compensate for the varying background noise level using a varying estimation of noise rate is also introduced in this chapter.

5.2 Algorithm

The proposed methodology includes two steps. In the first step, most of the solar noise is removed based on a novel noise density estimation model, which is a 3-D

extension of the method introduced in Chapter 4 for 2-D profiles. In the second step, an adaptive ellipsoid is used to examine each remaining point. Instead of using a fixed size, local principle component analysis (PCA) [88] is used to adaptively change the size and orientation of the ellipsoid to account for local point cloud geometry.

5.2.1 Noise density estimation model

In this section, we introduce a new model to estimate noise density at the location of each point to allow compensation for inhomogeneous noise density. First, the individual line noise density for each outgoing beamlet, which is only related to reflectance, is estimated. We generate an elevation histogram with 1-m resolution in the z -axis for all points. The peak of the histogram represents the approximate location of the signal return. A buffer area is determined ± 50 m around the peak location. All of the signal points are assumed to be located in the buffer area and the rest of the data should contain only noise points; we will refer to this as the noise region. In the noise region, we count the number of points N for every 60 outgoing laser shots, which corresponds to approximately 0.001 s of acquisition. We assume that overall the noise level of an area scanned over such a short interval should be similar. Then, the line noise point density of all the beamlets over this interval is calculated as

$$\rho_l = N/(6000R), \tag{5.1}$$

where, N is the total number of points in the interval, R is the range of the laser and 6000 is the product of the number of laser shots (60) and the number of beamlets in each laser shot (100).

Next, the influence of scanning geometry is estimated. First, we consider the point on the top of each beamlet vector. All these points will approximately form a plane H, because data from all the beamlets are truncated with the same range gate. For each point, we define a sphere with a search radius r and count the number of beamlet vectors passing through the sphere and the length of the vector inside the sphere. This concept is shown in Figure 5-1 where O is the examined point, v is a beamlet vector passing through the sphere, q is the intersection point of beamlet vector v and the plane P and F is the location of the laser scanner. The length of the portion of the vector inside the sphere d is given as

$$d = 2\sqrt{r^2 - \left(\left|\overrightarrow{OF} \times \overrightarrow{OQ}\right| \Big/ \left|\overrightarrow{FQ}\right|\right)^2}. \tag{5.2}$$

Then the estimated noise density of one beamlet, ρ_E , is calculated as follows:

$$\begin{aligned} &\rho_E = \gamma \sum_{i=1}^{n} \rho_l^i d_i \Big/ \left(\frac{4}{3}\pi r^3\right) and \\ &\gamma = 100 n_u / n, \end{aligned} \tag{5.3}$$

where γ is a correction coefficient, n_u is the number of laser shots in the sphere, and n is the total number of beamlet vectors. The correction coefficient is the ratio of the number of laser shots fired to the number of beamlets in the sphere. There might be no return recorded for a single beamlet, and therefore, the correction coefficient is needed to scale the number of noise points. Typically, the correction coefficient is ~2, but can be as large as 10 in some areas.

The estimated noise density is assigned to all the points on the beamlet. It should be noted that this methodology allows the density of noise points for each beamlet to be different. The points with higher elevation will have a higher density because of the

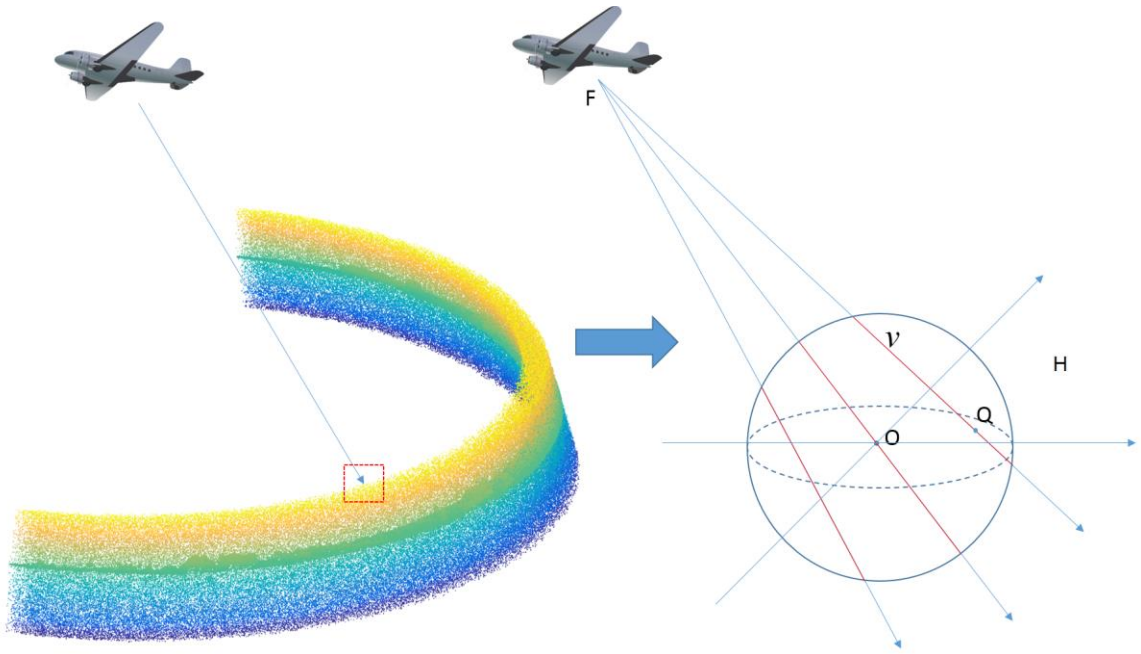

Figure 5-1 Overview of the spherical model. (Left) Data set and one beamlet vector. (Right) Details on the computations for each vector. In this example, three vectors intersect the sphere and the red portions are inside the sphere.

influence of scanning geometry. We conservatively estimate the point density from the top point within each beamlet.

After estimating the noise density for each point, an initial filtering is applied, which is similar to the application of a voxel-based method. We first count the number of neighboring points for each interrogated point in a sphere. However instead of using this number as a direct threshold, we use the quotient of the number of neighbors and the estimated noise density. Then, we estimate the number of noise points N_{tot} using the same method described in Chapter 4. The N_{tot} points with the smallest quotient are labeled as noise points. After this, most solar noise has been removed, leaving only noise points located near the signal returns. In the next section, an adaptive ellipsoid searching method will be introduced to remove these near-signal noise points.

5.2.2 Adaptive ellipsoid searching method

In this section, a morphing ellipsoid that adapts to the local scene geometry is utilized to filter near-signal noise. Near-signal noise returns have more neighbors within a voxel or data bin than other noise points, which make them more difficult to remove using point density as the only criteria. To solve this problem, we consider the geometric distribution of the signal points using a local PCA estimation. After the first step of filtering (Section 5.2.1), we examine each point in the remaining point cloud. A selection of 25 nearest neighbors to a query point is used to form a local subset, upon which PCA is applied. The number of neighbors selected is empirically determined based on the point density of the data. The result of the PCA is a 3×3 matrix P of three eigenvectors in column, and three eigenvalues e_1, e_2 and e_3. The adaptive search ellipsoid is defined using these values and the following equations:

$$\begin{aligned} a &= re_1 \Big/ \sqrt[3]{E}, \\ b &= re_2 \Big/ \sqrt[3]{E}, \\ c &= re_3 \Big/ \sqrt[3]{E} \ \ and \\ E &= e_1 e_2 e_3, \end{aligned} \tag{5.4}$$

where, a, b and c are the length of three axis of the ellipsoid and r is the radius used in the first filtering step. The ellipsoid has the same volume as the initial sphere, and therefore with the same point density the number of points in the ellipsoid should be equal. The center of the ellipsoid is at the query point. To simplify the calculations, instead of rotating the ellipsoid, we rotate the neighborhood points using the following equation

$$\begin{bmatrix} x_i^r \\ y_i^r \\ z_i^r \end{bmatrix} = P^{-1} \begin{bmatrix} x_i \\ y_i \\ z_i \end{bmatrix}, \tag{5.5}$$

where, $[x_i, y_i, z_i]$ is the coordinate of the i th neighbor point. We can then determine which neighbor points are still in the ellipsoid by substituting the rotated coordinates into the equation of the ellipsoid using

$$flag = \frac{x_i^{r2}}{a^2} + \frac{y_i^{r2}}{b^2} + \frac{z_i^{r2}}{c^2}. \tag{5.6}$$

If flag is less than one, the point is inside the ellipsoid. Finally, we count the number of neighbors of the query point in a sphere, n_s and the number of neighbors in an ellipsoid n_e is also obtained. We then consider the change of these two numbers and use the ratio, n_e / n_s , as the metric to label noise; if the ratio is less than a threshold, the point will be removed. Figure 5-2 shows the change of the search voxel from a sphere to an ellipsoid. The star is the interrogated point. The circles are its 25 nearest neighbors. The circles are evenly random distributed on a 2 x 2 plane with an RMSE of 0.2 m. The star is 0.5 m away from the plane. In the top figure, a sphere with the radius of 1.5 m is used and all the neighbor points are inside the sphere. In the bottom figure, an ellipsoid generated with local PCA is considered and only 5 neighbors are inside the ellipsoid. Points outside the ellipsoid are colored blue and points inside are colored red. Here, the change ratio (threshold) is empirically determined as 20%, which is used in this work. Selection of the threshold is empirical and 20% was effective for the experimental data. This parameter can obviously be tuned to better fit the point cloud based on the instrument specifications and collection parameters of the data set.

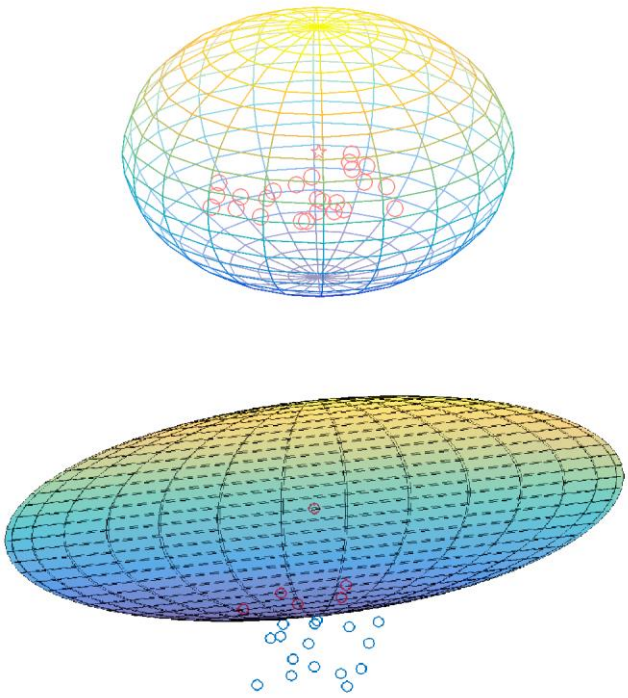

Figure 5-2 Overview of the search ellipsoid. The bottom figure is scaled to demonstrate detail more clearly.

5.3 Experimental data set

The SPL dataset analyzed was collected by the HRQLS system developed by Sigma Space Corporation. As introduced in Chapter 2, HRQLS is a moderate altitude SPL system that employs multiple laser beamlets. HRQLS is a circularly scanning system and a diffractive optical element breaks a green laser beam (532 nm) into a 10×10 array of spots at the target. Returns from each output beamlet are imaged onto an independent channel of a high resolution multi-stop timer [28], [76]. The dataset was collected on August 3rd, 2016 in Easton, MD USA. HRQLS was operated at ~3.5 km above ground level (AGL) and produced a swath of ~2 km. The imaged point density is ~12 points/m^2.

Reference data was collected by a conventional linear-mode LiDAR on June 14th 2016 with a Leica ALS 80 sensor operated at 1.3 km AGL. The nominal point density is ~25 points / m^2. The time gap between the experimental SPL data and the reference

linear-mode data is ~1.5 months and is short enough that few differences in the imaged scene would be expected.

5.4 Results and discussion

Figure 5-3 shows the results of the spherical noise estimation. (A) is an overview of the spherical noise estimation model where the points are colored by estimated noise density (points/m3). (B) shows a filtered point cloud using noise estimates from the spherical model. The points are colored by elevation (meters). (C) demonstrates the result of a voxel-based filtering method and again the points are colored by elevation. We can clearly see a yellow strip with high noise density [shown with an arrow in Figure 5-3 (A)]. High density areas of noise have similar spatial characteristics as points from weak reflective targets, such as vegetation. Using a single fixed threshold without considering the varying noise rate is not sufficient to accurately filter the noise. Figure 5-3 (B) shows the filtered result using only the noise density estimation step of the proposed method, and we can clearly see that there are no remaining noise points in the region identified in Figure 5-3 (A) as having high noise rates. While with the voxel-based results, given in Figure 5-3 (C), there are some residual noise points left because of the localized variations in noise density. The final filtered result of the data with both proposed steps is shown in Figure 5-4.

Next, we compared the filtered result from our proposed method to both a voxel-based method and reference linear-mode data. The voxel-based method used a cube size of 3×3×0.3 m (Length×Width×Height) as suggested in [89] and the threshold for noise removal was the mean point density. Further details on the voxel-based method can be

found in [89]. We selected three types of terrain: rooftops, bare ground, and the top of the vegetation canopy to compare the performance of the proposed filtering method with the voxel-based approach. For each type of terrain, five regions were selected for comparison. The area of each region is ~200 m^2. The root mean square error (RMSE) of the filtered results is given in Table 5-1.

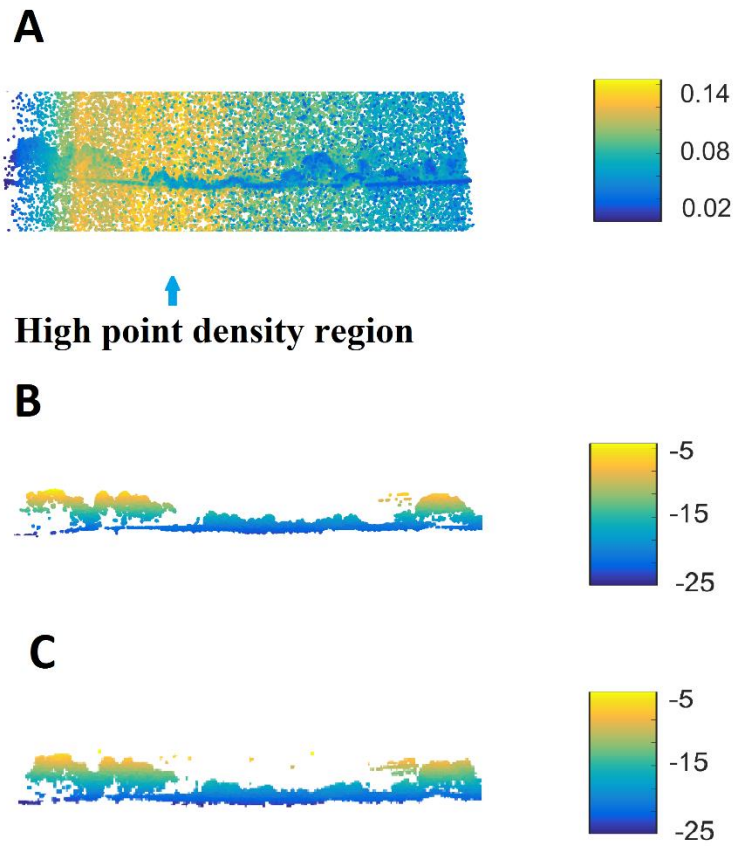

Figure 5-3 Comparision of results from the proposed method and voxel-based method. The horizontal extent of the data is about 150 m.

To determine a noise level for signal returns for the HRQLS data sets, and to get an idea of the difference in the number of noise points removed by the two filtering methods, we manually classified eight rooftop regions as a benchmark for comparison. The eight roofs were selected from strong reflective surfaces, where the roof definition was very evident in the SPL data. The results are shown in Table 5-2.

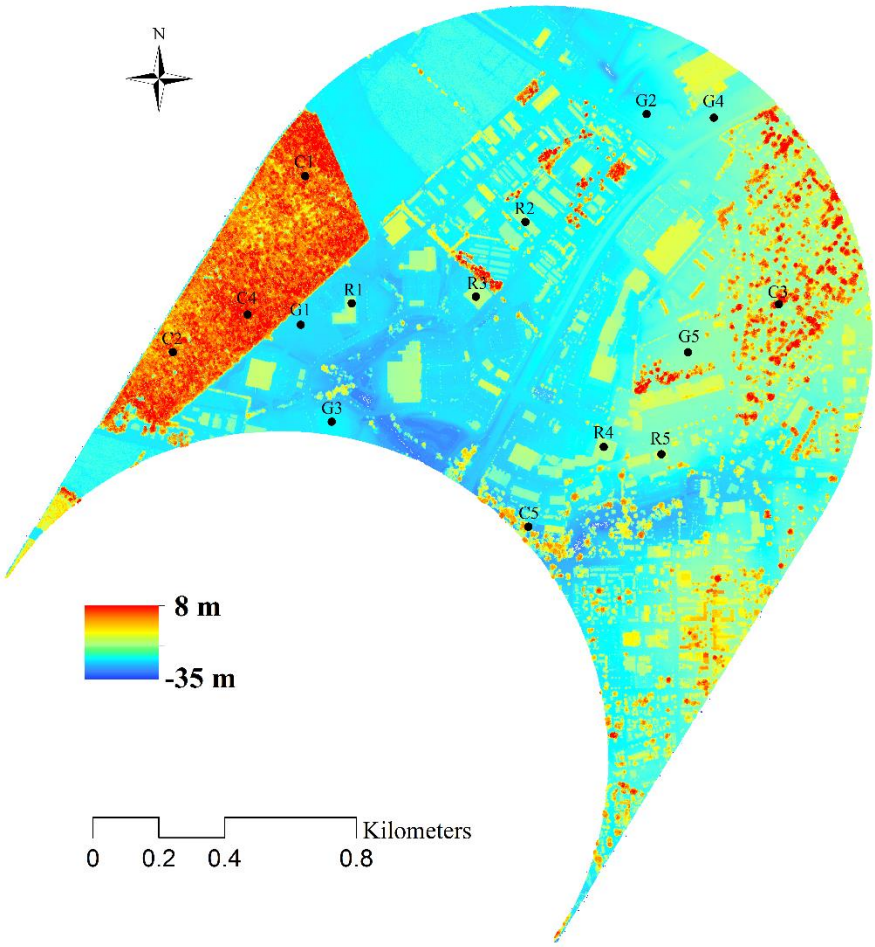

Figure 5-4 Filtered point cloud of study area. The points are colored by ellipsoidal elevation. Fifteen test areas are labeled: R1–R5 are rooftop targets, G1–G5 are bare ground areas, and C1–C5 are vegetation canopy.

Table 5-1 Statistical comparison between the proposed method and the voxel-based method. Root mean square error (RMSE) in meters between the filtered results and the reference linear mode LiDAR data is shown.

	Type	Region 1	Region 2	Region 3	Region 4	Region 5	Max	Min	Mean
Roof	AES	0.10	0.10	0.09	0.09	0.08	0.10	0.08	0.09
	Voxel	0.14	0.11	0.11	0.10	0.10	0.14	0.10	0.11
Ground	AES	0.16	0.14	0.10	0.08	0.10	0.16	0.08	0.12
	Voxel	0.19	0.16	0.12	0.10	0.12	0.19	0.10	0.14
Canopy	AES	1.85	1.95	2.79	1.98	1.79	2.79	1.79	2.07
	Voxel	2.08	2.21	3.24	3.12	2.11	3.24	2.08	2.55

Table 5-2 Number of noise points removed by the proposed method and voxel-based method compared to manual classification along with RMSE of the plane fit from the manually filtered point cloud. Roof 1, 6, 7 and 8 are tilted rooftops and all others are flat.

	Total	Proposed	Percentage	Voxel	Percentage	RMSE
Roof 1	89	61	69%	30	34%	0.10
Roof 2	333	296	89%	168	50%	0.09
Roof 3	335	268	80%	127	38%	0.09
Roof 4	508	415	82%	192	38%	0.08
Roof 5	120	110	92%	59	49%	0.08
Roof 6	183	137	75%	85	46%	0.07
Roof 7	108	75	69%	29	27%	0.07
Roof 8	119	105	88%	63	53%	0.08

From the table, we can see that the proposed method filtered about twice as many near-signal points as the voxel-based method did. For hard planar surfaces (rooftops), the proposed method RMSE compares very closely with that of the manually filtered point cloud. For a qualitative analysis, we selected two representative profiles to show the difference between the two filtered results. Figure 5-5 (A) and (B) shows vertical profiles of rooftops: one tilted roof and one horizontal roof. We can see that the proposed method profiles are very clean, while the voxel-based result is noticeably noisier. The voxel-based filter works better for the horizontal roof; this is because all of the voxels are of the same size and orientation (usually horizontal). For the tilted roof, a voxel will cover both roof and noise and misclassify the noise points as part of the signal. For the proposed method, the searching ellipsoid changes its size and orientation adaptively based on local geometry so that the signal points are kept and more noise close to the surface is removed. A majority of the remaining noise points underneath the rooftop are caused by the detector after-pulsing effect [75], which results in more clustered noise that cannot be

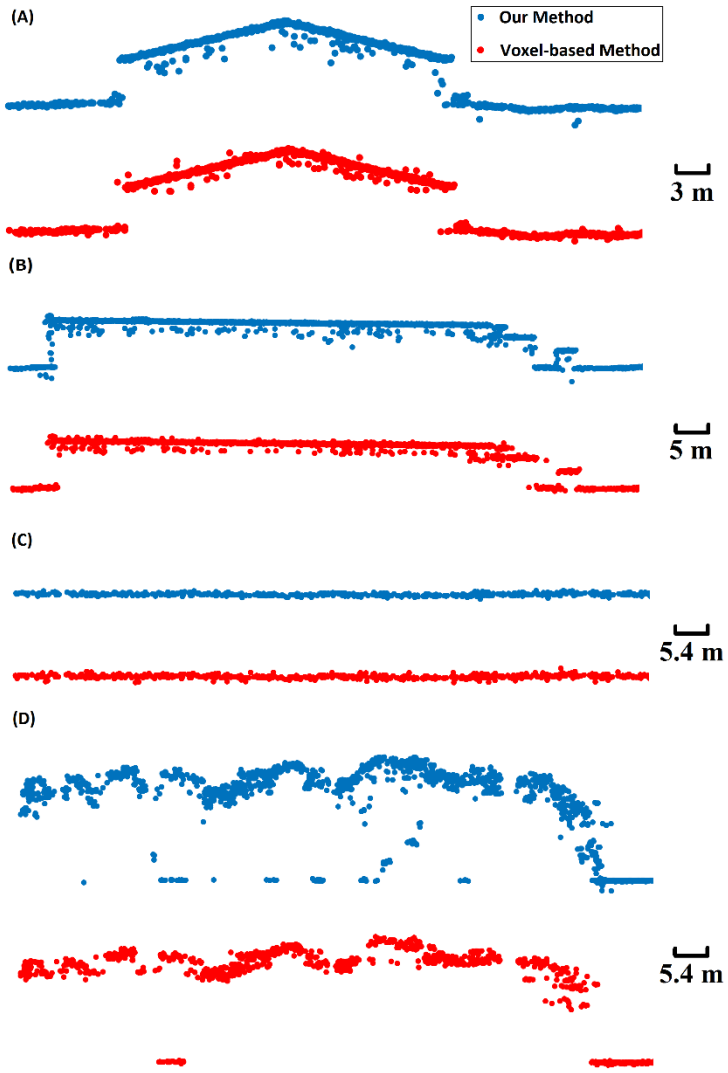

Figure 5-5 Comparison of results from the proposed method and voxel-based method. The width of all the vertical sections is 2 m. (A) tilted rooftop, (B) flat rooftop, (C) bare ground, (D) vegetation canopy.

easily removed with a density-based method. These correlated noise points have different characteristics from solar noise and their removal will be discussed in Chapter 7. The RMSE of the tilted rooftop is 0.11 m for the proposed method and 0.16 m for the voxel-based method. For the flat rooftop, the RMSE is 0.12 versus 0.14 m for proposed and voxel-based, respectively. The RMSE difference of the two results is not very significant because of the small number of close-to-surface noise points present for the

rooftops. However, even though the RMSE is close, Table 5-2 shows that on average the proposed method removes significantly more of the near-signal noise points.

Figure 5-5 (C) shows a vertical profile of bare ground. Result for the ground profile is similar to that of the flat roof top, except that the after-pulsing effect is not as evident because the ground surface is not a bright reflector. We can see some noise points remaining in the voxel-based result. The RMSE of AES method result is 0.12 m versus 0.14 m for the voxel based method; the voxel-based method has difficulty in areas where the terrain is sloped; similar to the situation for tilted rooftops.

Finally, we compared results in a vegetation canopy region as shown in Figure 5-5 (D). For this region we compared top of canopy estimates. The RMSE of our proposed method is 2.07 m while the voxel-based RMSE is 2.55 m. The RMSE is higher for both methods in the canopy regions; when compared to solid surfaces such as rooftops and ground, the canopy shape is significantly more complex. Because there is no consistent canopy shape, even the use of an adaptively based ellipsoid cannot adequately model the rapidly changing surface model. As, a result, while the AES method improves the results over the voxel-based method it still struggles to accurately separate signal from noise in the tree canopy.

As a final note, increased processing time is a drawback of the proposed method. For the filtering of one million points, the voxel-based method runs in 45 seconds versus 269 seconds for the proposed method. All the algorithms were run with Matlab 2016a on the same computer (Intel E5-2603, 16 GB RAM).

5.5 Conclusion

In this chapter, a novel AES method was proposed and tested for filtering SPL data. The AES method has two steps: in the first step, a spherical model for noise density estimation is established to balance the influence of inhomogeneous noise levels throughout the point cloud. Noise points, even in high noise rate regions can be removed. In the second step, an ellipsoid is used to filter near-signal noise points. Local PCA is applied to adapt the size and orientation of the ellipsoid to the local signal points. We applied the proposed method on an experimental SPL data set and compared with a published voxel-based filtering method. Artificial targets (rooftops), bare ground, and vegetation canopy were selected to compare the performance of the two methods. The results show that the AES method has a lower RMSE in all these regions and especially outperformed the voxel-based method in areas where the reflective surfaces (targets) were sloped.

Chapter 6

An Improved Adaptive Ellipsoid Searching Method for Combined Single Photon LiDAR data

In Chapter 5, an AES filtering method to effectively remove solar/dark noise in SPL data was introduced. In this chapter, an improved AES method is proposed to retain linear features in SPL data while still effectively removing noise returns. The improved method works on the combined SPL data sets (i.e. overlapping flight lines) to further utilize spatial correlation of signal points. Powerlines, an important linear feature in SPL data, are used to check the performance of the improved method. This chapter is a summary of the work in [90].

6.1 Background

Mapping and monitoring powerlines is of importance to power companies [91]. Airborne linear mode Light Detection and Ranging (LiDAR) has been proven to be an efficient and accurate tool to monitor powerlines. A great number of methods have been proposed to classify and reconstruct powerlines from LiDAR point clouds, for example: [92]–[97].

SPL systems are able to detect weaker laser returns than its predecessor, linear mode airborne LiDAR (LMAL). This high quantum sensitivity affords SPL a tremendous efficiency advantage over LMAL systems because they are able to collect data with a wider swath and from a higher altitude [51]. Therefore, SPL has potential to be a more efficient tool for powerline monitoring.

The AES method introduced in the last chapter is able to remove most solar/dark noise effectively. However, it does not fully utilize the spatial correlation between overlapping observations from different epochs of time because it filters SPL data from individual flightlines and epochs separately, without considering time or spatial overlap. During data collection, a majority of imaged areas are scanned repeatedly at multiple epochs and with differing view geometries. In these overlap areas the spatial correlation of noise returns is not enhanced due to their random distribution within the range gate. However, for signal photons, the returns locations from different observational epochs are correlated. The simultaneous analysis of all observations from a particular area results in more clustered signal points, which will enable improved filtering results. These clustered observations are more advantageous when considering weak signal returns from objects such as power lines than for larger targets with strong reflectance (e.g., rooftops).

The filtering process required for a combined point cloud consisting of multiple time separated observations of an area differs from that used to examine raw SPL data on an epoch by epoch basis. For instantaneous epoch filtering the basic processing flow for the histogram-, voxel-based and AES methods is similar: extract the characteristics of the noise returns (e.g., distribution, point density etc.) in regions without signal points, and then use these characteristics to remove them in the entire data set according to expected instantaneous properties of the noise. However, for combined multi-look SPL data, the statistics and characteristics of the noise returns are not static because we are combining different observations from different points in time, and the noise density is known to vary substantially with both time and viewing geometry. Therefore, a new workflow for the combined SPL data filtering is required.

In this chapter we propose an improved AES method, called the voxel-spherical adaptive ellipsoid searching (VSAES) method, in which a voxel spherical (VS) model is adopted to estimate the point density of the combined point cloud, and an improved adaptive ellipsoid searching (AES) method is applied to remove the noise points. The new method is based on a probabilistic model instead of the direct ratio rule used in the original AES method presented in Chapter 5.

6.2 Algorithm

The filtering workflow for the combined point cloud is comprised of three steps: (A) tiling the raw data into data blocks, (B) estimating point density using the VS model and, (C) removing noise returns with an improved AES method. Details of each step are given in the following sub-sections.

6.2.1 Data tiling

The study area is rasterized with a square horizontal grid resolution of 100 m. A new data file is generated for each grid cell, and then all points within the cell are stored in the corresponding file based on their horizontal locations. In addition to three dimensional coordinates, the GPS time, channel number and line point density are also stored for each point. Line point density is calculated from the raw single range observation dataset by counting the average number of noise points per meter for each laser beamlet in the same way as introduced in Chapter 5. Figure 6-1 shows a representative data block and line noise density for each data point in the block.

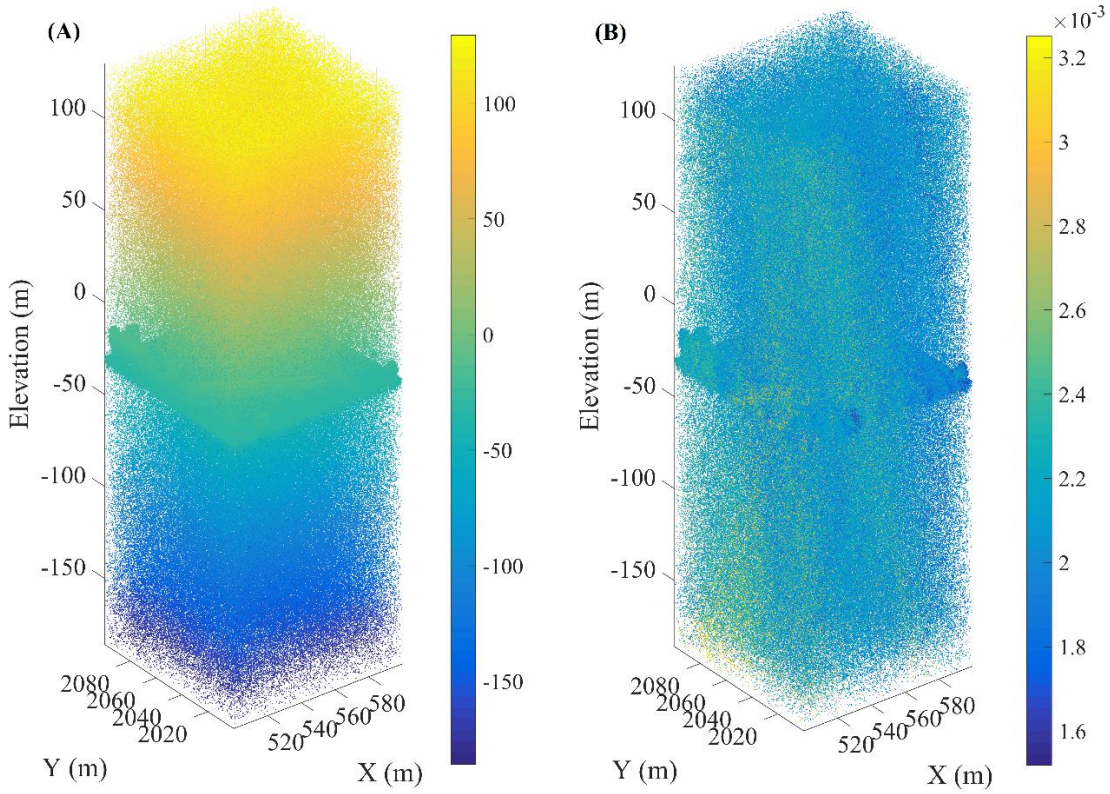

Figure 6-1 An overview of a data block after tiling. (A) is colored by elevation and the (B) is colored by estimated line point density

6.2.2 VS model

As previously explained, the noise density varies both horizontally and along the laser line of sight. Therefore, the noise density for the whole data set needs to be estimated instead of computing a single noise metric based on the top part or the bottom part of the data block, which are usually regarded as noise region and used to compute unified noise metrics [87]. Herein, we first group points into voxels, estimate the voxel noise density and assign this value to all the points inside the voxel. It is safe to assume that the noise density does not change much in a small voxel, for example 10 × 10 × 10 m, which is the voxel size used in this paper. A sphere located at the center of the voxel is then defined with the same volume as the voxel. Next, the expected number of noise

points in the sphere is estimated. For every point in the data block, the corresponding aircraft location can be interpolated using the post-processed GNSS/INS aircraft trajectory. The vector connecting the data point and the aircraft describes the direction of the outgoing laser beamlet. By calculating the distance between the line and the center of the sphere we can determine if the laser beamlet intersects the sphere. Given the spatial relationship between the query data point Q, the corresponding aircraft location F and the sphere center O as shown in Figure 6-2, the distance between the laser beamlet and the sphere center is calculated as

$$d = \left|\overrightarrow{OF} \times \overrightarrow{OQ}\right| / \left|\overrightarrow{FQ}\right|. \tag{6.1}$$

The laser beamlets at a distance to the center of the sphere shorter than the radius intersect the sphere. The part of a laser beamlet inside the sphere is labeled red in Figure 6-2 and its length l can be easily calculated using the Pythagorean Theorem. By applying this process to each data point in the block, we obtain all the laser beamlets intersecting the sphere and the corresponding length of the beamlet within the sphere. The estimated noise point density inside the sphere is then given as follows:

$$\begin{aligned} &\rho_E = \sum_{i=1}^{n} \rho_l^i l_i \gamma \Big/ \left(\frac{4}{3}\pi r^3\right) and \\ &\gamma = 100 n_u / n, \end{aligned} \tag{6.2}$$

where, ρ_l^i is the line point density of the *i*-th laser beamlet which is calculated in step A, l_i is the length of the segment of the *i*-th beamlet inside the sphere, r is the sphere radius and γ is a correction coefficient which is the ratio of the number of laser shots to the number of beamlets in the sphere. The correction coefficient compensates for channels

that do not have a return recorded [87]. Figure 6-2 gives an overview of the whole process for the VS model.

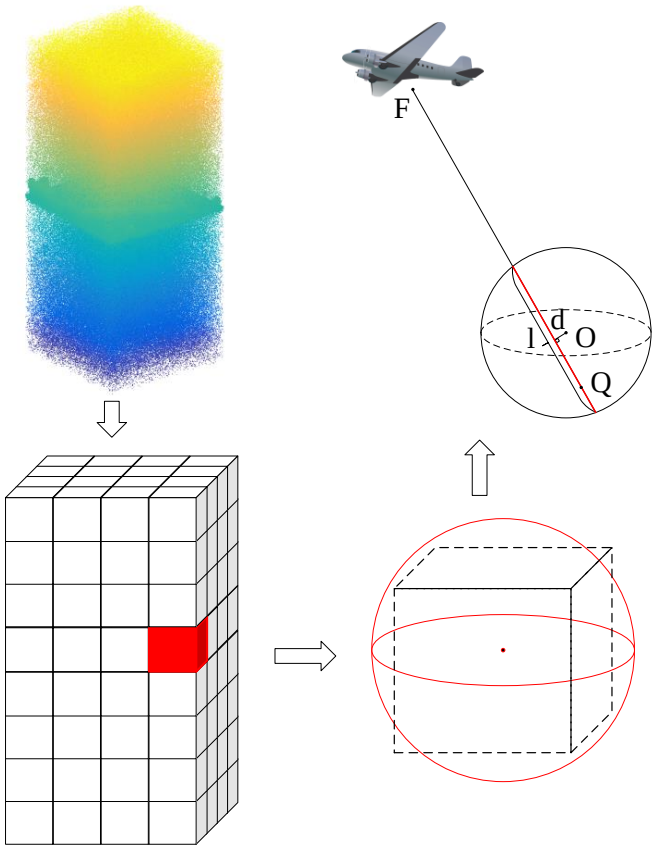

Figure 6-2 The workflow for the VS model. The data block is first voxelized. Then for each point, a sphere with the same volume as the voxel is defined at the center of the voxel. Finally, the expected number of points is calculated.

6.2.3 AES

The AES application is similar to what was introduced in Chapter 5: 25 neighbors are selected to compute a PCA and then the ellipsoid based on the PCA is rotated and the number of points in the rotated ellipsoid are counted. In the last chapter, an empirically determined threshold is then used to classify the query point. Here, we expand the AES method with a more rigorous testing procedure by establishing a hypothesis test; H0: the query point is a noise return and H1: the query point is a signal point.

For a given query point and a region with any shape around it, the number of neighbor points inside the region conforms to a Poisson distribution; the proof is as follows. Consider a 3-D space with randomly distributed points. For any point, the probability of the number of its neighbor points inside the region is calculated as

$$P = \binom{k}{N-1}\left(\frac{v}{V_s}\right)^k \left(1-\frac{v}{Vs}\right)^{N-k-1}, \tag{6.3}$$

where, k is the number of neighbors, v is the volume of the region, V_s is the volume of the whole space and N is the number of all points in the space. When V_s and N are very large, the equation can be approximated as

$$P = \frac{N^k}{k!}\left(\frac{v}{V_s}\right)^k e^{-\frac{N_v}{V_s}}. \tag{6.4}$$

We can then define a point density $\rho = N/V_s$, and rewrite the equation as

$$P = \frac{1}{k!}(\rho v)^k e^{-\rho v}. \tag{6.5}$$

The density is obtained from the VS model by dividing the expected number of points with the volume of the voxel. If the cumulative probability from zero to k is less than 95%, then the null hypothesis H0 is true and the point is a noise return, otherwise the point is a signal photon.

6.3 Experimental data set

The experimental dataset was collected using the SPL100 system. Two datasets were used to examine performance of the proposed method. The first dataset was collected on November 10th, 2016 at Easton, MA and contains three overlapping flightlines. Data collection was from ~3.5 km above ground level (AGL) with a cone

angle of 9 degrees and a scan frequency of 60 kHz. The point density is ~18 points/m^2 for a single flightline pass and the dataset was truncated with a range gate of 300 m around the expected signal return location. The other experimental dataset was collected on February 23rd, 2017 at Lufkin, TX and also contains three overlapping flightlines. The aircraft flew ~2 km AGL with a cone angle of 12 degrees and scan frequency of 50 kHz. The point density is ~20 points/m^2 for a single flightline pass and the dataset was truncated with a range gate of 85 m.

6.4 Results

The VS model was first applied to each data block. Figure 6-3 displays the results of a representative VS model where we can see that the noise density is uneven throughout the whole data block. This demonstrates the importance of considering the scanning geometry when estimating noise level.

The filtered result with both VS and AES applied is shown in Figure 6-4. For comparison the filtered result for the same area using a histogram method and the AES method are also shown. The histogram method proposed by Degnan was used; more details on this method can be found in [23], [51].

The red linear feature crossing in Figure 6-4 from the top left to bottom right is a transmission line. We note significant differences in appearance of this transmission line when comparing the three filtered results. We have also manually classified the transmission line returns for comparison with the filtered results. Figure 6-5 shows the vertical profiles of the filtered and manually classified transmission line and Table 6-1 gives a comparison of filtered and manually classified datasets. We define a 7x7 m

(Height × width) examination region around the transmission line and count the number of laser returns classified as signal from the transmission line within it. We then compare these points with the number of manually classified transmission points. The detection rate is calculated by dividing the number of correctly identified points with the number of manually classified signal points in the examination region. The false alarm rate is calculated by dividing the number of misclassified points with the total number of extracted points in the examination region.

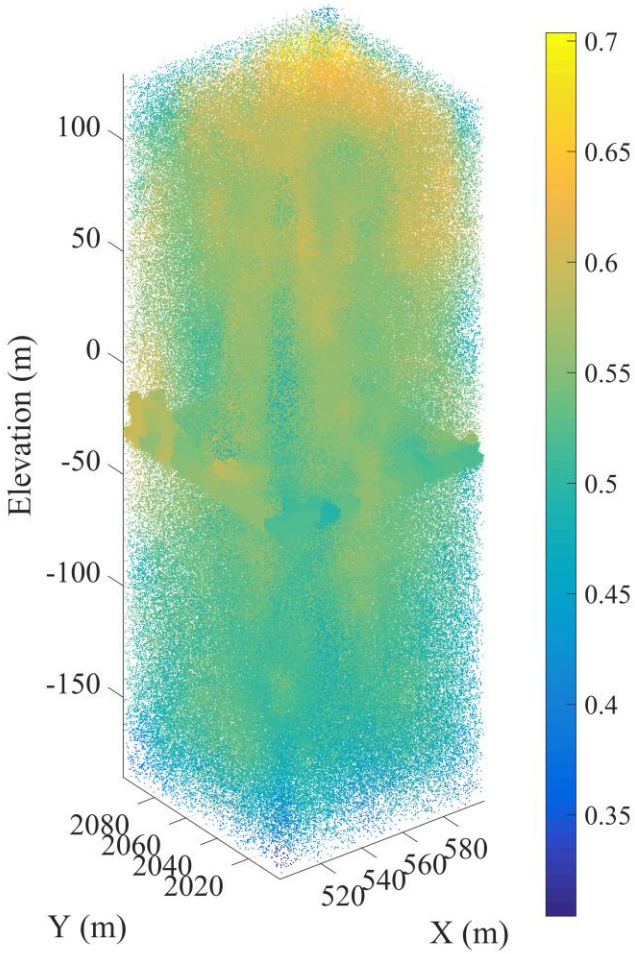

Figure 6-3 Estimated expected number of points for each voxel using VS model. The data is colored by the expected number of points.

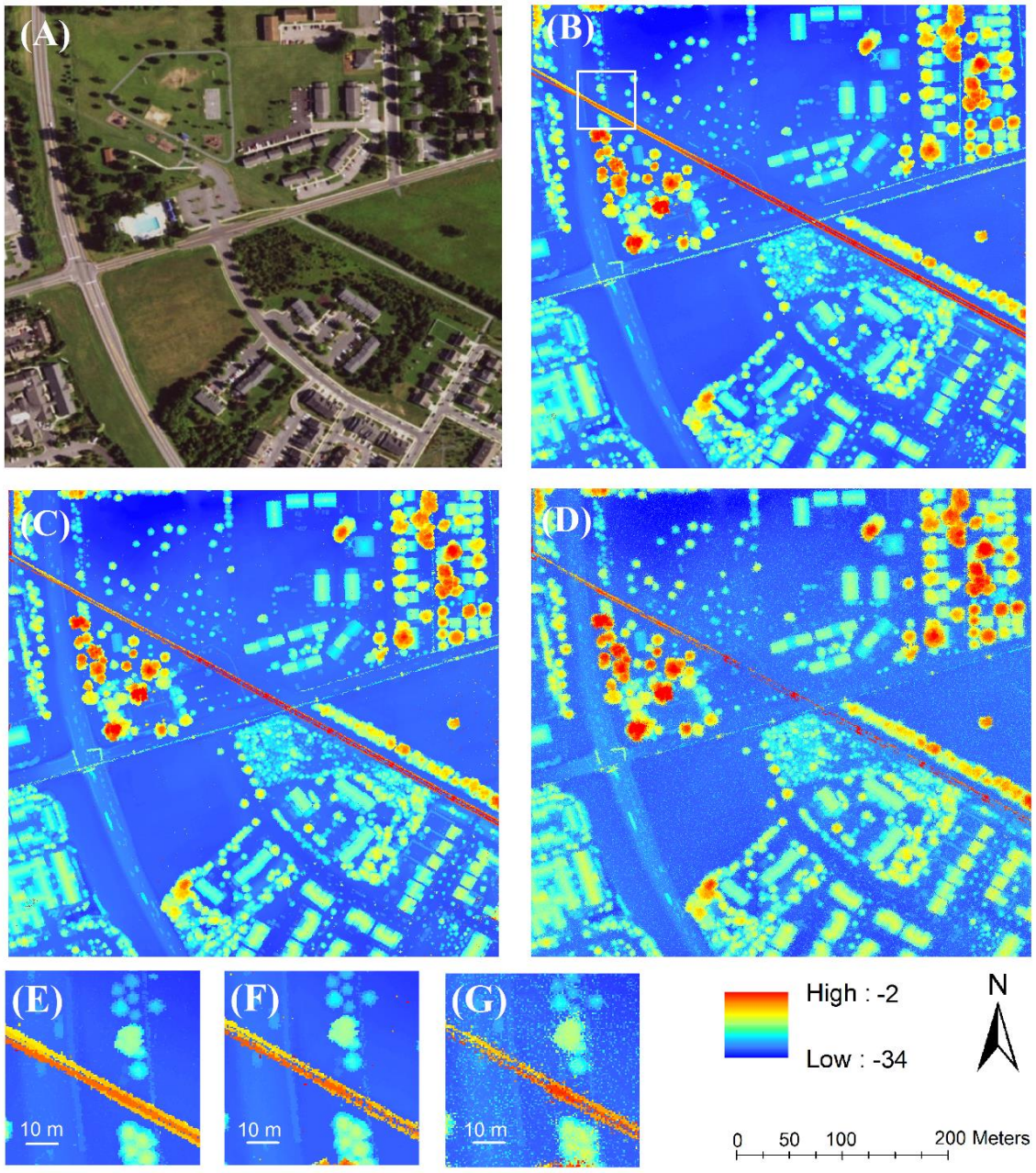

Figure 6-4 Filtered results of the Easton area. Satellite image (A). VS-AES result (B). AES only result (C) and DCC result (D). Detailed view of the powerline (E) (F) (G) corresponding to (B) (C) and (D). The zoom in area is labeled in (B) with a white square. The results are colored by elevation.

Table 6-1 Statistical result for the extraction of transmission lines with three filtering methods.

	Number of correctly identified	Detection rate	Number of misclassified	False alarm rate
Raw data	57185	N/A	N/A	N/A
VSAES	50925	89.1%	2884	5.4%
AES	14802	25.9%	799	5.1%
DCC	7666	13.4%	2016	20.8%

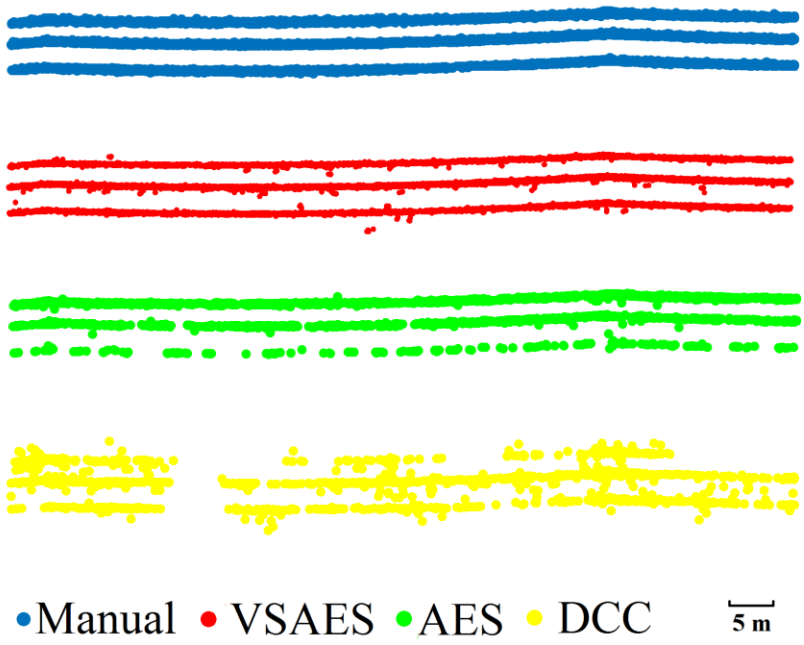

Figure 6-5 Vertical profile of the transmission lines from manually selected raw data and filtering result using VSAES, AES and DCC method.

From Table 6-1, we can see that the proposed method retains 89.1% of the power line points with only a few incorrectly classified noise returns. For comparison, AES keeps only 25.9% of the transmission line points and DCC retains only 13.4%. From Figure 6-5, we can see that the transmission line points retained in the VSAES results discriminate the three separate cables clearly even though a few noise points remain misclassified close to the wires. For the AES result, the upper two lines are well defined but the extraction of the third line is not complete with a large number of gaps appearing. For the DCC result, clear gaps can be found in all three cables and more noise points appear close to the transmission lines. The optical image for the transmission lines are displayed in Figure 6-7. Both the visual check and statistical analysis show that the extraction of weak signal points is improved by combining the temporally spaced observations and using the VSAES filtering approach.

Next we check the results for a distribution line whose wires have an even smaller diameter than the transmission line. As before, we manually extracted signal points for the distribution line. One thing to notice is that because of the low laser energy returned from distribution lines, even manual extraction is very hard and its accuracy is likely lower than that for larger transmission lines. Again, we define an examination region with the same size, 7×7 m (Height × Width) to evaluate the performance of the three filters; the statistics for distribution line extraction are given in Table 6-2.

For the extraction of distribution lines, the proposed VSAES method detects only 60% of the line points, but still significantly more than the 29.3% for the AES method and 11.1% for the DCC method. From Figure 6-6 we can see that the lowest wire in

Table 6-2 Statistical result of extraction of distribution lines using three filtering methods. The meaning of each column is the same as Table 6-1.

	Number of correctly identified	Detection rate	Number of misclassified	False alarm rate
Raw data	20793	N/A	N/A	N/A
VSAES	12265	60.0%	1042	7.8%
AES	6089	29.3%	594	8.9%
DCC	2305	11.1%	639	41.6%

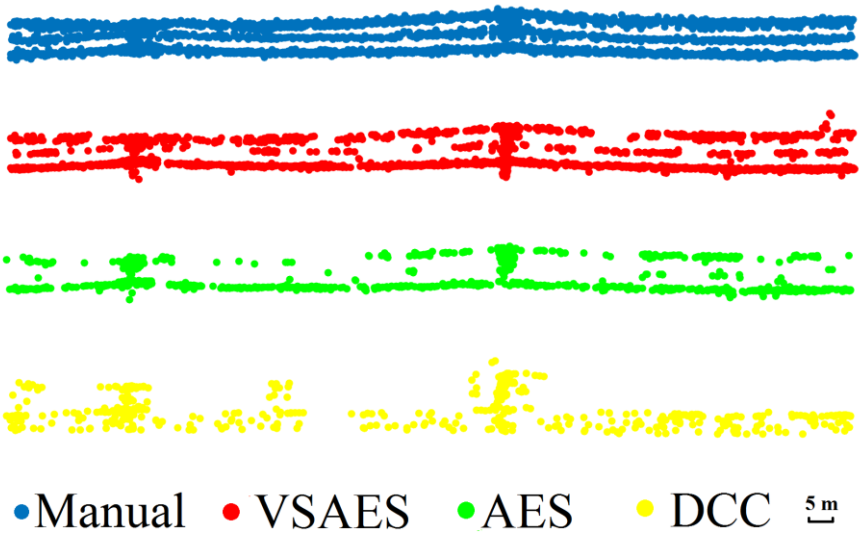

Figure 6-6 Vertical profile of the distribution lines from manually selected raw data and filtered result using VSAES, AES and DCC method.

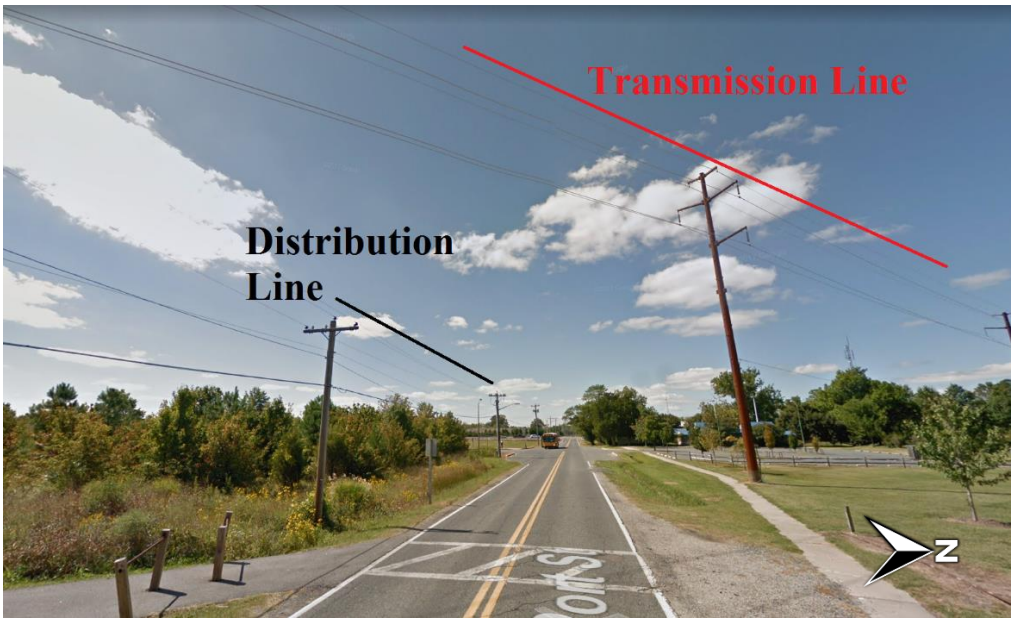

Figure 6-7 Ground view image of the Easton study area. The red line depicts the transmission lines and the black line shows the distribution lines. The north arrow shows an approximate north direction.

VSAES profile is well detected with only a small gap. The top line has more gaps but there are still enough return points to accurately depict the distribution wire geometry. Results for the middle wire is the worst with larger areas containing gaps. However, the results are still markedly better than from the other two filtering methods, and appear to contain enough points to model the distribution line. The optical image for distribution lines is also displayed in Figure 6-7.

Finally, we examine performance for an additional distribution line in the Lufkin flight area. The filtered result with VSAES, AES, and DCC are displayed in Figure 6-8. The detailed sub-figures in Figure 6-8 show a region at an intersection of two distribution lines. Results from the proposed method retain both lines and clearly shows two lines. Only one line can be seen clearly from the AES result while the other is difficult to see. For the DCC results, no linear features are visible. We also display vertical profiles and statistical analysis for the three filtered results in Figure 6-9 and Table 6-3.

The proposed method significantly outperformed both the AES and DCC methods by correctly classifying 85.9% distribution line points versus 37.9% and 6.1% respectively. The top line in the VSAES result is well extracted, while a few gaps can be found on the middle and bottom wire. By visual inspection of an oblique street view image (Figure 6-10), we see that there are 3 wires at the top level and only one line at the middle and bottom levels. Thus, the top line in the vertical profile is composed from signal returns from three distribution lines resulting in a clear line with no gaps in the figure.

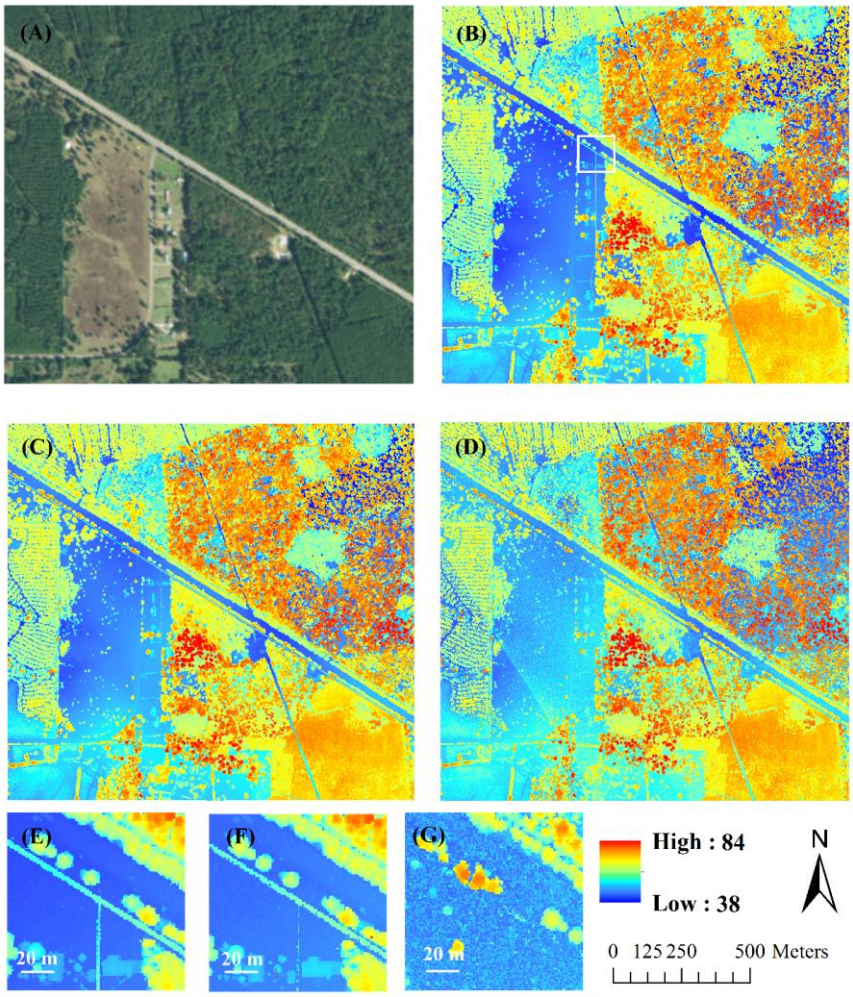

Figure 6-8 Filtered results of the Lufin area. Satellite image (A). VS-AES result (B). AES result (C) and DCC result (D). Detailed view of the powerline (E) (F) (G) corresponding to (B) (C) and (D). The zoom in area is labeled in (B) with a white square. The results are colored by elevation.

Table 6-3 Statistical result of extraction of distribution lines using three filtering methods. The meaning of each column is the same as Table 6-1.

	Number of correctly identified	Detection rate	Number of misclassified	False alarm rate
Raw data	104542	N/A	N/A	N/A
VSAES	89836	85.9%	5250	5.5 %
AES	39367	37.9%	2622	6.2%
DCC	6370	6.1%	980	13.3%

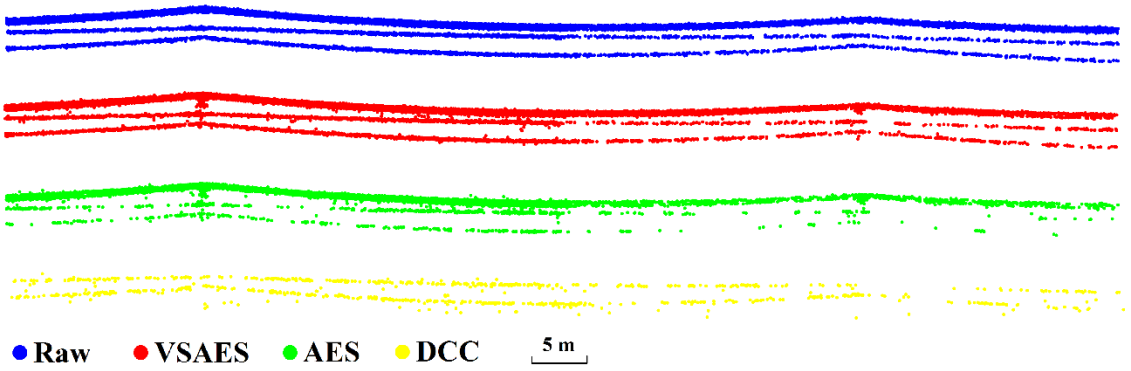

Figure 6-9 Vertical profile of the transmission lines at Oncor area from manually selected raw data and filtered result using VSAES, AES and DCC method.

Figure 6-10 Ground view image of the Lufkin study area. The north arrow shows an approximate north direction.

6.5 Discussion

From the comparison of filtered results from the 3 sets of powerlines, we can see a significant improvement in extracting powerline points using the proposed method. The improvements seen in the VSAES results are primarily because of two factors: the consideration of the local point cloud geometry during filtering and the combination of overlapping flight lines before filtering. Returns from the wires align two-dimensionally, which makes the calculated three dimensional point density for each wire point relatively small. The DCC method filters SPL data using the resolution of a one dimensional range bin and retains all the points in the data bin as signal points if the query data bin satisfies the filtering criteria. This 1-D filtering mechanism makes DCC have limited efficiency for powerlines. However, if we consider the two-dimensional nature of the powerline (adapting to the local point cloud geometry), then VSAES can more effectively extract power line points compared to methods that do not consider the local nature of the point cloud.

In addition, due to the limited overlap between any power cable and the footprint of one laser shot, there are only a small number of signal photons bounced back to the SPL system. Because of the statistical nature of the sensor (i.e. relatively low photon detection efficiency), even fewer photons are recorded by the system, making them difficult to distinguish from noise in a single flightline. In this circumstance, even considering only local geometry information with the AES method is not sufficient to effectively retain enough powerline points; we need to consider all observations simultaneously, and the proposed VSAES method can fully utilize data from different observations and even different flightline collections. The powerlines are illuminated

from different directions and the probability that the sensor receives photons from each part of the powerline therefore is increased, which enhances the spatial correlation of the powerline points and therefore helps to improve the filtered result.

An additional advantage of VSAES over AES is the mathematical robustness of the former method. Even though both VSAES and AES consider local geometry information through a PCA, they utilize different standards to differentiate signal from noise. In AES, we count the number of neighbors for a query point in a sphere and an ellipsoid determined by PCA; the difference of these two numbers is used as the decision variable and compared to an empirically determined threshold. The performance of the filtering results relies on a proper selection of this threshold. By contrast, the proposed VSAES method utilizes a filtering criteria based on a hypothesis test and the selection of a statistical 95% confidence threshold. Therefore, the selection of the threshold is more objective and the filtered result is more robust as a result.

One thing to note is that even considering the enhanced spatial correlation and local geometry distribution from overlapping flight observations, there are still a number of powerline points missing, for example, the result of distribution line at Easton area (shown in Figure 6-6). By checking corresponding optical image (see Figure 6-7), we observe that the top and middle lines are thinner than the bottom one and this likely explains the higher number of missing points for them. For a direct comparison, we also evaluated a laser scanning data set for the same distribution line from a linear-mode airborne Lidar system. The data was collected on June 14th 2016 using a Leica ALS 80 sensor operated at ~1.3 km AGL and the nominal point density is ~25 points/m^2. The top view and vertical profile of the distribution line from the linear-mode data is shown in

Figure 6-11. From the vertical profile we can see that even though the bottom wire is well defined, the top and middle lines are missing in the linear-mode data. The energy of the return signal is too low for the linear-mode system to detect, and would require an even lower flight height to model these lines. However, in the SPL point cloud (flown at ~2 km AGL), the top and middle lines are defined with enough points to model them. This also indicates that SPL has an advantage over LMAL for powerline monitoring because the data can be collected from higher flight heights.

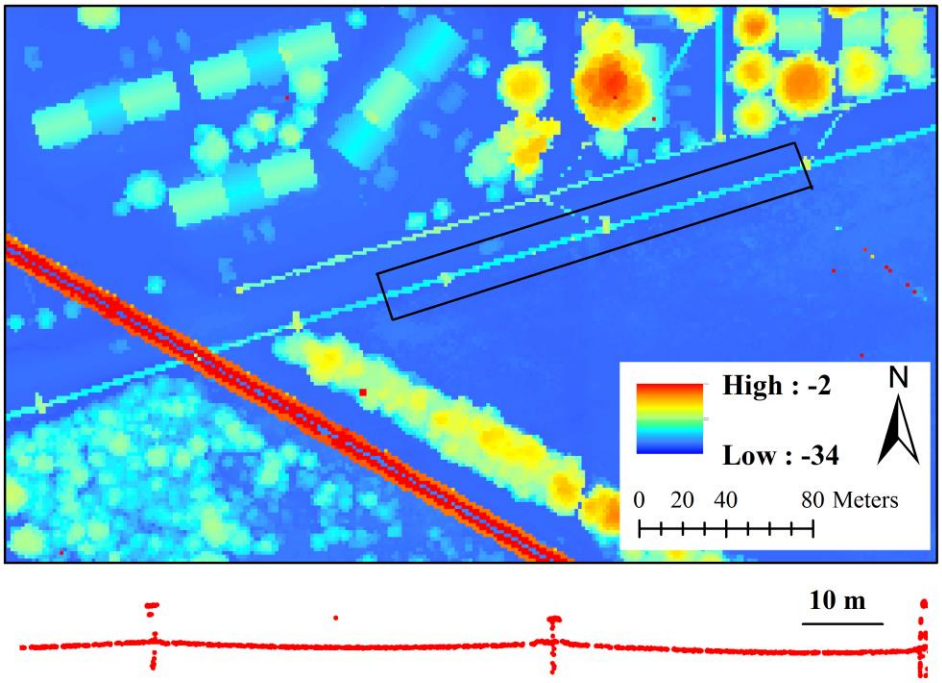

Figure 6-11 Top view of the distribution line area from linear-mode LiDAR data (top). Vertical section of the distribution line labeled in the black rectangle (bottom). Note that this profile is identical to the location given in Figure 6-6 for the SPL data.

Finally, we compare the performance of VSAES and AES for strong reflectors, such as rooftops. We selected 5 rooftops and compared the filtered result using both AES and VSAES to that of LMAL data. We also manually filtered the SPL data as a benchmark. The results are shown in Table 6-4.

Table 6-4 Comparison between the AES and the VSAES method. RMSE in meters between the filtered results and the reference LMAL data is shown.

	Manual	AES	VSAES
Roof 1	0.05	0.06	0.07
Roof 2	0.11	0.11	0.11
Roof 3	0.12	0.12	0.13
Roof 4	0.15	0.16	0.16
Roof 5	0.07	0.09	0.09

For the combined point clouds, the probability that noise points clustered near the targets is higher. As a result, the VSAES filter may have a higher probability of misclassifying these clustered noise points. However, from Table 6-4 we can see that the VSAES results are as good as AES results, considering that 1 cm of difference should not be considered significant given the expected ranging accuracy of the sensor (usually 2-5 cm).

6.6 Conclusions

In this chapter, an improved VSAES method was proposed to extract weak reflections from features such as powerlines from combined SPL point clouds. The proposed method first reorganizes the combined data by tiling it into data blocks, during which the spatial correlation of signal points is improved. Then the VS model is used to estimate the expected number of points in each voxel and solves the problem of uneven noise density while also balancing the computational load. At last, an improved AES method, based on a hypothesis test, is used to filter the data. The combined VSAES method used on a complete SPL data set (instead of on a flightline by flightline basis) makes a significant improvement for extracting weak signals such as returns from power lines. For the experimental dataset from the Easton area, 89% of the transmission line points are extracted versus 25.9% for the AES method and 13.4% for the DCC method.

For distribution line points, whose return signal is even weaker (smaller wire sizes), the proposed VSAES method extracted 60% of the signal points versus 29.3% for AES and 11.1% for DCC. For the Lufkin, TX dataset, the extraction result is 85.9% versus 37.9% and 6.1% (VSAES, AES and DCC respectively). We also demonstrated that points from thin powerlines, though not recorded in a coincident LML dataset, can be extracted from SPL data. The high quantum sensitivity and high data collecting efficiency gives the SPL system great potential for future powerline monitoring. The VSAES method may be also beneficial at other applications, such as extraction of ground surface under dense canopy or low reflectance targets.

Chapter 7

Afterpulse Removal in Single Photon LiDAR Data Using Robust Regression

High quantum sensitivity makes SPL systems susceptible to false returns from two primary sources: dark/solar noise and afterpulses. In the previous chapters 4-6, methods for removing dark/solar noise have been discussed. Though these methods have been shown to remove dark/solar noise effectively, they have limited effect on afterpulse removal because of the correlated nature of afterpulse returns. In this chapter, a method to remove afterpulses is presented and discussed.

7.1 Background

An afterpulse is a secondary pulse emitted by the detector after the primary pulse related to the detection of a photon [98]. It is caused by amplification of secondary electrons originating from positive ions during the ionization of residual gases in a photomultiplier tube (PMT) [99]–[102], or by amplification of carriers trapped by defects and impurities on deep levels in the multiplication layer of avalanche photodiodes (APD) [103], [104] . Unlike solar noise, afterpulses can only be recorded by the system after the detector has been triggered (by signal returns), and its point density is usually higher than that of solar noise; it is also not randomly distributed. Thus, in a SPL dataset, afterpulses are always found clustered beneath the signal returns from strong reflectors. Due to these unique characteristics current noise filtering approaches have limited success removing afterpulses. Afterpulses have been studied in the telecommunication

industry and mitigated using hardware solutions such as sine wave gating (SG) or self-differencing (SD) techniques [105]–[109], but to date there have not been studies of methods for detecting and eliminating afterpulses for SPL systems. Afterpulses deteriorate the quality of SPL data, especially for hard surfaces such as architectural features and ground that are commonly of highest interest for data users. Therefore, an effective way to remove afterpulses is desirable.

7.2 Algorithm

Herein, we propose an individual shot-based afterpulse removal method, in which robust regression is applied to define surface structure, and then points below the defined surface are removed. Robust regression is a form of regression analysis used to circumvent some limitations of other conventional methods such as ordinary least square (OLS) which are highly sensitive to outliers [110], [111]. Afterpulse points and possible vegetation points are difficult to effectively remove as outliers when applying methods such as OLS to surfaces, and can easily cause these approaches to fail. In these circumstances, robust regression is an effective tool to define the true signal return surface. Robust regression first defines an objective function and then iterates with varied weights applied to each of the observations. This approach enables outlier points to have little influence on the final regression results because they will have small weights applied. More details on robust regression can be found in [110], [111]. As a pre- and post-processing step to afterpulse removal, two different solar noise filtering methods: DCC [23] and VSAES [90] are also applied separately. The processing workflow is shown in Figure 7-1.

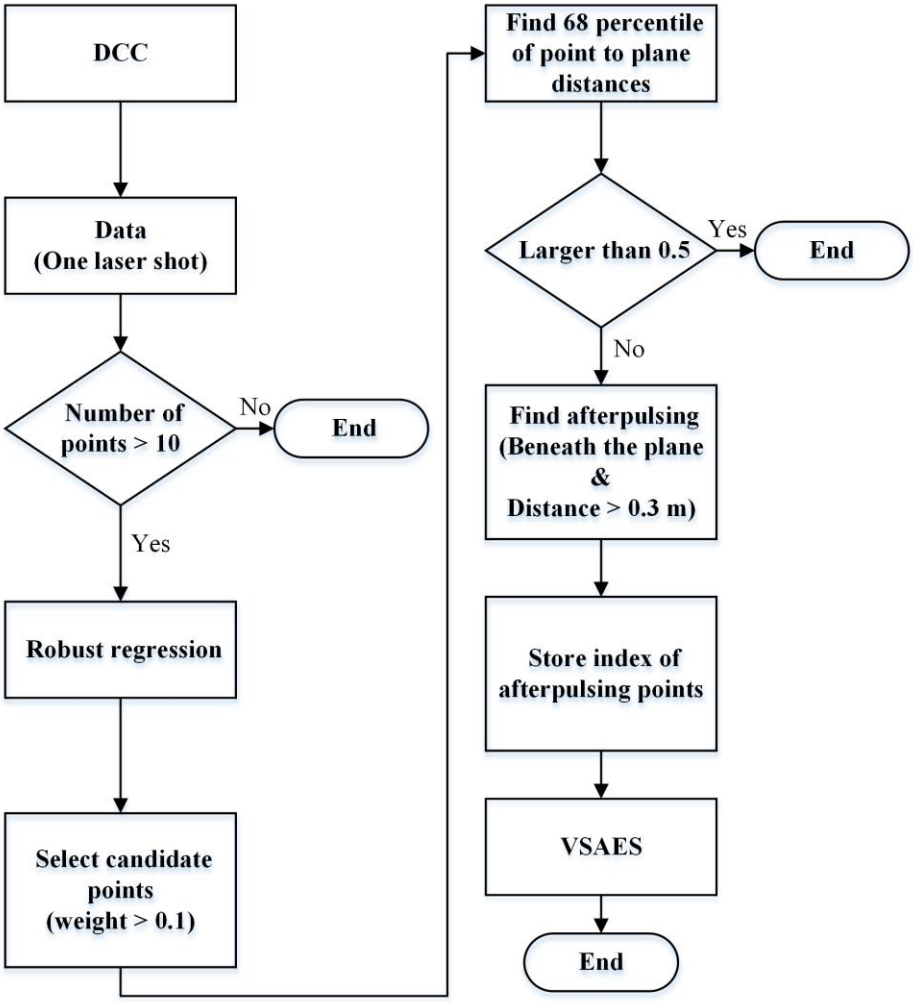

Figure 7-1 Overall flowchart of the proposed afterpulse removal method. The flowchart demonstrates the processing chain for each laser shot.

The data in each laser shot is first coarsely filtered using the DCC method. This method is chosen because it retains nearly all the signal and afterpulse points and is also computationally efficient. Two parameters are required for the DCC method: a coarse filtering bin size to determine the filtering threshold and a fine filtering bin size to remove the noise points. The coarse filtering bin size was set to 30 m as suggested in [23] and the fine filtering bin size was set to 5 m. After a manual verification of the data, we found that most of the afterpulse noise appears to be in a band up to 2-3 meters beneath the surface (this is demonstrated in the results section). Therefore, to guarantee retaining

all possible afterpulse points, we selected a 5 m fine bin size; this parameter can be easily modified based on the source of the input dataset.

Most of the solar noise returns are removed by the DCC process, leaving primarily signal points, afterpulse points and a few unfiltered solar noise returns. Robust regression is then applied to the filtered data from each laser shot with an initial weight of 1 for each data point, during which each point is assigned a new weight iteratively. Points with weight larger than 0.1 are selected as candidate hard surface points. This threshold was determined empirically and can be tuned by application. From the results of the iterative robust regression, it is expected that afterpulse points will be excluded and only hard surface points used to fit a planar surface. However, in some situations, when there are a large percentage of signal points above the surface, for example from the tree canopy or structures on the rooftop, the regression algorithm will assign both the surface points and the additional high signal points a high weight and then fit the plane to all of them. Thus the performance of the regression result needs to be validated before the fitted surface is used to remove possible afterpulse points. To automate this assessment we check the 68 percentile of the sorted point-to-plane distances, if it is smaller than an empirically determined threshold (0.5 m is used in this paper), the regression results are deemed to be reliable. Here we assume the distribution of the point-to-plane distances are subject to a Gaussian distribution and examine data below the one standard deviation range resulting 68 percentile of sorted distances. If the regression results fail to pass the percentile examination, the current shot is left as indeterminate and the filter continues to process the next shot. The frequency of percentile test failures depends upon the scene

contents for the scanned area. For bare ground and building areas, the test usually passes while failure is more common in heavily vegetated areas.

If the percentile test is passed, then all the returns from the shot that are 0.3 m lower than the fitted plane are labeled as afterpulse points. The 30 cm threshold is determined based on the dead time of the sensor and the diffusion of the dataset. For the SPL100 system, the dead time is quoted as 1.6 ns which corresponds to 24 cm in range. Due to ranging errors, geolocation errors and timing jitter the SPL signal points for hard surfaces generally form a plane with a thickness of ~10-20 cm. Therefore, a conservative estimate of 30 cm is selected as the threshold used herein. This threshold can obviously be tuned based on the SPL dataset characteristics. Finally, the labeled afterpulse points are removed and the whole dataset is then filtered using the VSAES method.

7.3 Experimental data set

The SPL data used in the experiment was collected with an SPL100 system manufactured by Sigma Space Corporation, a division of Leica Geosystems. The SPL100 is an updated version of the HRQLS system. The experimental dataset covers the main campus of the University of Houston (Houston, TX, USA) and was collected on February 25th, 2017. The system was operated at ~4200 m above the ground level (AGL) and the imaged point density is ~30 points per square meter.

A linear-mode airborne LiDAR (LMAL) dataset collected by an Optech Titan system was used as ground truth to examine the performance of the proposed SPL filtering method. The Titan system is a multispectral airborne LiDAR system manufactured by Teledyne Optech Inc. which emits laser pulses in a zigzag pattern at

wavelengths of 532, 1064 and 1550 nm with a field of view of ±30° [112]. The acquisition occurred on February 16th, 2017 at ~500 m AGL with a raw point density of ~12 per square meter. The combined three color laser point cloud was used as a reference to check the spatial performance of the proposed SPL filtering method, and the green (532 nm) LMAL laser data alone was also used to explore the relationship between target reflectance and the presence of afterpulse noise. Figure 7-2 shows an overview optical image of the study area.

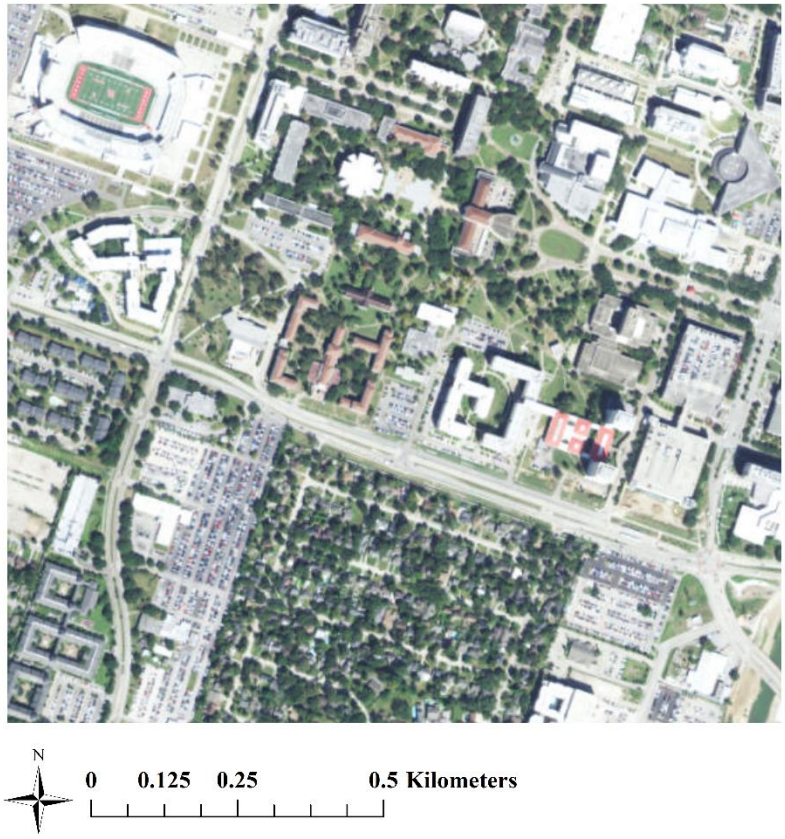

Figure 7-2 Overview optical image of the study area.

7.4 Results

We applied the proposed afterpulse removal method and VSAES filtering to the experimental dataset described earlier. The point cloud after removal of solar/dark noise

and afterpulses is shown in Figure 7-3. To evaluate the effectiveness of the afterpulse removal routine, we first check performance on building rooftops. A vertical profile of two representative rooftops is shown in Figure 7-4. We can see that the afterpulse points are removed effectively. To quantitatively examine the results, we selected 20 rooftops (each with an area of ~ 75 m^2) from the study dataset (labeled in Figure 7-3) and compared the number of filtered afterpulse points removed to a manual count of the number of afterpulses. The results are given in Table 7-1. Since there is no difference between a solar noise point and an afterpulse point, herein, we regard all the noise points within a 5 m range beneath the rooftop as afterpulse points from manual inspection.

From the results in Table 7-1 we can see that the proposed method effectively removes ~90% of the afterpulse points. Also, we can see that even though the area of each rooftop is the same, the number of afterpulse points varies by a couple orders of magnitude. A detailed discussion of this variability will be provided in next section.

Next we evaluate the performance of the afterpulse filter for terrain modeling. First, we classify ground points for the two filtered results: one using only the VSAES to remove solar noise and the second using both the proposed afterpulse removal method and VSAES. The classification was performed using the Terrascan (www.terrasolid.com) embedded ground classification routine and the parameters used were: 88° for terrain angle, 10° for iteration angle and 1.4 m for iteration distance. No manual corrections to the filtered point cloud were applied. A digital terrain model (DTM) was generated from

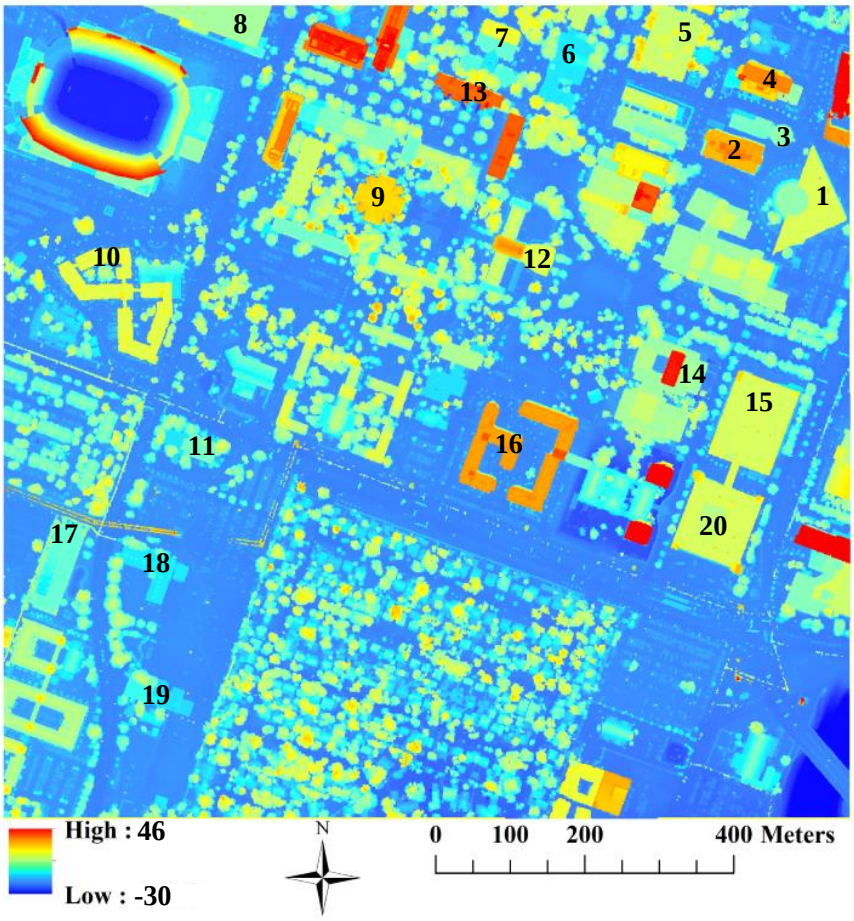

Figure 7-3 Filtered point cloud of study area. The points are colored by elevation. 20 representative rooftops examined for a quantitative assessment of filter performance are labeled.

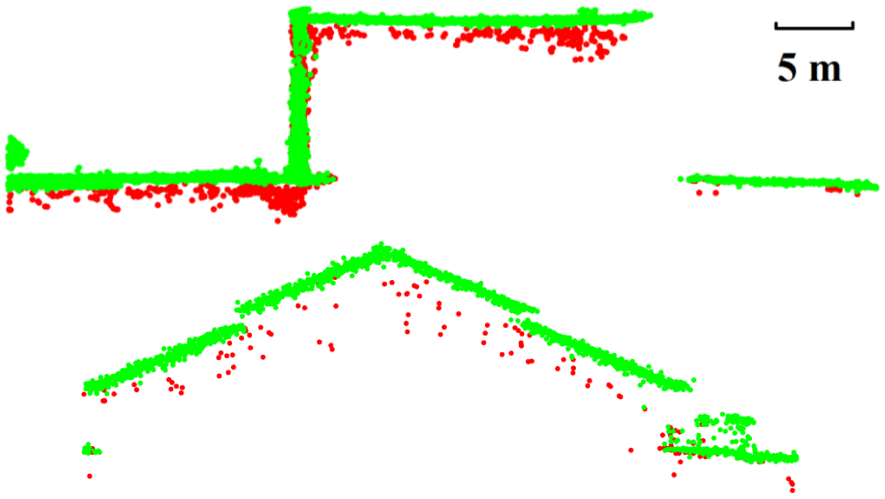

Figure 7-4 Two representative rooftop profiles to demonstrate afterpulse removal. Red points are the filtered result when using VSAES only and green points are when VSAES and the proposed afterpulse removal method are both applied. The width of both vertical profiles is 2 m.

Table 7-1 Statistical comparison between the results from the proposed method and manual classification. We manually labeled all the noise points within a 5 m range beneath each rooftop as afterpulse points. The area of each rooftop is ~75 m^2.

Rooftop ID	Manually removed	Algorithm removed	Rate
1	650	591	90.9%
2	455	407	89.5%
3	612	550	89.9%
4	989	927	93.7%
5	230	220	95.7%
6	174	134	77.0%
7	664	636	95.8%
8	587	476	81.1%
9	337	314	93.2%
10	599	579	96.7%
11	210	181	86.2%
12	178	139	78.1%
13	361	341	94.5%
14	75	67	89.3%
15	430	357	83.0%
16	180	169	93.9%
17	588	536	91.2%
18	1558	1464	94.0%
19	542	453	83.6%
20	243	213	87.7%
Overall	9662	8754	90.6%
Mean	483	438	89.2%

the classified ground points. We also generated a reference DTM using the reference LMAL data which was automatically classified and manually validated by the National Center for Airborne Laser Mapping (www.ncalm.org). We then generated elevation difference between the DTM products from the experimental data and the reference DTM, with the results presented in Figure 7-5.

In Figure 7-5 we can clearly see the difference between the two results. With afterpulses removed, the elevation differences in most areas have a mean close to zero. The larger differences mainly appear around buildings because of occlusions caused by scanning geometry and the interpolation algorithm applied to fill gaps in the DTMs.

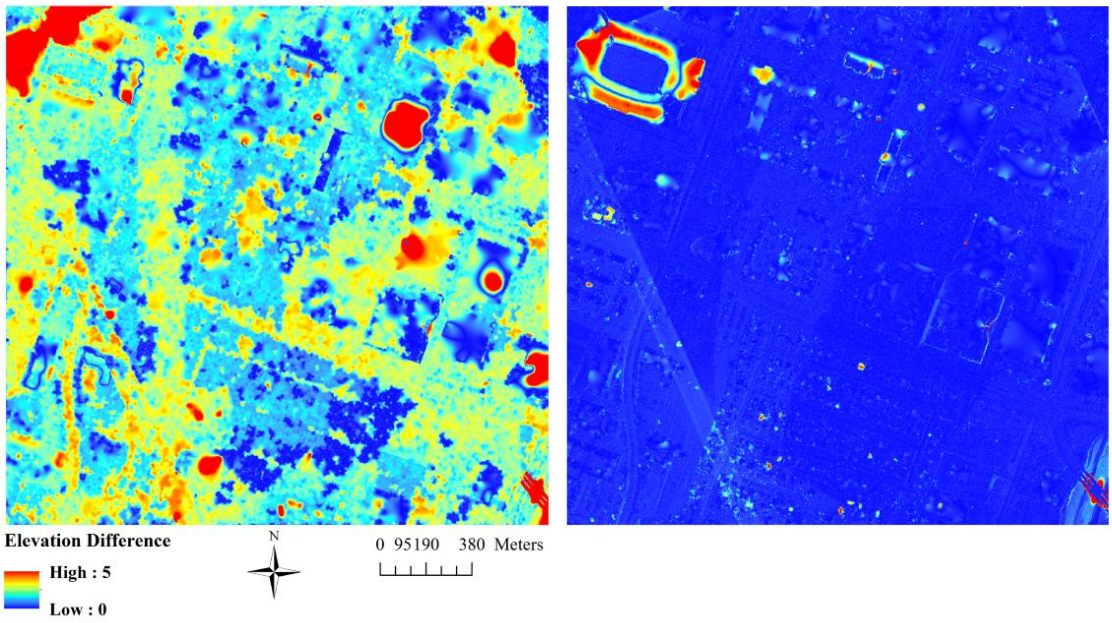

Figure 7-5 Absolute elevation difference to the reference ground DEM from the result with (right) and without (left) removal of afterpulse points using the proposed method. The figure is colored by elevation difference and only shows differences from 0 to 5 m.

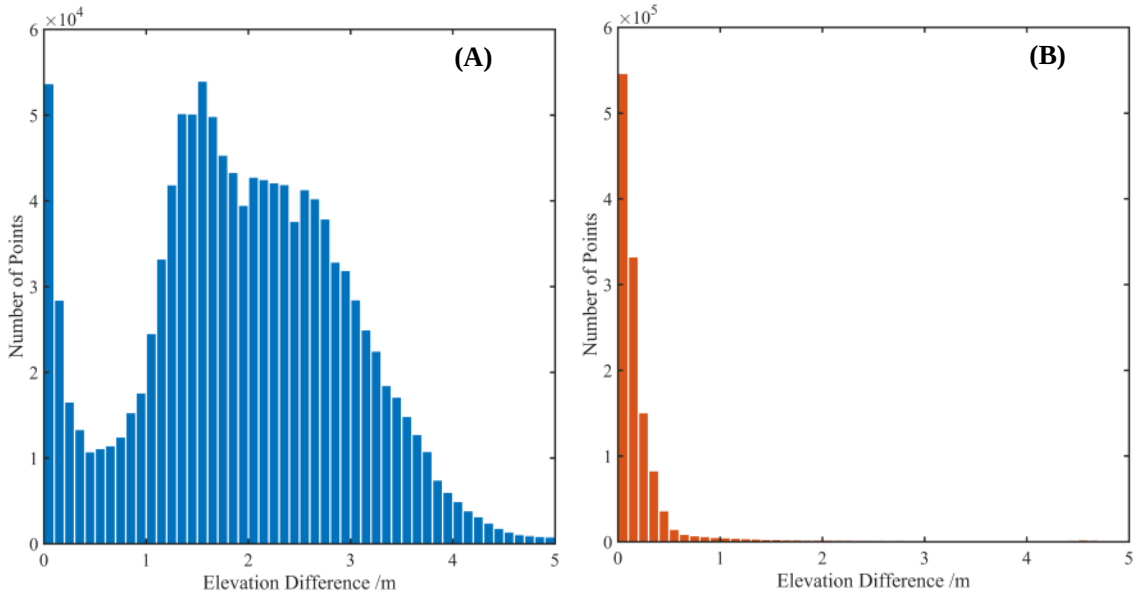

Figure 7-6 Distribution of elevation differences shown in Figure 7-5. (A) is for results with VSAES only and (B) is for results with afterpulses removed. Also, we only plot elevation difference ranging from 0 to 5 m to demonstrate the distribution of elevation differences.

There are two remaining areas with large elevation differences, one in the northwest corner due to a stadium; because of the large footprint of the stadium bleachers

interpolation causes large elevation difference. The other area is in the southeast corner where there is a bridge over a river; the automatic classification from Terrascan didn't properly classify these features.

The distributions of the elevation differences were also analyzed and the results are shown in Figure 7-6. For the VSAES only result, the mean difference is 1.95 m while the mean difference for the afterpulse filtered result is only 0.23 m. We can also see that for the VSAES only result there are clearly many areas with large elevation differences. This is because of the large number of afterpulse points under the primary return surfaces that confuses the Terrascan classification routine leading to a big elevation differences when compared to the reference ground model. Most ground filters typically start by gridding the data coarsely and then using the lowest points in each bin as ground points [33]. This works well for LMAL because there are no afterpulses but for SPL this means that all of the initial ground candidate points are likely afterpulse points which will cause a bias to the final ground model as the candidate points are not likely to be removed.

7.5 Discussion

The filtered result from the proposed method for afterpulse removal shows good agreement with the reference linear-mode LiDAR data. The proposed method is able to remove ~90% of afterpulse points on buildings. The remaining undetected afterpulses are mainly a result of the following conditions: heavily vegetated areas, complex structures on top of buildings and building corners. These all make it difficult for the proposed method to fit a reliable plane to signal returns and effectively remove afterpulse points.

Examining Figure 7-6 (A) again, we see that the elevation difference distribution can be divided into two parts, one from 0 to 0.5 m and the other from 0.5 to 5 m. The latter part is clearly elevation errors caused by unfiltered afterpulse points as discussed in the results section. The first portion indicates that in some areas, there are either very few afterpulse points or that the afterpulse points are removed using VSAES only. Many density based filtering methods may be able to remove afterpulse points to some degree, especially if they are sparse. However, removal relies on time-consuming parameter tuning and also risks misclassification of signal points if the filter is set to aggressively remove clustered afterpulses. The proposed method aims to remove afterpulses based on local geometry instead of point density. Thus it is effective in removing afterpulses while still retaining signal returns.

The relationship between the number of afterpulse points, the number of signal points, and return intensity were also examined. In the previous section, we mentioned that even though all the rooftops examined had the same approximate area, the number of afterpulse points varied widely between rooftops. To better demonstrate the change in the number of afterpulses, we examined each laser shot and counted the number of signal points and the number of classified afterpulse points. The results are shown in Figure 7-7. For each laser shot, we obtain a data pair: the number of signal points and the number of afterpulse points. The color scale in Figure 7-7 indicates the number of data pairs that fall on each integer coordinate location. We can see that there is most commonly ~10-20 afterpulse points and ~80-100 signal points for each laser shot (of 100 beamlets). There is also a clear trend that shows with an increase in signal points, afterpulse points are more probable to appear. The statistical analysis displayed in Figure 7-7 was conducted on the

coarsely filtered result (applying the DCC method only) to ensure that a majority of the afterpulse points were included. It should be noted, that while the number of afterpulse points is reliable, the number of signal points may be less accurate because the DCC method does not remove all of the solar/dark noise points; the result is some noise in the statistical analysis, however this should not affect the overall trends shown in Figure 7-7. To better understand the characteristics of afterpulses better, we compare the number of afterpulse points to the average intensity recorded for the coincident linear-mode LiDAR data.

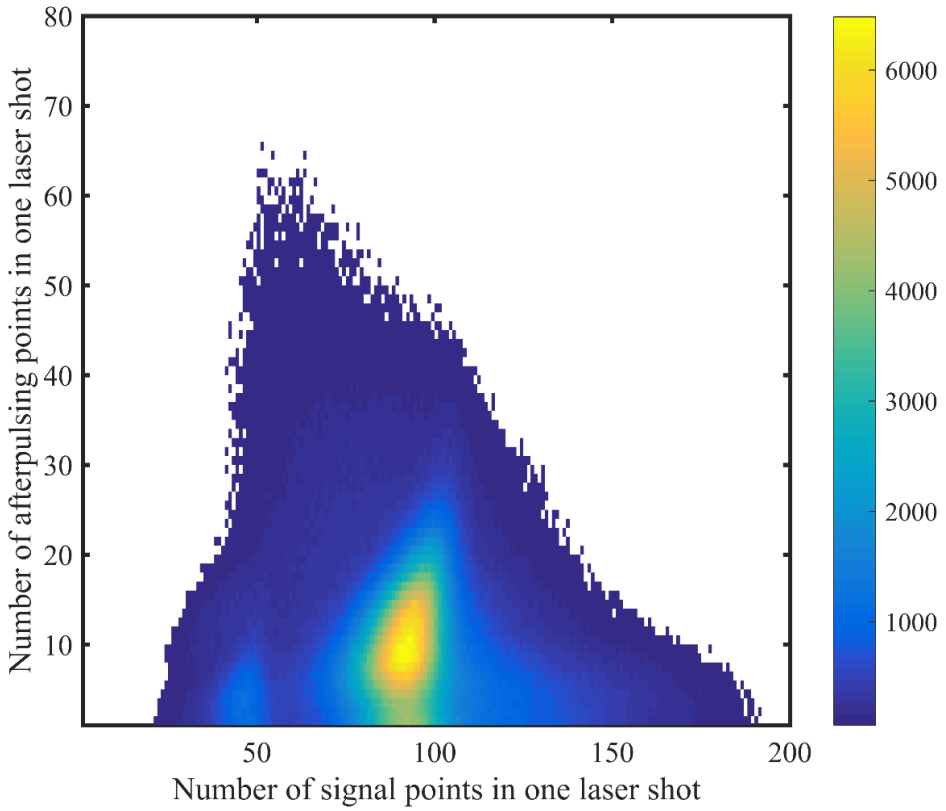

Figure 7-7 Relationship between the number of afterpulses and number of signal points for each laser shot. Each coordinate indicates a data pair consisting of number of afterpulses (y) and number of signal points (x) colored by the number of data pairs falling at each integer coordinate location.

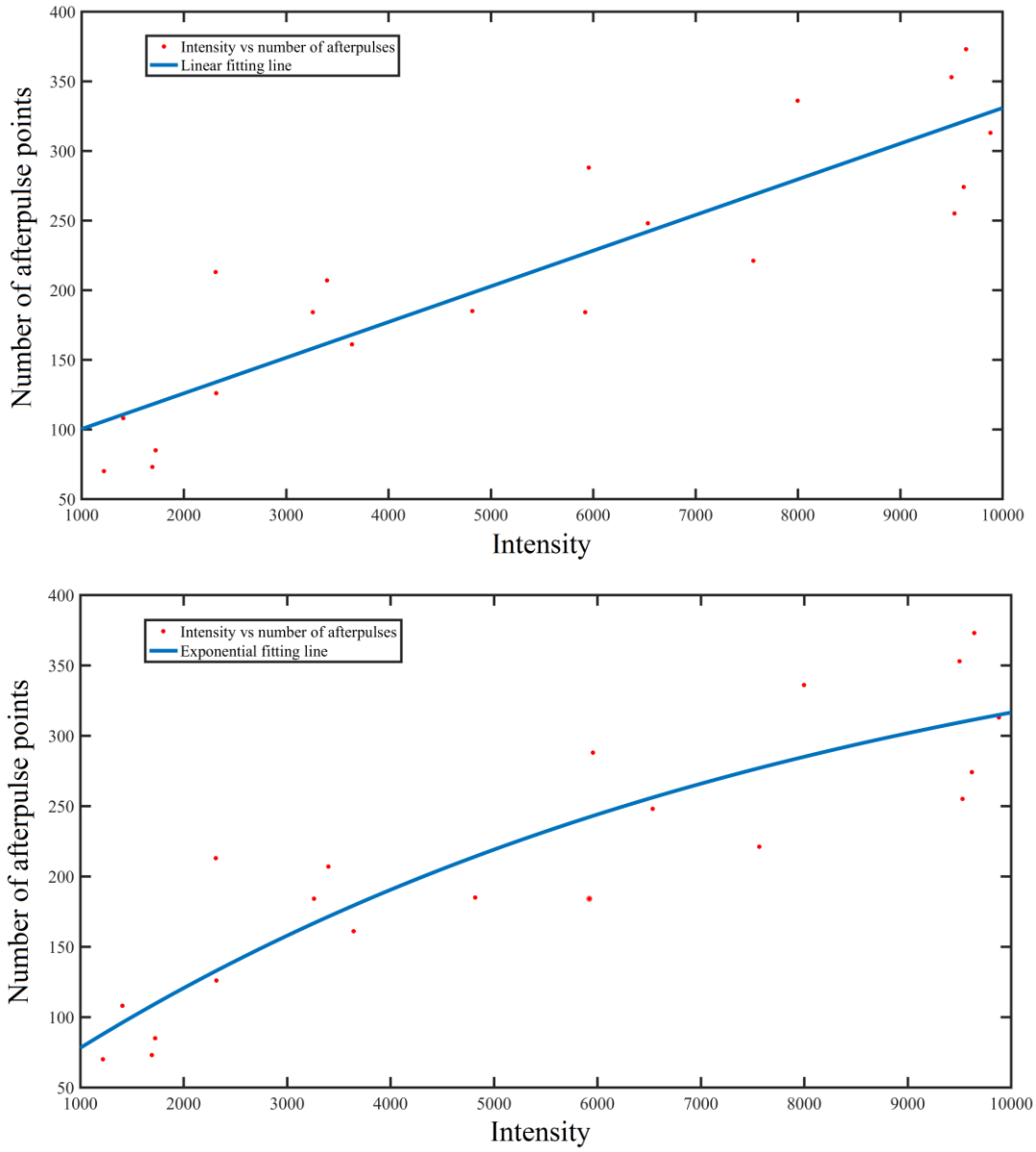

Figure 7-8 Relationship between number of afterpulses and average return signal intensity for the 20 selected rooftops

Figure 7-8 shows the relationship between the number of afterpulses and the mean LMAL return intensity for the same area for the rooftops depicted in Figure 7-5. Intensity from the Titan green laser point cloud for the rooftop areas was obtained and the mean intensity for each sample area was calculated. This mean intensity was then plotted w.r.t. the number of afterpulse points identified. We fitted the resultant points with a linear model, obtaining an R^2 of 0.77. This linear regression clearly shows number of afterpulse

points increases with increasing return signal strength. The stochastic detection process of an SPL system is a Poisson process [47]. Therefore, we would expect an exponential relationship between the number of incident photons and detections, and thus we then also fitted the data with exponential functions as shown in Figure 7-8 bottom figure. The exponential model fits the data at a moderate level with R^2 of 0.77. Several reasons may explain this. First, the LMAL intensity data is not calibrated, although it was corrected for range and incidence angle effects. The different scanning geometry between LMAL and SPL may also introduce some errors. Finally, we regarded all the noise points within 5 m range beneath the plane as afterpulses while some of them might be solar/dark noise returns – it is impossible to discriminate between the two.

It should also be noted that the SPL100 system operates at a green wavelength, thus enabling the possibility of bathymetric mapping. There were several small water bodies outside the study area that were examined and they clearly showed that a shortcoming of the proposed afterpulse removal method is that it incorrectly removes bathymetric returns because they appear as afterpulses to returns from the water surface. For water body areas, the surface of the water reflects most of the laser energy and forms a good planar surface that can easily be identified by the afterpulse removal algorithm. Thus bathymetric areas should be processed separately without afterpulse removal if benthic layer retrieval is desired.

7.6 Conclusions

Afterpulse noise points are one of the significant sources of error in SPL datasets, but have received little attention in the current literature. The clustering of afterpulses

beneath strong reflectors gives them a different statistical pattern from solar/dark noise, and thus makes them difficult to remove using existing SPL filtering methods. In this chapter, we proposed and tested a new method of removing afterpulse points from SPL data. The method utilizes local geometry information based on robust regression and was effective at removing most afterpulse points while still retaining signal points. In the experiment, around 90% of afterpulse points beneath rooftops were removed. For terrain areas, the proposed method decreased the mean elevation difference to reference linear-mode data from 1.95 m to 0.23 m using a conventional automated ground filtering algorithm. However, the proposed method does still have some shortcomings; for heavily vegetated areas, complex structures and water bodies, the proposed method has either limited effectiveness or misclassifies bathymetric signal points. Future work will attempt to improve the performance of afterpulse removal for these special situations.

Chapter 8

Conclusions and Future Work

8.1 Contributions of the dissertation and conclusions

New generation single photon LiDAR systems are able to collect data much more effectively than linear-mode LiDAR systems due to their high quantum sensitivity. However, this high quantum sensitivity also leads to a much higher noise rate, which can deteriorate the quality of SPL datasets if not properly classified. In this dissertation, filtering methods for SPL data were studied and the following contributions have been made.

In Chapter 4, a novel point density based algorithm was proposed for filtering 2-D single photon LiDAR profiles. The algorithm considers the probability distribution function of distances to the *k*-th nearest neighbors. Then Bayesian decision theory is applied to calculate the probability of a point being signal or noise. We also adaptively scaled the noise level based on the estimated noise rate provided in the MABEL data before filtering to ensure a homogeneous noise rate within the whole dataset. This proposed noise scaling significantly improves the performance on green channels when using point density based methods. The proposed method was applied to two MABEL datasets of CA and MO. The extracted ground surfaces were compared with high accuracy airborne laser scanning data. The RMSE between the filtered CA MABEL profile and the ALS is ~6 meters for MABEL's green channels and ~4 meters for the near-infrared channels. The RMSE for comparison between the MABEL profile and ALS data for the MO test dataset is ~2 meters. The results showed that the profiled ground

surface can be reliably extracted by the proposed method. The proposed method was also compared with mDBSCAN, a point density based algorithm. mDBSCAN with and without noise rescaling was applied to the same datasets, both of which removed fewer noise points than the proposed method did. Also the proposed method outperformed mDBSCAN at steep areas since mDBSCAN works with only horizontal interrogation regions.

In Chapter 5, a novel AES method was proposed to filter the 3-D imaging SPL data. The AES method was designed to solve two problems: inhomogeneous noise distribution and near-signal noise removal. The AES method has two steps. In the first step, a spherical model for noise density estimation is established to balance the influence of inhomogeneous noise levels throughout the point cloud. Then the quotient of the number of neighbors and the estimated noise density is used as the rule to initially filter the input data. In the second step, a morphing ellipsoid is used to filter near-signal noise points. Local PCA is applied to adapt the size and orientation of the ellipsoid to the local signal points. The change in the numbers of points in the original sphere and the morphing ellipsoid is regarded as the metric for noise classification. The AES method was tested on a SPL point cloud from Easton, MD collected by the HRQLS system. A voxel-based filtering method was applied to the same dataset for comparison. Linear-mode ALS data was used as a reference, and the filtered results from the two methods on different types of targets were evaluated. We found that the RMSE on solid planes was 0.09 m versus 0.11 m, 0.12 m versus 0.14 m for bare ground and 2.07 m versus 2.55 m for vegetation canopy for the AES and voxel methods respectively. We also manually

selected several solid planar reference surfaces and found that the proposed method successfully removed twice as many noise points as the voxel-based method.

Then in Chapter 6, an improved VSAES method was proposed to retain weak signals from combined SPL point clouds (i.e. overlapping in space and/or time) during the filtering process. The proposed method first reorganizes the combined data by tiling it into data blocks, during which the spatial correlation of signal points is improved. Then the VS model is used to estimate the expected number of points in each voxel. By employing this VS model, our proposed method can simultaneously process a combined SPL data set containing multiple flightlines, in which the noise density is unevenly distributed throughout the whole data set. Finally, an improved AES method, based on a hypothesis test, is used to filter the data more robustly than the original version. The combined VSAES method used on a complete SPL data set (instead of on a flightline by flightline basis) makes a significant improvement for extracting weak signals such as returns from powerlines. For the experimental dataset from the Easton area, 89% of the transmission line points were extracted versus 25.9% for the AES method and 13.4% for the DCC method. For distribution line points, whose return signal is even weaker (smaller wire sizes), the proposed VSAES method extracted 60% of the signal points versus 29.3% for AES and 11.1% for DCC. For the Lufkin, TX dataset, the extraction result was 85.9% versus 37.9% and 6.1% (VSAES, AES and DCC respectively). We also demonstrated that the points from thin powerlines, though not recorded in a coincident LMAL dataset, can be extracted from SPL data. The high quantum sensitivity and high data collecting efficiency gives the SPL system great potential for future powerline monitoring.

Finally, in Chapter 7, a new method of removing afterpulse points from SPL data was discussed. Afterpulses have different characteristics from solar/dark noise and thus can not be removed effectively by density-based solar noise filters. The proposed method utilizes robust regression to define target surfaces in each laser shot and removes points beneath it. The regression result is validated by checking point-to-plane distances. The validation process ensures that the regression result is not influenced by signal points above the target surface such as returns from vegetation. The proposed method was tested on SPL dataset of the University of Houston main campus. The VSAES method was also applied to remove solar/dark noise for comparison. Performance of the afterpulse removal method for buildings and ground were evaluated. For buildings, 20 representative rooftops were examined and it was found that 90% of the afterpulse points on average were removed. For the ground surface, we examined the RMSE between DSM's generated from the SPL dataset and the reference LMAL dataset. The proposed method successfully reduced the RMSE from 1.95 m to 0.23 m. In addition, positive correlation between the number of afterpulses and return intensity was found, and fitting of the number afterpulses versus return intensity gave an R^2 of 0.77 with both a linear model and an exponential model.

8.2 Future work

Recommendations for future work include the following two major areas: improving computational efficiency of the filter and retrieving intensity information for targets.

8.2.1 Improved computational efficiency

The filtering algorithms introduced in Chapter 5 and 6 are point-based, which means the algorithm has to iterate on each point in the dataset. Other published methods, histogram- or voxel-based for example, operate by iterating on each data bin or voxel. Thus, the proposed methods have lower computational efficiency than these other methods. Herein, we propose two possible ways to improve the computation efficiency.

One way is to implement the proposed methods in C/C++. In this dissertation, all the methods were developed with Matlab. Though efficient for matrix computations, Matlab is not optimized for complex calculations. One of the novelties of the proposed method is to accommodate local point geometry with a morphed ellipsoid defined by a local PCA. However, calculating PCA for all the points requires iteration in Matlab, which lowers the overall computational efficiency. Iteration is not as significant a bottleneck in C/C++ and thus the methods will run in a much more effective manner.

Another computational efficiency could be realized by using Mahalanobis distance to neighbors for each point instead of calculating PCA. Mahalanobis distance utilizes standard deviation as the metric instead of absolute distance and thus has potential to help remove near-signal noise. Mahalanobis distance can be computed with matrix computation. Therefore, even with Matlab, application of Mahalanobis distance is capable of significantly improving computational efficiency.

Also, multiple-thread computation with GPU (graphics processing unit) is a potential way to improve computational efficiency. GPUs have recently been used in many different fields such as artificial intelligence, data mining, and scientific simulations. The proposed filtering methods implies simple operations on each point

individually, and the results for each point does not influence operation of other points. This mechanism is therefore an excellent fit for parallel computation and thus implementation with GPU multiple-thread computations will help improve computational efficiency.

8.2.2 Intensity retrieving

As introduced in Chapter 2, SPL detectors operate in a binary mode which means that the number of incident photons does not make any difference on the magnitude of output photocurrent, and thus no intensity information is available. However, with some processing, intensity information might be retrieved using properly filtered SPL data. Detection events modeled as a Poisson process and the probability of triggering the detector is one minus the probability of zero. If the number of incoming photons increases, detection probability goes up too. And the number of incoming photons is correlated to target reflectance, or in other words, intensity of target photons. A higher detection probability indicates larger number of returns from the target are recorded. Therefore, it is possible to establish a relationship between the point density and the intensity. And the relationship is expected to be exponential.

The experiment might start with examining only hard surfaces, such as building rooftop areas and the ground surface. Targets with a large range of reflectance distribution are preferable. Then the mean point density of each target can be calculated. The point density should be normalized with respect to number of flight lines, overlap between continuous shots and other related factors so that point density is only related to the target reflectance. A reference data with intensity information is required, either hyperspectral data or LiDAR data with the same wavelength. Finally, an exponential

regression model can be applied to the point density and the corresponding intensity value.

It should be noted that for SiPM-based SPL systems, intensity can be estimated as a proportion of the output voltage. However, the accuracy of this measurement has not been fully investigated and still requires validation. If this estimated intensity is not sufficient, combining it with detection probability estimation may be a better choice.

Bibliography

[1] J. R. Dymond, J. D. Shepherd, and J. Qi, "A Simple Physical Model of Vegetation Reflectance for Standardising Optical Satellite Imagery," *Remote Sens. Environ.*, vol. 75, no. 3, pp. 350–359, Mar. 2001.

[2] C. P. Lo, D. A. Quattrochi, and J. C. Luvall, "Application of high-resolution thermal infrared remote sensing and GIS to assess the urban heat island effect," *Int. J. Remote Sens.*, vol. 18, no. 2, pp. 287–304, Jan. 1997.

[3] J. Hasch, E. Topak, R. Schnabel, T. Zwick, R. Weigel, and C. Waldschmidt, "Millimeter-Wave Technology for Automotive Radar Sensors in the 77 GHz Frequency Band," *IEEE Trans. Microw. Theory Tech.*, vol. 60, no. 3, pp. 845–860, Mar. 2012.

[4] W. M. Kaula, G. Schubert, R. E. Lingenfelter, W. L. Sjogren, and W. R. Wollenhaupt, "Apollo laser altimetry and inferences as to lunar structure," in *Lunar and Planetary Science Conference Proceedings*, 1974, vol. 5, pp. 3049–3058.

[5] F. Clapuyt, V. Vanacker, and K. Van Oost, "Reproducibility of UAV-based earth topography reconstructions based on Structure-from-Motion algorithms," *Geomorphology*, vol. 260, pp. 4–15, May 2016.

[6] D. Pflugmacher, W. B. Cohen, R. E. Kennedy, and Z. Yang, "Using Landsat-derived disturbance and recovery history and lidar to map forest biomass dynamics," *Remote Sens. Environ.*, vol. 151, pp. 124–137, Aug. 2014.

[7] Z. Pan, C. L. Glennie, J. C. Fernandez-Diaz, C. J. Legleiter, and B. Overstreet, "Fusion of LiDAR Orthowaveforms and Hyperspectral Imagery for Shallow River

Bathymetry and Turbidity Estimation," *IEEE Trans. Geosci. Remote Sens.*, vol. 54, no. 7, pp. 4165–4177, Jul. 2016.

[8] J. Yang and J. Kerekes, "A combined approach for ice sheet elevation extraction from lidar point clouds," in *2014 IEEE Western New York Image and Signal Processing Workshop (WNYISPW)*, 2014, pp. 15–18.

[9] X. Zhang, C. Glennie, and A. Kusari, "Change Detection From Differential Airborne LiDAR Using a Weighted Anisotropic Iterative Closest Point Algorithm," *IEEE J. Sel. Top. Appl. Earth Obs. Remote Sens.*, vol. 8, no. 7, pp. 3338–3346, Jul. 2015.

[10] Xiaoye Liu, "Airborne LiDAR for DEM generation: some critical issues," *Prog. Phys. Geogr.*, vol. 32, no. 1, pp. 31–49, Feb. 2008.

[11] X. Liu and Z. Zhang, "Drainage network extraction using LiDAR-derived DEM in volcanic plains," *Area*, vol. 43, no. 1, pp. 42–52, Jun. 2010.

[12] M. D. McCoy, G. P. Asner, and M. W. Graves, "Airborne lidar survey of irrigated agricultural landscapes: an application of the slope contrast method," *J. Archaeol. Sci.*, vol. 38, no. 9, pp. 2141–2154, Sep. 2011.

[13] R. Hesse, "LiDAR-derived Local Relief Models - a new tool for archaeological prospection," *Archaeol. Prospect.*, vol. 17, no. 2, pp. 67–72, 2010.

[14] J. Fernandez-Diaz, W. Carter, R. Shrestha, and C. Glennie, "Now You See It… Now You Don't: Understanding Airborne Mapping LiDAR Collection and Data Product Generation for Archaeological Research in Mesoamerica," *Remote Sens.*, vol. 6, no. 10, pp. 9951–10001, Oct. 2014.

[15] A. F. Chase, D. Z. Chase, J. F. Weishampel, J. B. Drake, R. L. Shrestha, K. C.

Slatton, J. J. Awe, and W. E. Carter, “Airborne LiDAR, archaeology, and the ancient Maya landscape at Caracol, Belize,” *J. Archaeol. Sci.*, vol. 38, no. 2, pp. 387–398, Feb. 2011.

[16] A. B. Davies and G. P. Asner, “Advances in animal ecology from 3D-LiDAR ecosystem mapping,” *Trends Ecol. Evol.*, vol. 29, no. 12, pp. 681–691, Dec. 2014.

[17] C. R. Lane and E. D’Amico, “Calculating the Ecosystem Service of Water Storage in Isolated Wetlands using LiDAR in North Central Florida, USA,” *Wetlands*, vol. 30, no. 5, pp. 967–977, Oct. 2010.

[18] A. S. Antonarakis, S. S. Saatchi, R. L. Chazdon, and P. R. Moorcroft, “Using Lidar and Radar measurements to constrain predictions of forest ecosystem structure and function,” *Ecol. Appl.*, vol. 21, no. 4, pp. 1120–1137, Jun. 2011.

[19] B. A. Brooks, S. E. Minson, C. L. Glennie, J. M. Nevitt, T. Dawson, R. Rubin, T. L. Ericksen, D. Lockner, K. Hudnut, V. Langenheim, A. Lutz, M. Mareschal, J. Murray, D. Schwartz, and D. Zaccone, “Buried shallow fault slip from the South Napa earthquake revealed by near-field geodesy,” *Sci. Adv.*, vol. 3, no. 7, p. e1700525, Jul. 2017.

[20] J. Telling, C. Glennie, A. Fountain, and D. Finnegan, “Analyzing Glacier Surface Motion Using LiDAR Data,” *Remote Sens.*, vol. 9, no. 3, p. 283, Mar. 2017.

[21] Y. Guo, G. Huang, and R. Shu, “3D imaging laser radar using Geiger-mode APDs: analysis and experiments,” in *Technology*, 2010, pp. 768402–768402.

[22] J. Degnan, J. McGarry, T. Zagwodzki, P. Dabney, J. Geiger, R. Chabot, C. Steggerda, J. Marzouk, and A. Chu, “Design and performance of an airborne multikilohertz photon-counting microlaser altimeter,” *Int. Arch. Photogramm.*

Remote Sens. Spat. Inf. Sci., vol. 34, no. 3/W4, pp. 9–16, 2001.

[23] J. J. Degnan, "Photon-counting multikilohertz microlaser altimeters for airborne and spaceborne topographic measurements," *J. Geodyn.*, vol. 34, no. 3–4, pp. 503–549, Oct. 2002.

[24] V. Molebny, G. Kamerman, and O. Steinvall, "Laser radar : from early history to new trends," vol. 7835, pp. 6–9, 2010.

[25] R. Heinrichs, B. F. Aull, R. M. Marino, D. G. Fouche, a K. McIntosh, J. J. Zayhowski, T. Stephens, M. E. O'Brien, and M. a Albota, "Three-dimensional laser radar with APD arrays," *Soc. Photo-Optical Instrum. Eng. Conf. Ser.*, vol. 4377, pp. 106–117, 2001.

[26] R. M. Marino, T. Stephens, R. E. Hatch, J. L. McLaughlin, J. G. Mooney, M. E. O'Brien, G. S. Rowe, J. S. Adams, L. Skelly, and R. C. Knowlton, "A compact 3 D imaging laser radar system using Geiger-mode APD arrays- System and measurements," *Proc. SPIE*, vol. 5086, pp. 1–15, 2003.

[27] T. Bahr and P. Smith, "Airborne Geiger-Mode LiDAR for Large-Scale, High-Resolution Wide-Area Mapping," *GI_Forum*, vol. 1, pp. 85–93, 2016.

[28] J. J. Degnan, C. Field, R. Machan, E. Leventhal, D. Lawrence, Y. Zheng, R. Upton, J. Tillard, and S. Howell, "Recent Advances in Photon-Counting , 3D Imaging Lidars," no. November, pp. 8–13, 2007.

[29] B. F. Aull, A. H. Loomis, D. J. Young, R. M. Heinrichs, B. J. Felton, P. J. Daniels, and D. J. Landers, "Geiger-mode avalanche photodiodes for three-dimensional imaging," *Lincoln Lab. J.*, vol. 13, no. 2, pp. 335–349, 2002.

[30] M. a. Itzler, M. Entwistle, M. Owens, K. Patel, X. Jiang, K. Slomkowski, S.

Rangwala, P. F. Zalud, T. Senko, J. Tower, and J. Ferraro, “Geiger-mode avalanche photodiode focal plane arrays for three-dimensional imaging LADAR,” *Proc. SPIE. 7808, Infrared Remote Sens. Instrum. XVIII*, vol. 7808, p. 78080C, 2010.

[31] Hamamatsu-Photonics, “Photomultiplier Tubes Basics and Applicatioins,” 1999.

[32] J. Degnan, “Scanning, Multibeam, Single Photon Lidars for Rapid, Large Scale, High Resolution, Topographic and Bathymetric Mapping,” *Remote Sens.*, vol. 8, no. 11, p. 958, Nov. 2016.

[33] X. Meng, N. Currit, and K. Zhao, “Ground Filtering Algorithms for Airborne LiDAR Data: A Review of Critical Issues,” *Remote Sens.*, vol. 2, no. 3, pp. 833–860, Mar. 2010.

[34] X. Meng, L. Wang, J. L. Silván-Cárdenas, and N. Currit, “A multi-directional ground filtering algorithm for airborne LIDAR,” *ISPRS J. Photogramm. Remote Sens.*, vol. 64, no. 1, pp. 117–124, 2009.

[35] J. Shan and S. Aparajithan, “Urban DEM generation from raw {LiDAR} data,” *Photogramm. Eng. Remote Sens.*, vol. 71, no. 2, pp. 217–226, 2005.

[36] K. Zhang and D. Whitman, “Comparison of Three Algorithms for Filtering Airborne Lidar Data,” *Photogramm. Eng. Remote Sens.*, vol. 71, no. 3, pp. 313–324, 2005.

[37] M. Elmqvist, E. Jungert, F. Lantz, Å. Persson, and U.Söderman, “Terrain Modelling and Analysis Using Laser Scanner Data,” *Int. Ach. Photogramm. Remote Sens*, vol. XXXIV, pp. 211–218, 2001.

[38] R. Passini, D. Betzner, and K. Jacobsen, “Filtering of digital elevation models,”

ASPRS Annu. Conv. Washingt., p. 9, 2002.

[39] G. Vosselman, "Slope based filtering of laser altimetry data," *Int. Arch. Photogramm. Remote Sensing, Vol. 33, Part B3/2*, vol. 33, no. Part B3/2, pp. 678–684, 2000.

[40] X. Meng, L. Wang, and N. Currit, "Morphology-based Building Detection from Airborne Lidar Data," *Photogramm. Eng. Remote Sens.*, vol. 75, no. 4, pp. 437–442, Apr. 2009.

[41] J. Zhang and J. Kerekes, "An Adaptive Density-Based Model for Extracting Surface Returns From Photon-Counting Laser Altimeter Data," *IEEE Geosci. Remote Sens. Lett.*, vol. 12, no. 4, pp. 726–730, Apr. 2015.

[42] Z. Zhang, Y. Zhao, Y. Zhang, L. Wu, and J. Su, "A real-time noise filtering strategy for photon counting 3D imaging lidar," *Opt. Express*, vol. 21, no. 8, p. 9247, Apr. 2013.

[43] U. C. Herzfeld, B. W. McDonald, B. F. Wallin, T. A. Neumann, T. Markus, A. Brenner, and C. Field, "Algorithm for Detection of Ground and Canopy Cover in Micropulse Photon-Counting Lidar Altimeter Data in Preparation for the ICESat-2 Mission," *IEEE Trans. Geosci. Remote Sens.*, vol. 52, no. 4, pp. 2109–2125, Apr. 2014.

[44] B. Chen and Y. Pang, "A denoising approach for detection of canopy and ground from ICESat-2's airborne simulator data in Maryland, USA," in *Applied Optics and Photonics China (AOPC2015)*, 2015, p. 96711S.

[45] L. A. Magruder, M. E. Wharton, K. D. Stout, and A. L. Neuenschwander, "Noise filtering techniques for photon-counting ladar data," in *SPIE Defense, Security,*

and Sensing, 2012, p. 83790Q.

[46] K. H. Horan and J. P. Kerekes, "An automated statistical analysis approach to noise reduction for photon-counting lidar systems," in *2013 IEEE International Geoscience and Remote Sensing Symposium - IGARSS*, 2013, pp. 4336–4339.

[47] T. Cossio, K. C. Slatton, W. Carter, K. Shrestha, and D. Harding, "Predicting topographic and bathymetric measurement performance for low-SNR airborne lidar," *IEEE Trans. Geosci. Remote Sens.*, vol. 47, no. 7, pp. 2298–2315, 2009.

[48] P. Gatt, S. Johnson, and T. Nichols, "Geiger-mode avalanche photodiode ladar receiver performance characteristics and detection statistics," *Appl. Opt.*, vol. 48, no. 17, p. 3261, Jun. 2009.

[49] Z. Liu, W. Hunt, M. Vaughan, C. Hostetler, M. McGill, K. Powell, D. Winker, and Y. Hu, "Estimating random errors due to shot noise in backscatter lidar observations," *Appl. Opt.*, vol. 45, no. 18, pp. 4437–4447, 2006.

[50] C. Glennie, "Rigorous 3D error analysis of kinematic scanning LIDAR systems," *J. Appl. Geod.*, vol. 1, no. 3, Jan. 2007.

[51] J. J. Degnan and C. T. Field, "Moderate to high altitude, single photon sensitive, 3D imaging lidars," in *SPIE Sensing Technology + Applications*, 2014, p. 91140H.

[52] S. Johnson, P. Gatt, and T. Nichols, "Analysis of Geiger-mode APD laser radars," in *Proceedings of SPIE*, 2003, vol. 5086, pp. 359–368.

[53] M. a. Itzler, R. Ben-Michael, C.-F. Hsu, K. Slomkowski, A. Tosi, S. Cova, F. Zappa, and R. Ispasoiu, "Single photon avalanche diodes (SPADs) for 1.5 μm photon counting applications," *J. Mod. Opt.*, vol. 54, no. 2–3, pp. 283–304, Jan. 2007.

[54] H. T. van Dam, S. Seifert, R. Vinke, P. Dendooven, H. Lohner, F. J. Beekman, and D. R. Schaart, "A Comprehensive Model of the Response of Silicon Photomultipliers," *IEEE Trans. Nucl. Sci.*, vol. 57, no. 4, pp. 2254–2266, Aug. 2010.

[55] J. Y. Yeom, R. Vinke, N. Pavlov, S. Bellis, L. Wall, K. O'Neill, C. Jackson, and C. S. Levin, "Fast Timing Silicon Photomultipliers for Scintillation Detectors," *IEEE Photonics Technol. Lett.*, vol. 25, no. 14, pp. 1309–1312, Jul. 2013.

[56] SensL, "An introduction to SiPM," 2011.

[57] M. D. Eisaman, J. Fan, A. Migdall, and S. V. Polyakov, "Invited Review Article: Single-photon sources and detectors," *Rev. Sci. Instrum.*, vol. 82, no. 7, p. 071101, 2011.

[58] Hamamatsu Photonics, "Photomultiplier Tubes and Related Products," 2006.

[59] A. C. Brenner, J. P. DiMarzio, and H. J. Zwally, "Precision and Accuracy of Satellite Radar and Laser Altimeter Data Over the Continental Ice Sheets," *IEEE Trans. Geosci. Remote Sens.*, vol. 45, no. 2, pp. 321–331, Feb. 2007.

[60] B. E. Schutz, H. J. Zwally, C. A. Shuman, D. Hancock, and J. P. DiMarzio, "Overview of the ICESat Mission," *Geophys. Res. Lett.*, vol. 32, no. 21, p. L21S01, 2005.

[61] M. R. Siegfried, R. L. Hawley, and J. F. Burkhart, "High-Resolution Ground-Based GPS Measurements Show Intercampaign Bias in ICESat Elevation Data Near Summit, Greenland," *IEEE Trans. Geosci. Remote Sens.*, vol. 49, no. 6, pp. 3393–3400, Sep. 2011.

[62] T. Schenk and B. Csatho, "A New Methodology for Detecting Ice Sheet Surface

Elevation Changes From Laser Altimetry Data," *IEEE Trans. Geosci. Remote Sens.*, vol. 50, no. 9, pp. 3302–3316, Sep. 2012.

[63] J. Kohler, T. A. Neumann, J. W. Robbins, S. Tronstad, and G. Melland, "ICESat Elevations in Antarctica Along the 2007–09 Norway–USA Traverse: Validation With Ground-Based GPS," *IEEE Trans. Geosci. Remote Sens.*, vol. 51, no. 3, pp. 1578–1587, Mar. 2013.

[64] W. Abdalati, H. J. Zwally, R. Bindschadler, B. Csatho, S. L. Farrell, H. A. Fricker, D. Harding, R. Kwok, M. Lefsky, T. Markus, A. Marshak, T. Neumann, S. Palm, B. Schutz, B. Smith, J. Spinhirne, and C. Webb, "The ICESat-2 Laser Altimetry Mission," in *Proceedings of the IEEE*, 2010, vol. 98, no. 5, pp. 735–751.

[65] M. Awadallah, S. Ghannam, L. Abbott, and A. Ghanem, "A two-stage algorithm for extraction of ground and top of canopy in photon-counting profiling-LiDAR data in preparation for the ICESat-2 mission," in *2014 IEEE Geoscience and Remote Sensing Symposium*, 2014, pp. 1353–1356.

[66] K. M. Brunt, T. A. Neumann, K. M. Walsh, and T. Markus, "Determination of local slope on the Greenland ice sheet using a multibeam photon-counting lidar in preparation for the ICESat-2 mission," *IEEE Geosci. Remote Sens. Lett.*, vol. 11, no. 5, pp. 935–939, 2014.

[67] M. McGill, T. Markus, V. S. Scott, and T. Neumann, "The Multiple Altimeter Beam Experimental Lidar (MABEL): An Airborne Simulator for the ICESat-2 Mission," *J. Atmos. Ocean. Technol.*, vol. 30, no. 2, pp. 345–352, Feb. 2013.

[68] D. Gwenzi, M. A. Lefsky, V. P. Suchdeo, and D. J. Harding, "Prospects of the ICESat-2 laser altimetry mission for savanna ecosystem structural studies based on

airborne simulation data," *ISPRS J. Photogramm. Remote Sens.*, vol. 118, pp. 68–82, Aug. 2016.

[69] D. Harding, P. Dabney, S. Valett, A. Yu, A. Vasilyev, and A. Kelly, "Airborne polarimetric, two-color laser altimeter measurements of lake ice cover: A pathfinder for NASA's ICESat-2 spaceflight mission," in *2011 IEEE International Geoscience and Remote Sensing Symposium*, 2011, pp. 3598–3601.

[70] A. W. Yu, D. J. Harding, and P. W. Dabney, "Laser transmitter design and performance for the slope imaging multi-polarization photon-counting lidar (SIMPL) instrument," 2016, vol. 9726, p. 97260J.

[71] P. Cho, H. Anderson, R. Hatch, and P. Ramaswami, "Real-Time 3D Ladar Imaging," in *Proceedings - HPCMP Users Group Conference, UGC 2006*, 2006, vol. 16, no. 1, p. 62350G–62350G–12.

[72] R. M. Marino and W. R. Davis, "Jigsaw: a foliage-penetrating 3D imaging laser radar system," *Lincoln Lab. J.*, vol. 15, no. 1, pp. 23–36, 2005.

[73] A. L. Neuenschwander, M. M. Crawford, L. A. Magruder, C. A. Weed, R. Cannata, D. Fried, R. Knowlton, and R. Heinrichs, "Terrain classification of ladar data over Haitian urban environments using a lower envelope follower and adaptive gradient operator," in *Proceedings of SPIE - The International Society for Optical Engineering*, 2010, vol. 7684, p. 768408.

[74] R. Knowlton, "Airborne Ladar Imaging Research Testbed," *MIT Lincoln Lab. Tech Notes*, 2011.

[75] K. Y. Shrestha, "Mixed Topographic and Shallow Bathymetric Mapping via Multi-stop Photoelectron Laser Ranging," PhD. Dissertation. University of

Florida, 2010.

[76] J. J. Degnan, D. Wells, R. Machan, and E. Leventhal, “Second generation airborne 3D imaging lidars based on photon counting,” in *Optics East 2007*, 2007, p. 67710N–67710N–7.

[77] J. Degnan, R. Machan, E. Leventhal, G. Jodor, and C. Field, “Photon-Counting, 3D imaging Lidars Operating at Megapixels per Second,” *2009 Conference on Lasers and Electro-Optics and 2009 Conference on Quantum electronics and Laser Science Conference*. pp. 1–2, 2009.

[78] R. I. Abbot, P. J. Shelus, J. D. Mulholland, and E. C. Silverberg, “Laser observations of the Moon: Identification and construction of normal points for 1969-1971,” *Astron. J.*, vol. 78, no. 8, p. 784, Oct. 1973.

[79] M. Awadallah, S. Ghannam, L. Abbott, and A. Ghanem, “Active Contour Models for Extracting Ground and Forest Canopy Curves from Discrete Laser Altimeter Data,” in *Proceedings: 13th International Conference on LiDAR Applications for Assessing Forest Ecosystems*, 2013, pp. 1–8.

[80] J. Canny, “A Computational Approach to Edge Detection,” *IEEE Trans. Pattern Anal. Mach. Intell.*, vol. PAMI-8, no. 6, pp. 679–698, Nov. 1986.

[81] T. Cossio, “Prediction of topographic and bathymetric measurement performance of airborne low-SNR lidar systems,” University of Florida, 2009.

[82] A. Swatantran, H. Tang, T. Barrett, P. DeCola, and R. Dubayah, “Rapid, High-Resolution Forest Structure and Terrain Mapping over Large Areas using Single Photon Lidar,” *Sci. Rep.*, vol. 6, p. 28277, Jun. 2016.

[83] X. Wang, Z. Pan, and C. Glennie, “A Novel Noise Filtering Model for Photon-

Counting Laser Altimeter Data," *IEEE Geosci. Remote Sens. Lett.*, vol. 13, no. 7, pp. 947–951, Jul. 2016.

[84] Chih-Cheng Tseng, Hsuan-Tsang Chen, and Kwang-Cheng Chen, "On The Distance Distributions of The Wireless Ad Hoc Networks," in *2006 IEEE 63rd Vehicular Technology Conference*, 2006, vol. 2, pp. 772–776.

[85] NASA, "MABEL_L2A Product Data Dictionary," 2014.

[86] NASA, "http://icesat.gsfc.nasa.gov/icesat2/data/mabel_docs.php," 2010. .

[87] X. Wang, C. Glennie, and Z. Pan, "An Adaptive Ellipsoid Searching Filterfor Airborne Single-Photon Lidar," *IEEE Geosci. Remote Sens. Lett.*, pp. 1–5, 2017.

[88] S. Wold, K. Esbensen, and P. Geladi, "Principal component analysis," *Chemom. Intell. Lab. Syst.*, vol. 2, no. 1–3, pp. 37–52, Aug. 1987.

[89] H. Tang, A. Swatantran, T. Barrett, P. DeCola, and R. Dubayah, "Voxel-Based Spatial Filtering Method for Canopy Height Retrieval from Airborne Single-Photon Lidar," *Remote Sens.*, vol. 8, no. 9, p. 771, Sep. 2016.

[90] X. Wang, C. Glennie, and Z. Pan, "Adaptive noise filtering for single photon LiDAR observation," in *2017 IEEE The International Geoscience and Remote Sensing Symposium*, 2017, pp. 3361–3364.

[91] L. Cheng, L. Tong, Y. Wang, and M. Li, "Extraction of Urban Power Lines from Vehicle-Borne LiDAR Data," *Remote Sens.*, vol. 6, no. 4, pp. 3302–3320, Apr. 2014.

[92] G. Sohn, Y. Jwa, and H. B. Kim, "Automatic Powerline Scene Classification and Reconstruction Using Airborne LIDAR Data," *ISPRS Ann. Photogramm. Remote Sens. Spat. Inf. Sci.*, vol. I–3, pp. 167–172, Jul. 2012.

[93] R. A. Mclaughlin, “Extracting Transmission Lines From Airborne LIDAR Data,” *IEEE Geosci. Remote Sens. Lett.*, vol. 3, no. 2, pp. 222–226, Apr. 2006.

[94] L. Matikainen, M. Lehtomäki, E. Ahokas, J. Hyyppä, M. Karjalainen, A. Jaakkola, A. Kukko, and T. Heinonen, “Remote sensing methods for power line corridor surveys,” *ISPRS J. Photogramm. Remote Sens.*, vol. 119, pp. 10–31, Sep. 2016.

[95] H. B. Kim and G. Sohn, “Random Forests Based Multiple Classifier System for Power-Line Scene Classification,” *ISPRS - Int. Arch. Photogramm. Remote Sens. Spat. Inf. Sci.*, vol. XXXVIII–5/, pp. 253–258, Sep. 2012.

[96] J. Liang, J. Zhang, K. Deng, Z. Liu, and Q. Shi, “A New Power-Line Extraction Method Based on Airborne LiDAR Point Cloud Data,” in *2011 International Symposium on Image and Data Fusion*, 2011, pp. 1–4.

[97] L. Zhu and J. Hyyppä, “Fully-Automated Power Line Extraction from Airborne Laser Scanning Point Clouds in Forest Areas,” *Remote Sens.*, vol. 6, no. 11, pp. 11267–11282, Nov. 2014.

[98] M. Gerber and R. Kleiman, “Afterpulse background suppression in time-correlated single photon counting lifetime experiments using optimized gate filter,” in *Photovoltaic Specialist Conference (PVSC), 2014 IEEE 40th*, 2014, pp. 1899–1902.

[99] R. Staubert, E. Bohm, K. Hein, K. Sauerland, and J. Trumper, “Possible effects of photomultiplier-afterpulses on scintillation counter measurements,” *Nucl. Instruments Methods*, vol. 84, no. 2, pp. 297–300, Jul. 1970.

[100] K. Y. Shrestha, W. E. Carter, K. C. Slatton, and T. K. Cossio, “Shallow bathymetric mapping via multistop single photoelectron sensitivity laser ranging,”

IEEE Trans. Geosci. Remote Sens., vol. 50, no. 11, pp. 4771–4790, 2012.

[101] M. P. Bristow, "Suppression of afterpulsing in photomultipliers by gating the photocathode," *Appl. Opt.*, vol. 41, no. 24, pp. 4975–4987, 2002.

[102] P. B. Coates, "The origins of afterpulses in photomultipliers," *J. Phys. D. Appl. Phys.*, vol. 6, no. 10, p. 1159, 1973.

[103] J. Zhang, M. A. Itzler, H. Zbinden, and J.-W. Pan, "Advances in InGaAs/InP single-photon detector systems for quantum communication," *Light Sci. Appl.*, vol. 4, no. 5, p. e286, May 2015.

[104] M. Liu, C. Hu, J. C. Campbell, Z. Pan, and M. M. Tashima, "Reduce Afterpulsing of Single Photon Avalanche Diodes Using Passive Quenching With Active Reset," *IEEE J. Quantum Electron.*, vol. 44, no. 5, pp. 430–434, May 2008.

[105] N. Namekata, S. Sasamori, and S. Inoue, "800 MHz single-photon detection at 1550-nm using an InGaAs/InP avalanche photodiode operated with a sine wave gating," *Opt. Express*, vol. 14, no. 21, p. 10043, 2006.

[106] N. Namekata, S. Adachi, and S. Inoue, "1.5 GHz single-photon detection at telecommunication wavelengths using sinusoidally gated InGaAs/InP avalanche photodiode," *Opt. Express*, vol. 17, no. 8, p. 6275, Apr. 2009.

[107] N. Namekata, S. Adachi, and S. Inoue, "Ultra-Low-Noise Sinusoidally Gated Avalanche Photodiode for High-Speed Single-Photon Detection at Telecommunication Wavelengths," *IEEE Photonics Technol. Lett.*, vol. 22, no. 8, pp. 529–531, Apr. 2010.

[108] Z. L. Yuan, B. E. Kardynal, A. W. Sharpe, and A. J. Shields, "High speed single photon detection in the near infrared," *Appl. Phys. Lett.*, vol. 91, no. 4, p. 041114,

Jul. 2007.

[109] L. Xu, E. Wu, X. Gu, Y. Jian, G. Wu, and H. Zeng, “High-speed InGaAs/InP-based single-photon detector with high efficiency,” *Appl. Phys. Lett.*, vol. 94, no. 16, p. 161106, Apr. 2009.

[110] W. Dumouchel and F. O’Brien, “Integrating a robust option into a multiple regression computing environment,” *Inst. Math. Its Appl.*, vol. 36, p. 41, 1991.

[111] P. W. Holland and R. E. Welsch, “Robust regression using iteratively reweighted least-squares,” *Commun. Stat. - Theory Methods*, vol. 6, no. 9, pp. 813–827, Jan. 1977.

[112] J. Fernandez-Diaz, W. Carter, C. Glennie, R. Shrestha, Z. Pan, N. Ekhtari, A. Singhania, D. Hauser, and M. Sartori, “Capability Assessment and Performance Metrics for the Titan Multispectral Mapping Lidar,” *Remote Sens.*, vol. 8, no. 11, p. 936, Nov. 2016.